GKSS
FORSCHUNGSZENTRUM
in der HELMHOLTZ-GEMEINSCHAFT

Study of the interaction between the current field and structures in the bathymetry in a tidal inlet

(Vom Fachbereich Coastal Research Laboratory, Forschungs- und Technologiezentrum Westküste (FTZ), der Christian-Albrechts-Universität zu Kiel als Diplomarbeit angenommen)

Authoress:
G. Kakoulaki

ISSN 0344-9629

HELMHOLTZ
| GEMEINSCHAFT

wissen
schafft
nutzen

GKSS 2009/9

GKSS 2009/9

Study of the interaction between the current field and structures in the bathymetry in a tidal inlet

(Vom Fachbereich Coastal Research Laboratory, Forschungs- und Technologiezentrum Westküste (FTZ), der Christian-Albrechts-Universität zu Kiel als Diplomarbeit angenommen)

Authoress:
G. Kakoulaki
(Institute for Coastal Research)

GKSS-Forschungszentrum Geesthacht GmbH • Geesthacht • 2009

Die Berichte der GKSS werden kostenlos abgegeben.
The delivery of the GKSS reports is free of charge.

Anforderungen/Requests:

GKSS-Forschungszentrum Geesthacht GmbH
Bibliothek/Library
Postfach 11 60
21494 Geesthacht
Germany
Fax.: +49 4152 87-17 17

ISSN 0344-9629

GKSS-Forschungszentrum Geesthacht GmbH · Telefon (04152) 87-0
Max-Planck-Straße 1 · 21502 Geesthacht / Postfach 11 60 · 21494 Geesthacht

GKSS 2009/9

Study of the interaction between the current field and structures in the bathymetry in a tidal inlet

(Vom Fachbereich Coastal Research Laboratory, Forschungs- und Technologiezentrum Westküste (FTZ), der Christian-Albrechts-Universität zu Kiel als Diplomarbeit angenommen)

Georgia Kakoulaki

121 pages with 70 figures and 9 tables

Abstract

Comparisons between current velocities obtained from Radar Doppler Current Profiler (RDCP) and a two-dimensional depth integrated flow model are presented. The investigation area is located in the northern tip of the Sylt Island in the North Sea, Germany. Study results from a measuring campaign carried out in spring 2007 using a Radar Doppler Current Profiler deployed from a moving vessel were analyzed. The RDCP is a new ship based remote sensing method recently developed by the Institute for Coastal Research of the GKSS that has been used to scan the surface current velocity field horizontally. A two-dimensional depth integrated model covering the area of investigations was developed on the basis of Delft3D by WL Delft Hydraulics, the Netherlands. Comparisons between measured and computed current velocities for a 15 days period in May 2007 were done to check the model accuracy. The comparison is done by checking the same areas in the model that the RDCP measurements cover. Good agreement resulted proving the adequacy of the method for model development.

Untersuchung der Wechselwirkungen von Strömungsfeld und Unterwasserdünen in einem Tidekanal

Zusammenfassung

In dieser Arbeit wird ein Vergleich von Strömungsfeldern, die mit dem Radar Doppler Current Profiler (RDCP) gemessen wurden, und einem zweidimensionalen, tiefenintegrierten Strömungsmodell präsentiert. Das Messgebiet befindet sich an der Nordspitze der Insel Sylt in der Deutschen Bucht. Die Grundlage der vorliegenden Ergebnisse ist eine Messkampagne, die im Mai 2007 im Messgebiet durchgeführt wurde und Daten eines schiffsgestützten RDCP verwendete. Das RDCP ist ein neues, schiffsbasiertes Fernerkundungssystem, das am Institut für Küstenforschung der GKSS entwickelt wurde, um horizontale Oberflächenströmungen flächenhaft zu erfassen. Ein zweidimensionales, tiefenintegriertes Modell, welches das Messgebiet abdeckt, wurde auf der Basis der Delft3D-Software von WL Delft Hydraulics in den Niederlanden entwickelt. Für die Überprüfung der Genauigkeit des Modells wurden berechnete und gemessene Daten eines 15-tägigen Zeitraums im Mai 2007 miteinander verglichen. Für den Vergleich wurden RDCP-Daten und Modelldaten des exakt gleichen Gebietes überprüft. Eine gute Übereinstimmung der Daten beweist eine grundsätzliche Tauglichkeit der Methode für Modellentwicklungen.

Manuscript received / Manuskripteingang in TFP: 8. Oktober 2009

Table of Contents

List of Figures and Tables

Notations

ADCP	Acoustic Doppler Current Profiler
BSH	Bundesant fur Seeschiffahrt und Hydrographie
C_{2D}	2D Chezy coefficient ($m^{1/2}/s$)
CODAR	Coastal Ocean Dynamics Applications Radar
C_r	Courant Number (-)
CSM	Continental Shelf Model
DWD	Deutsche Wetterdienst
Δt	time step (s)
Δx	cell width in x direction (m)
Δy	cell width in y direction (m)
d	distance
d_{50}	median bed size of the sediments
∂	partial derivation operator
F	External driving force (wind, waves, Carioles)
g	acceleration due to gravity (m/s^2)
GBM	German Bight Model
H	average depth (m)
h	water depth (m)
θ	incidence angle
k	effective dispersion coefficient
k_s	Nikuradse roughness length
LKN	Landedbetrieb fur Kustenschutz, Nationalpark und Meeresschut
λ_s	sea surface wavelength,
λ_r	radar wavelength and
M	x direction of the model

MAE	Mean absolute error
N	y direction of the model
n	Manning's coefficient
p	the power parameter (p>0)
$RDCP$	Radar Doppler Current Profiler
$RMAE$	Relative Mean Absolute Error
ρ	fluid density (kg/m³)
ρ_0	water density (kg/m^3)
SAR	Synthetic Aperature Radar
$SLAR$	Side-looking airborne radar
t	time (s)
$\vec{\tau}_b$	bed shear stress vector
z_b	bed level above reference datum (m)
τ_{bx}, τ_{by}	bed shear stress in x, y directions (N/m²)
$\vec{U}$	vector of the horizontal velocity (m/s)
V_f	volume below the MSL of the finer grid
V_i	volume below the MSL of the examined grid
$\bar{v},\ \bar{u}$	fluid velocities in y, x – directions (m/s)
$WaMoS$	Waves Monitoring System, ground based
$w(d)$	weight indicator
$WERA$	Wellen Radar
WSA	Wasser- und Schifffahrtsamt
$\sum_{j=1}^{n} Mod_j$	sum of the computed values from the model
$\sum_{j=1}^{n} Mea_j$	sum of the measurements
2DH	two dimensional depth integrated model
LW	low water

Acknowledgements

This thesis is a collaboration between the GKSS, Institute for Coastal Research, Radar Hydrogrpahy department, and the CORELAB, University of Kiel.

I would like to express my sincere gratitude to Dr. F. Ziemer for giving the opportunity to implement my master thesis at the Department of Radar Hydrography (KOR) of GKSS Research Center. His continuous support helped me to complete my research.

My truly, deeply respect and appreciation to Professor R. Mayerle for the instigation, the support and the recognition of my effort. His belief on my skills encouraged and inspired me to round off my thesis.

I would like to express grateful thankfulness to S. Flampouris for offering me his scientific knowledge, the continuous encouragement, to be patient and helpful whenever I needed him. Without him this thesis would not have been completed.

Moreover I would like to thank the members of KOR, Mr. M. Cyceswski and S. Sedlacek, for tutoring me in programming and their help for technical and practical problems and Dr. Talal Etri for all his help in the modeling part.

I also want to acknowledge Dr. Walter Puls from the KSS department of GKSS for providing data for the thesis. Martina Heineke from the KOK department of GKSS for providing the multi beam echo sounder data.

Many thanks to my friends in CORELAB for the wonderful time that we had all together during the master course. Especially, I will like to thank my friend Ara for the help that he offered, Iria and Andre for hosting me and their good friendship. Katharina and Simon for reviewing the thesis.

Finally, my parents and my second family Apostolo and Lioula for giving me the wings to fly and find my Ithaki.

1 Introduction

Coastal circulation has been subject of research by marine scientists since the earliest days of fishing and shipping. The two most easily distinguishable causes for coastal motions are winds and tides. The response of coastal waters to these forces varies widely, influenced by climate, geomorphology and stratification [WINNET, 1980]. Due to this inexhaustible power the sea hydrodynamics are controlled by the currents. Currents are cohesive streams of sea water that circulates through the oceans and influences climate and living conditions for humans, plants and animals.

Monitoring the actual state of beaches and coastlines and predicting future states on a variety of timescales drove oceanographers to resort observation systems in order to study the oceanic and coastal processes. In coastal areas these observations are needed to support human activities such as weather, ship routing services etc or for the protection from eroding forces of wind, waves and currents, and the management of the coastal zone with its precious resources.

Since the discovery of the IR spectral region in 1800 by Sir William Herschel and the first use of the X-band radar, remote sensing became part of the oceanographic routine. Over the past 50 years, remote sensing has been developed into a very useful tool for monitoring the near shore environment, as it covers large inaccessible geographic areas more frequently than field sampling. On the other hand it cannot penetrate below the ocean's surface. Nevertheless, remote sensing microwave radars appear to offer solutions to several of the problems faced by in situ current measurements.

Coastal scientists and engineers often utilize either data driven extrapolation techniques or process-based numerical and analytical models to predict near shore flow fields and the resulting coastal evolution. In the recent past, numerical models have gained ground in improving our understanding of natural coastal dynamics and the assessment of consequences of human impact. If the relevant physical processes are known and expressed in mathematical formulations, numerical models can today be developed to simulate coastal processes on a discrete grid [WINNET, 2003; LESSER, 2004]. Both represent classical approaches, with known limitations; owing to for instance the lack of long term high-resolution data sets, poor opportunities for model calibration or inadequate representation of fundamental coastal processes in the model formulations. In the scope of the contemporary extensive observational programs, data assimilative models can serve as tools for data synthesis, or as dynamically based interpolators between observations that remain sparse in space and time. Velocity measurement problems are sometimes addressed by using numerical models to synthesize the velocity partners of a given spatial domain [SHIELDS, 2003].

Modelling and data simulation are to become essential components of emerging coastal observatories, providing three-dimensional (3D) or two-dimensional (2D and time-dependent descriptions of the ocean dynamics on the continental shelf. The measurement of surface currents has been conducted, historically, using a variety of techniques.

1.1 Objectives

The present investigation is an extended combined approach where in situ measurements and numerical hydrodynamic modelling is applied to understand the governing physics of the tidal basin Sylt-Romo, to support a management of the coastal area.

The first aim of the present research is the determination of the water mass transport in the tidal inlet of North Sylt Island as a function of the surface by Radar Doppler Current Profiler (RDCP) and water column current field by Acoustic Doppler Current Profiler (ADCP) and the bathymetry by a multi beam echo sounder. The second aim is the determination of the impact of the actual depth and of the laying geo-structures on the current field.

The pioneer part of the research is the combination of ship based, aerial time series measurements of the surface current field (RDCP) for the validation of the two dimensional hydro dynamical flow model using DELFT 3D of the tidal inlet.

1.2 Outline

The thesis is divided into 8 chapters. The first chapter informs the reader about the objectives, the structure of the thesis and the region of investigation is described. In the second chapter, the theoretical background is given in brief terms about the tides, tidal inlets, currents and their measurements and numerical modelling. The data acquisition, the available data and the instruments that used in this experiment are described in details in chapter three. The analysis of the field measurements is given in chapter four. Chapter five describes the development of the flow model. In chapter six the sensitivity studies of the numerical parameters are described and their effect on the model whereas the physical parameters and their influence in the model are presented. The comparison of the in situ measurements and the 2DH model on the basis of the RDCP is included in chapter eight. Moreover, in chapter eight the results of the data analysis are presented and discussed. Finally, the conclusions of the study and the outlook for further investigation are presented in chapter 9.

1.3 Region of Investigation

This study is focused on the biggest North-Frisian island Sylt, located 15 km off the German North Sea coast close at the Danish border (figure 1-1). The area of investigation is a semi-enclosed tidal inlet named "Lister Tief", between the northern tip of Sylt Island and southern part of Rømø Island, Denmark; both of these barrier islands are connected to the mainland by dams. The selection of Lister Tief was made due to the fact that it is the most pronounced and dynamic marine sand wave field in German coastal waters [HENNINGS, 2006].

The width of the tidal channel is 2.5 km and its depth exceeds the 30 m. The channel system is complex, consisted by three main channels Lister Ley (south), Hojer Dyb (southeast) and Romo Dyp (northeast). More than 50 % of the bight is characterized as sub-tidal areas, 33 % as intertidal and only 10 % as deep tidal channels [KAPPENBERG, 1997]. The tide is semi-diurnal with an average tidal range of about 1.8 m, classifying it as a micro-tidal estuary according to Davis (1964) or lower meso-tidal after Hayes (1979). For that reason cross shore transport is caused through the channels between the barrier islands.

The long shore transport along the west coasts is mainly wave-induced. The mean tidal currents are approximately 1–1.5 m/s and the tidal heights in the region are of the range 1.8 m, due to the limited depth of the inlet the effect of the wind on the hydrodynamics is significant. One part of the Lister Tief tidal area is consisted by tidal mud flats that are inundated nearly every tidal cycle. Under normal weather conditions, the tidal flats are covered with water for a period of 4.5–8 h during each tidal period [ANDERSEN, 1999].

Two small rivers discharge through sluice gates into the tidal area. The rivers BredeA and Vida have catchment areas of 464 km^2 and 1364 km^2, respectively. The mean freshwater discharge from these two rivers amounts to about 1.106 m^3 or 0.2 % of the tidal prism over one tidal cycle [PEJRUP, 2005]. Exchange with the open sea is only possible through the inlet between the two barrier islands [KAPPENBERG, 1997].

Lister Tief shows large morphological changes due to strong tidal current velocities. The sea bed morphology of the Lister Tief tidal channel is a complex configuration of different bed-forms. Small-scale as well as mega-ripples are superimposed on sand waves. In the troughs of sand waves often mega-ripple fans can be observed with a crest orientation perpendicular to the orientation of sand waves [HENNINGS, 2006]. The sand waves have average 200–500 m wavelength and 5–10 m height and as such sufficient to produce surface capillary wave features. The sand waves in Lister Tief are migrating less than 80 m per year [SLATER, 2005].

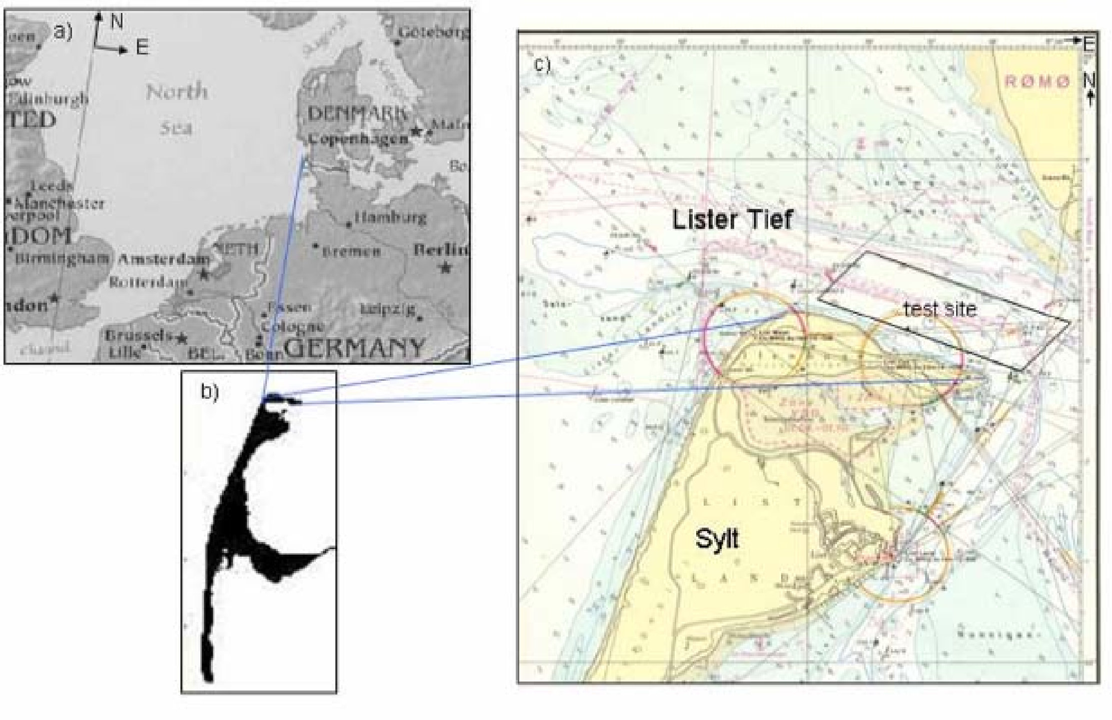

Figure 1-1. (a & b) Locations of the island of Sylt and the Lister Tief in the German Bight of the North Sea (c) Bathymetry of the Lister Tief tidal channel bounded by the islands of Sylt to the south and Rømø to the north, [source base map: TOP50 Schleswig Holstein and Hamburg**,** HENNINGS, 2006].

2 Theoretical Background

For the complete approach of the subject, it is essential to present the basic concepts beyond the currents and their generation forces, the current measurements, the tides and the radar imaging mechanism. In the following section of the chapter those subjects are presented.

2.1 Currents

Currents are the dominant mechanism of the sediment motion. Accurate estimations of coastal flow paths bring economic benefits and increase human safety. Currents transport nutrients, organisms and other biological and chemical constituents are important for the sustainability of the oceanic environment.

Consequently, gravity moves the density currents. A density difference in a fluid, in a gravitational field leads to pressure differences that drive the flow. Examples of density currents are turbidity currents or the thermohaline circulation. Moreover, geo-strophic currents are controlled by a balance between a pressure gradient force and the Carioles deflection. Large-scale mid-latitude ocean (and atmospheric) flow are in approximate geo-strophic balance.

The tidal currents, as their name suggests, are generated by the tides. Tides are essentially long, slow waves created by the gravitational force of the moon and to a lesser degree, the sun and the solar planets, on the earth surface. This due to the fact that the moon is 389 times closer to the Earth than the sun is [OPEN UNIVERSITY 2000]. The rise and fall of a tide is accompanied by the horizontal movement of the water called tidal current. It is necessary to make clear distiguishment between the tide and the tidal current, for the relation between them is complex and variable. Tide is the vertical rise and fall of the water, while the tidal current is the horizontal flow. The role of the tides is to rise and fall, while the tidal current floods and ebbs [POND 1983].

Tidal currents, just like tides, are mostly affected by the sum of the gravitational potential of moon and sun. When the period (28 days) of this common forcing is synchronous to the phase of the moon, tidal current velocities are strong and are called “spring currents”. In case of the moon is at the first or third quarter phases, tidal current velocities are weak and are called “neap currents” [PINET 2000]. The main difference between the tidal currents and other types of currents is that they don't flow as a continuous stream but they switch directions every time the tide transitions between high and low [SKINNER, 1989].

Most of the strongest tidal currents occur around three hours before or after the peak of high and low tides. When the tide rises and the flow of the transport is directed towards the shore, the tidal current is called flood current. On the other hand, when the tide recedes and the current is directed back out to the sea, it is called ebb current. Because the relative positions of the moon, sun and earth change at a known rate, tidal currents are predictable, following the astronomical conditions.

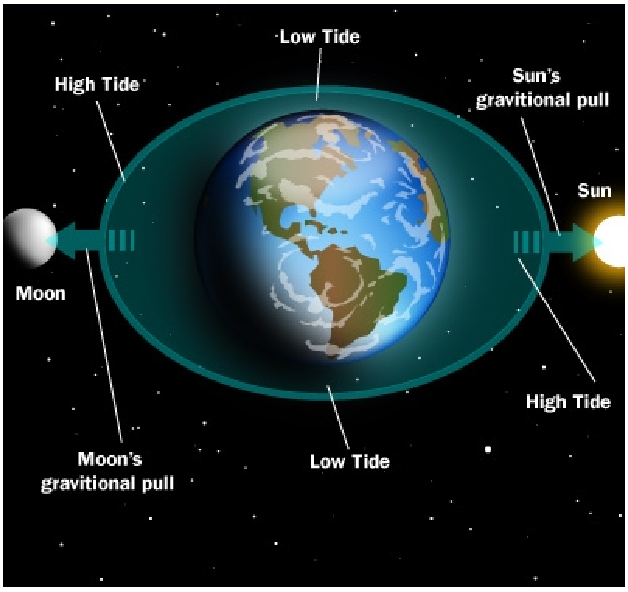

Figure 2-1. Influence of the moon on earth's gravitation forces, [science.howstuffworks.com/ocean-current4].

2.1.1 Current measurements

Ocean current date may be collected by a variety of methods. Once, the current velocity was measured exclusively by mechanical devices, nowadays it is almost entirely done by electronic instrumentation. Oceanographers can choose between instruments that use very different techniques including rotors and vanes, electromagnetic induction and Doppler instruments. Current meters only give information on the speed and direction of the water at the location of the instrument itself. Current measurements show that the current velocity has significant variations in time and space of the range 0–6 knots (1 knot = 1.852 km/h) [PICKARD 1990].

The measurement of the current can be given either as a flow speed (e.g., knots or m/sec) and a direction in which the current is moving (usually a heading given in degrees measured clockwise from true north) or as two separate flow speed components, U and V, measured along two orthogonal axes. The axes are usually oriented such that U represents the horizontal component of flow in the east-west direction while V represents the horizontal component in the north-south direction [PINET 2000].

The measurements of currents are divided into two categories the Eularian (in honor of the Swiss mathematician Leonhard Euler) and the Lagrangian measurements (in honor of Joseph Louis Lagrange, a French mathematician).

The Eularian method determines the water’s velocity at a fixed location in the fluid and is recorded over time. This is typically accomplished by the use of an electro-mechanical current meter, which measures the velocity at a single depth or the ADCP, which can provide a profile of velocity with depth. Current meters are usually mounted on a wire of a mooring, which is deployed from a ship. The ADCP can be mounted on a mooring at the bottom, or the underside of a vessel. Both will provide a time series of the velocity of the ocean's water mass at a single geographic location.

The Lagrangian method the current measurement is established in such a way that the path of each fluid particle is followed and is stated as a function of time. The simplest Langrangian current indicator is an object, called drifter, floating in the water with a minimum of surface exposed to the wind [PICKARD 1990]. Scientists have launched thousands of Lagrangian drifters into the ocean and deployed hundreds of fixed Eulerian stations near shore to observe ocean circulation. Tracking this drifter (by satellite, radar, radio, sound, etc) will give a quantitative description of the current velocity.

In both cases, Eulerian and Lagrangian measurements, the statements are usually made with respect to the axes which are stationary relative to the solid earth. In theoretical studies the Eulerian method it is easier to use, but in describing the circulation of the sea, the Lagrangian method is used more frequently [PICKARD 1990].

Faced with a particular situation, the oceanographers have to choose the instruments which provide the best data. Many previous in ocean and laboratories, have contributed to compare. The results have shown large discrepancies depending on the sensors [PICKARD 1990]. Scientists often use a combination of different techniques, such as in this thesis, where two different methods provide 3D current field observations.

2.1.2 Radar

Current measurements can also be obtained by radars carried by ships, planes, satellites or by ground based radars. Current measurements by remote sensing can be classified into two methods: space borne sensors, such as SAR and microwave altimeter; and ground base radar, such as X-band radar. Space borne sensors have the properties of global measurements, large size footprint and lower comparing resolution, in the order of ten to twenty meters to a few kilometers. On the other hand, X-band radar is suitable for monitoring waves, currents in near offshore or shallow zones [ALPERS & HASSELMAN, 1981, WU LI CHU, 2008].

In the past different types of radar systems have been used for observing the ocean

- SAR (Synthetic Aperature Radar)
- SLAR (Side-looking airborne radar)
- High Frequency radars (CODAR, WERA)
- WaMoS (Waves Monitoring System, ground based)
- MiROS

X-band radar was originally used for detecting obstacles or land while navigating at sea. It is used for measurements due to the reflectivity from the sea clutter at similar wavelengths to the sensors based on Bragg scattering [LONGUET-HIGGINS 1987, HASSELMAN & ALPERS 1952]. X-band radar, uses a microwave frequency band (0.01–1 m), that can measure Bragg scattering from the sea clutter with wavelengths of 0.5–50 cm. Because of the smaller wavelength, the X band radar is more sensitive towards smaller waves.

The Bragg backscattering theory consists the main broadly used for the backscattering of radars, e.g. ground based or naval radars. As the incidence angle of the radar is oblique to the local mean angle of the ocean surface, there is almost no direct specular reflection except at very high sea states. Therefore it is assumed that at first approximation Bragg resonance is the primary mechanism for backscattering radar pulses. The Bragg equation defines the ocean wavelengths for Bragg scattering as a function of radar wavelength and incidence angle:

$$\lambda_s = \frac{\lambda_r}{2\sin\theta} \quad (1)$$

Where:

λ_s = the sea surface wavelength,

λ_r = the radar wavelength and

θ = the incidence angle.

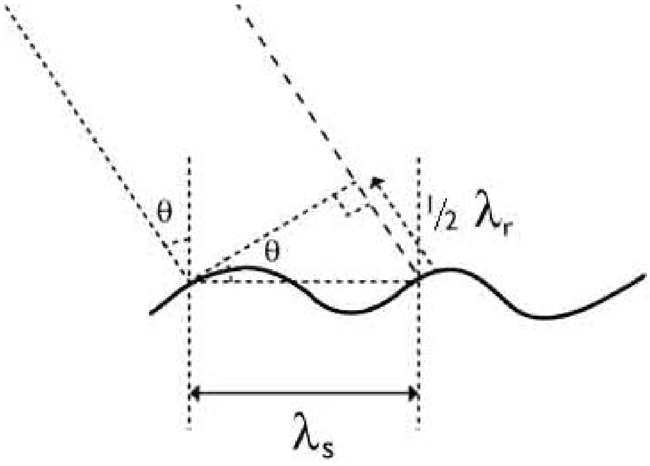

Figure 2-2. Scheme to visualize the relation between the scattering wave's length λ_s and the electromagnetic wave length λ_r. The relation between those two is observed by [CROMBIE 1956] and consist the basic principle of the radar systems.

The short Bragg-scale waves are formed in response to wind stress. If the sea surface is rippled by a light breeze with no long waves present, the radar backscatter is due to the component of the wave spectrum which resonates with the radar wavelength. The Bragg resonant wave has its crest nominally at right angles to the range direction [FLAMPOURIS 2006].

2.2 Tidal Inlets

Tidal inlets occur along a major part of the world's sandy coastlines. They are increasingly influenced by human interventions such as maintenance dredging, jetty construction, and land reclamation in the basin. Knowledge of the intervention-induced effects on inlet dynamics is crucial for successful coastal management because they can represent a hazard to neighboring areas since they induce strong shoreline changes [ELIAS 2006].

A tidal inlet is defined as an opening in the shore through which water penetrates the land thereby proving a connection between the ocean and bays, lagoons, and marsh and tidal creek systems. Tidal currents maintain the main channel of a tidal inlet. [GERALD 2005]. Often the tidal inlets are theorized as the relatively short channels connecting the bay and the ocean. There are cases that they exhibit irregular geometry and branch into multiple channels at the ocean – and bay-side leading to complicated flow patterns. As a result of the large variations in depth and width, the velocity field contains both vertical and horizontal eddies [VAN DE KREEKE 1992].

According to Hubband and Oertel 1979 three types of inlets are identified:

- Tide-dominated inlets are characterized by a deep, ebb-dominant main channel flanked by long, linear channel-margin bars. Sand bodies landward of the inlet throat are confined to tidal bars further landward in the marsh creek system.
- Wave-dominated inlets are characterized by large, flood-tidal deltas building into wide, open lagoons. Tidal channels are generally shallow (less than 6 m) and often bifurcate landward and seaward of the throat.
- In transitional inlets, major sand bodies are typically concentrated in the inlet throat. These inlets vary widely in morphology and sand body geometry.

Tidal inlets occur usually in meso-tidal environments, with moderate wave energy (about 0.6 to 1.5 m) [HAYES 1979]. Tidal inlet characteristics are controlled by wave energy, tidal range, tidal prism, sediment supply and direction and rates of sand delivered to the inlet [BERTIN 2004]. At most inlets over the long term, the volume of water entering the inlet during the flooding tide equals the volume of water leaving the inlet during the ebbing cycle. This volume is referred to as the tidal prism. The tidal prism is a function of the open water area and tidal range in the back barrier as well as frictional factors, which govern the ease of flow through the inlet [GERALD 2005].

A typical tidal-inlet/barrier-basin system consists of several morphological units [GEYLL 1976, VAN VEEN 2005] (figure 2-3). Seaward of the inlet, a shallow ebb-tidal delta occurs that often folds around a deep channel. On the delta itself, smaller-scale bars are observed that feature migration behavior, indicating that sand is being bypassed from one barrier island to the next. Just landward of the inlet, sometimes a flood delta is observed. In the main channels of the basins, tidal bars occur that have an along-channel wavelength several times the channel width [AHNERT 2001,

DALRYMPLE & RHODES 1995, VAN VEEN 2005]. When moving further inside the basin, the main channels become shallower and also undergo a sequence of bifurcations, resulting in a complex pattern of channels and tidal flats. Near the coastlines of the mainland and the barrier islands, salt marshes commonly occur.

Inlets vary in size and in stability. Some of them have a tendency to shift and to migrate while others comparatively fixed and permanent. Inlets migrate at rates that vary from a few to several tens of meters per year, depending upon such variables as rate of long shore sediment transport and depth of the inlet [HAYES 1979].

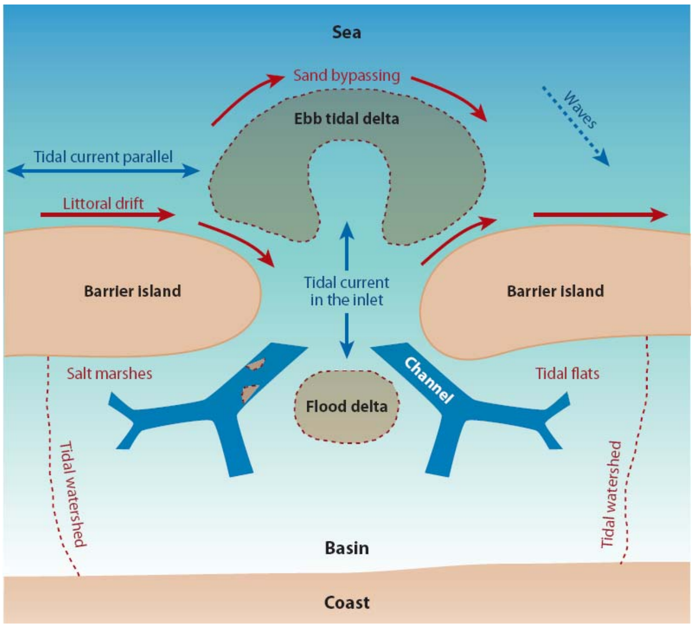

Figure 2-3. Sketch of an idealized tidal inlet system, showing the different geomorphologic elements and the dominant physical processes and phenomena, [SWART 2009].

2.3 Numerical Modelling

In recent years, there has been an increase in the use of numerical simulation models in the earth sciences as a means to evaluate large-scale or complex physical processes. Moreover, the great economic importance of the coastal zone has led to the development of many different numerical models for describing coastal currents, tides, and storm surges. The models extend from the beach to the continental slope, and they include a free surface, realistic coasts and bottom features, river runoff, and atmospheric forcing. A model is only a representation of the reality. As it is known analytic solutions of the equations of motion are difficult or impossible to be obtained for typical oceanic flows. The problem is due to the non-linear terms, friction, and the need for realistic shapes for the sea-floor and coastlines [BAUMERT 2005].

The advantages of numerical simulations compared to purely experimental investigation are quite obvious:

- Numerical results often are obtained faster and at lower costs.
- Parameter variations on the computer usually are easily realizable
- A numerical simulation often gives more comprehensive information due to the global and simultaneous computation of different problem-relevant quantities [SCHAFER 2006]

Like all systems numerical modeling has disadvantages. The problems that a numerical modeling faces are the following:

- Numerical models provide information only at grid points of the model. They provide no information about the flow between the points.
- Numerical calculations cannot be more accurate than the accuracy of the floating-point numbers and integers used by the computer. Unsharp errors cannot be ignored [RODI & LAURENCE 1999]
- The models can never give complete descriptions of the oceanic flows even if the equations are integrated accurately.

There is a world of difference between the character of the fundamental laws, on the one hand, and the nature of the computations required to breathe life into them, on the other [BERLINSKI 1996].

3 Data Acquisition

In this chapter the data acquisition is described. Mainly three types of data were required. Firstly, the meteorological data (water level, wind, waves) during the period of the research are presented. Secondly, the instruments with which current data were obtained are presented. Finally, the instrument for the mapping of the bed relief and for the sediment characteristics is described.

3.1 Experiment Set-up

The main objective of this campaign was to determine the sea surface currents by radar measurements at the Northest tip of the Sylt Island in the tidal channel Lister Tief. The instrument that was used for the acquisition of the sea-surface currents was the RDCP described in section 3.3.1. Vertical current profiles and water depth were collected using a ship-borne ADCP; the data of the ADCP were collected at a rate of one sample per 3 sec. Moreover the sea bed relief and the sediment characteristics were achieved by a multi-beam echo sounder.

The campaign took place in the spring of 2007 (May and June) and the area of interest was divided into five zones (figure 3-1). Several cross section with duration approximately 20–30 min each, were established. The direction of the ship was from West to East and the opposite direction.

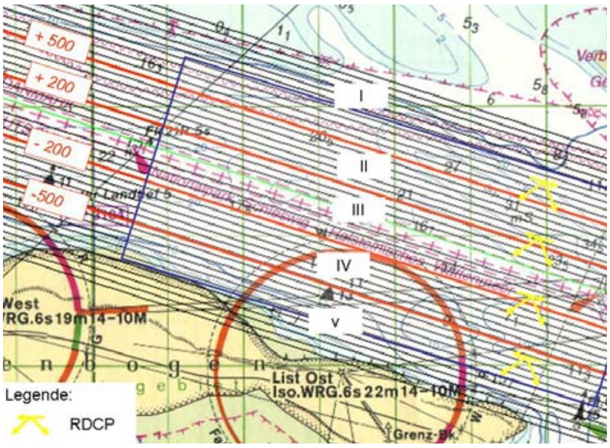

Figure 3-1. Division of the area of investigation into 5 zones, (source base map: TOP50 Schleswig Holstein and Hamburg).

3.2 Meteorological data

Typical stations along the coast provide wind speed, wind direction, air temperature, barometric pressure, rainfall and water temperature data. These basic measurements give us important information for predicting the coastal circulation, upwelling and changes to the weather and climate.

3.2.1 Wind data

Wind information for the period of the experiment was provided by German weather Service (Deutsche Wetterdienst DWD). The tide gauge station is located to the Lister Port in Sylt (figure 3-2) with coordinates 54.97N 8.467E.

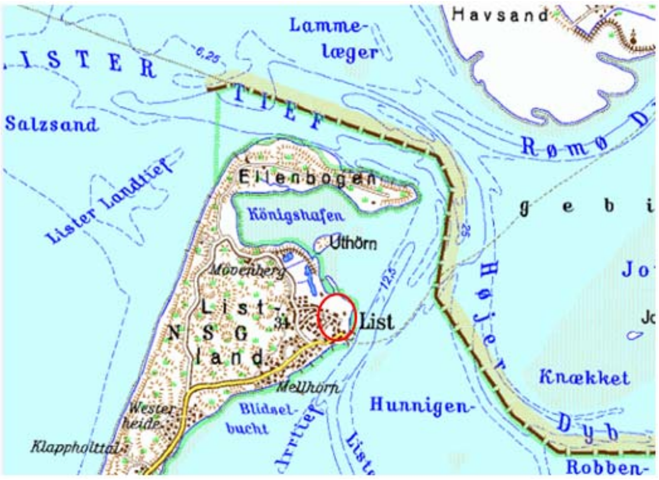

Figure 3-2. Tidal gauge station in Lister Port,
[source base map: TOP50 Schleswig Holstein and Hamburg].

The wind data presented in figures 3-3, 3-4 show mean wind velocities in the order of 5 m/s and mean wind direction 158^0 acting on the region during the end of May 2007 and the start of June 2007.

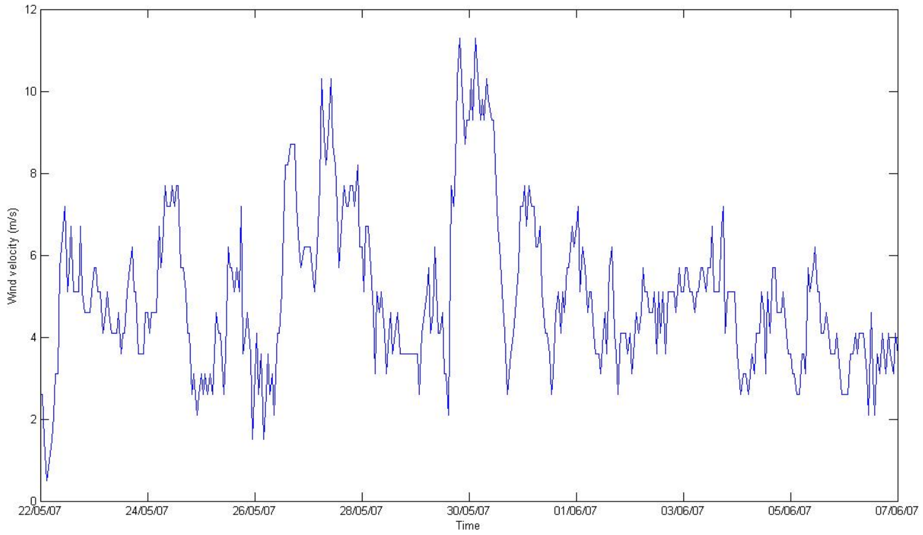

Figure 3-3. Time series of wind velocity in the monitoring station Lister Port (DWD).

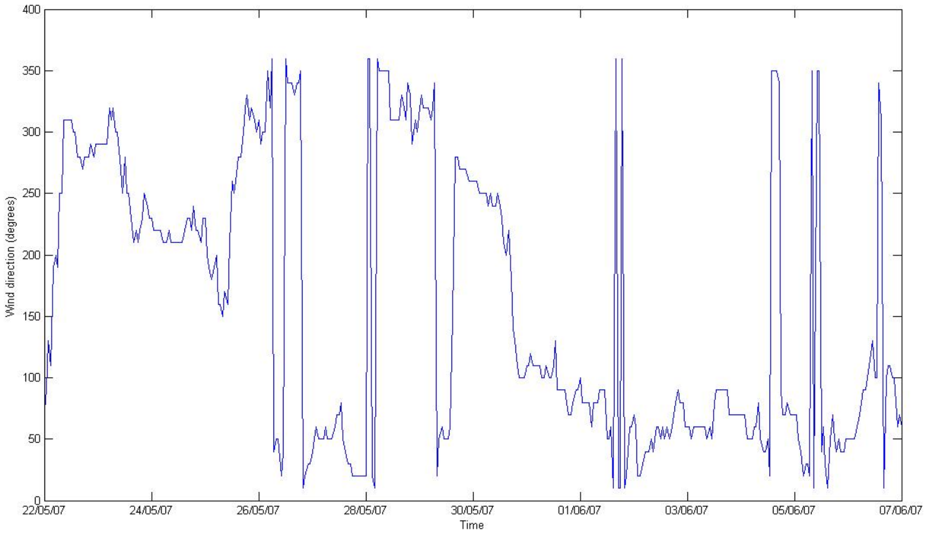

Figure 3-4. Time series of wind direction in the monitoring station Lister Port (DWD).

3.2.2 Water level

Water level measurements in the area of investigation were provided by DWD and Wasser Schiffahrts Amt (WSA). The tide gauge station is located in the position like the wind monitoring station in Lister Port. The tidal records governing the period of the campaign, 22th May – 7th June 2007, are presented in figure 3-5. The water level data were recorded with 1min interval. The only corrections were made to the data was the transformation from the NN time zone system to the UTC time zone system.

As it has been mentioned from previous researches in the area of interest the tidal range is 1.8 m/s, this is obvious in the figure 9.

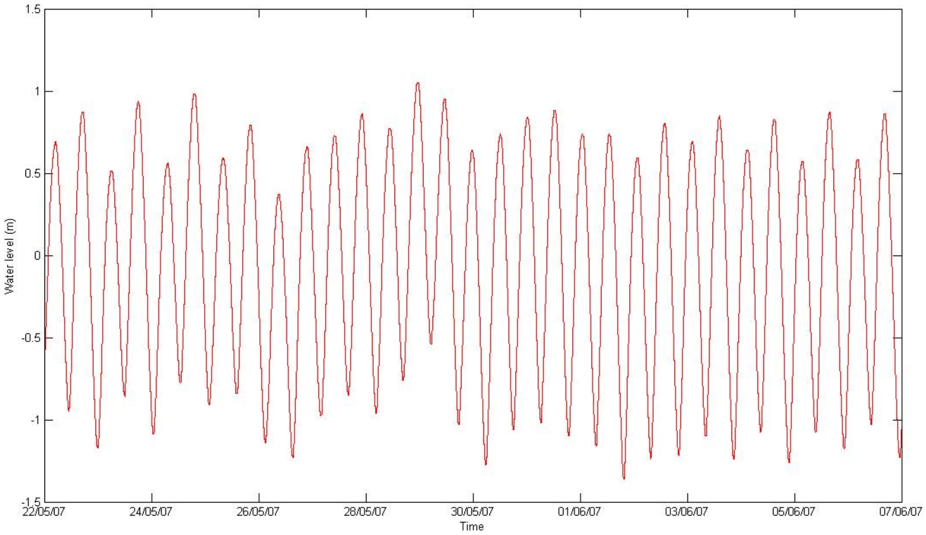

Figure 3-5. Water level measurement of the monitoring station in List Port [DWD, WSA].

3.2.3 Waves

The wave data time series were provided by the Landesbetriels fur Kustenschutz, Nationalpark und Meeresschutz (LKN). The wave buoy is located in Westerland 18 km southern from the area of investigation. In figure 3-6 the significant wave height, Hs, is illustrated during the period from 22th of May until the 7th of June. The measurements show moderate sea conditions for the entire period with an exception on the 30th of May; during this period the wave exceeds 2 m. This high peak indicates influence of the strong westerly breeze in the area, 11.8 m/sec wind speed and 280^0 mean wind direction, for that day.

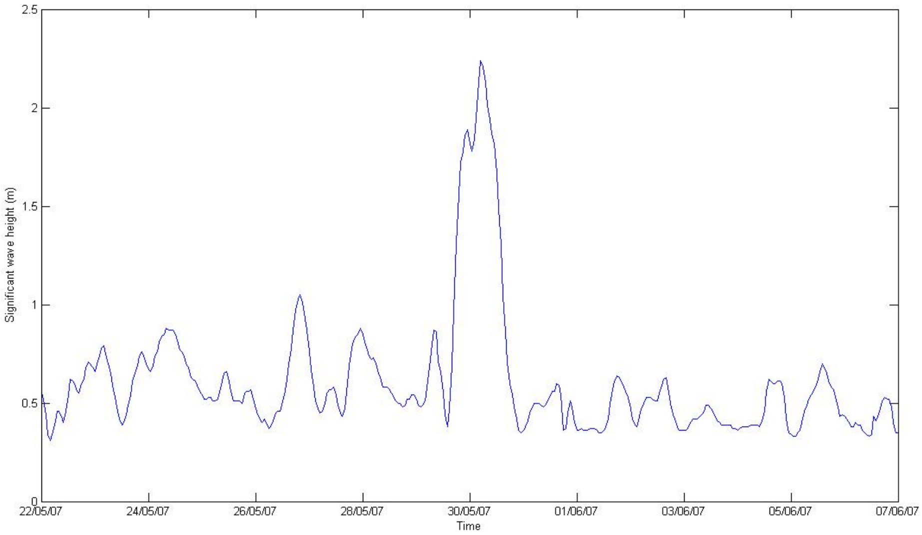

Figure 3-6. Significant wave height.

3.3 Current data

Measurements of currents are inherently more complex than temperature or density because current is a vector rather than a scalar quantity. Motion of water in the ocean is a fundamental feature that underlies transport and mixing of heat, salt, chemical species, and suspended particles [PICKARD 1990]. Observations of currents have progressed from point measurements to profiles and to surface maps.

3.3.1 Radar Doppler Current Profiler

The following section describes an innovative, recently presented method for the measurement of the sea surface current filed, based on the Doppler effect of the transmitted microwave pulse due to the surface current; analogue system is the ADCP. The system is a combination of a hardware and software developed by the Radar Hydrography department of GKSS (BRAUN et al., 2008, ZIEMER & CYSEWSKI, 2006).

The hardware of the system is consisted by two dopplerized X-band radars and a computer for their control. The radar has been developed in cooperation between the Electro technical University St. Petersburg, Russia, and the Institute for Coastal research, GKSS, Germany. The product of the method is the measurement of the surface current velocity field. In principle the current detection is based on the Doppler Effect of the transmitted microwave pulse due to the surface current field;

similar to the ADCP measurement for the water column. The hardware of the system is a combination of two nautical X-band radars. Each radar has been significantly modified, allowing the detection of the phase shift for each range cell of the received radar pulse and the calculation of the Doppler frequency shift caused by the scatter movement. The main change of the nautical system is the coherization of the transmitter-receiver to detect the Doppler frequency shifts in 250 cells (7.5 m each, and this resulted in a theoretical range of 1875 m) along a radial beam. The wave length of the electromagnetic signal is $\lambda_{radar} = 3$ cm. The RDCP is ship-based system (figure 11), the two radars have fixed staring direction perpendicular to each other to acquire the full vector of the current velocity during the passing of the ship. For each radial bin of 15 m length the radial velocities are calculated by the Doppler basic formula from the backscattered radar signal. The main advantage of the method is the area coverage. During data acquisition a precise differential GPS navigation system is used for the positioning of the ship to collocate the two current components in a post processing step and to correct the instantaneous antenna movements due to the pitch and the roll movements of the ship. The data were acquired with an antenna height of 9 m during a 20 minutes ship's survey from West to East. A wind sensor is responsible for the wind corrections of the output data. The radars scanned towards north or south producing a stripe of about 500 m width. The radial velocities from the backscattered signal are calculated by the Doppler relation for each range bin.

$$f_d = \frac{2v_r}{\lambda} = \frac{2f_t v_r}{c} \qquad (2)$$

f_d = Doppler frequency sift

v_r = vcosθ, where v is the speed, or magnitude of the vector velocity

θ = the angle between the target's velocity vector and the radial line of sight to the target

λ = total number of wavelengths

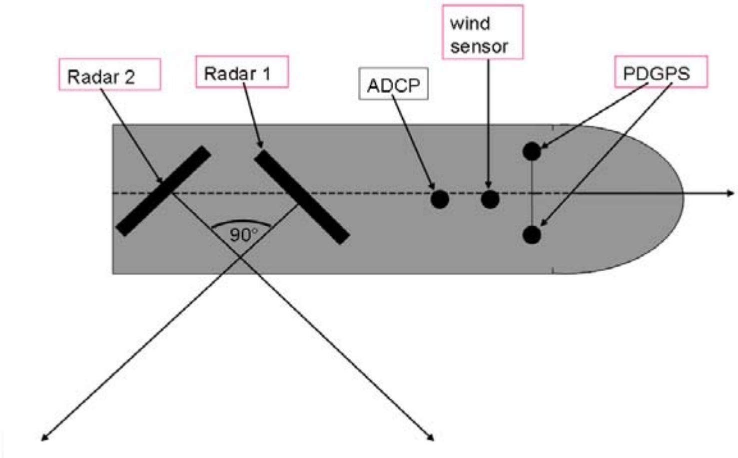

Figure 3-7. The hardware system of RDCP, (Image source: KOR, GKSS).

3.3.2 Acoustic Doppler Current Profiler

The Acoustic Doppler Current Profiler has been commercially available for about 25 years. It is currently being used for oceanography, estuary, river and stream flow current measurement**.** An ADCP is a type of an acoustic instrument that produces a record of water current velocities over a range of depths [RD Instuments]**.** The measurements are obtained by propagating a fixed frequency sound wave (10 μS) of high frequency through the water column and computing the Doppler frequency shift on echoes from suspended particles [DOUGLAS 2003]. The method assumes that these particles are moving with the same velocity as the water. Evaluating the travel time of the signal is possible to obtain the velocity components (U and V) along the vertical profile. Furthermore, the depth range of a given profile is influenced by the density of scatters, the presence of bubbles under the transducer and the noise generated by the propellers and by flow along the hull.

In the present experiment vertical profiles of the velocity have been measured by the ADCP, WH-Zedhead from RD Instruments of San Diego, with frequency 1200 kHz. The ADCP was mounted on the bottom of the vessel and is consisted by four downward independently working acoustic beams with each beam angled 20 degrees from the vertical axis of the transducer assembly (figure 3-8). The current velocity profiles have been recorded from a water depth 2.5 m below the water surface to 1.2 m above the seabed; separated into depth cells (bins) of 0.25 m length each. The velocity was measured relative to the reference frame of the instrument. Because the ADCP was mounted on a boat, the corrections for the boat’s velocity were made by partial deferential GPS. Ensembles of data are collected for brief periods at intervals on the order of 3 sec, regardless of the distance travelled by boat. Each ensemble of data gives information about the velocity magnitude and direction, water depth, temperature, boat displacement, heading and several other parameters related with the data quality.

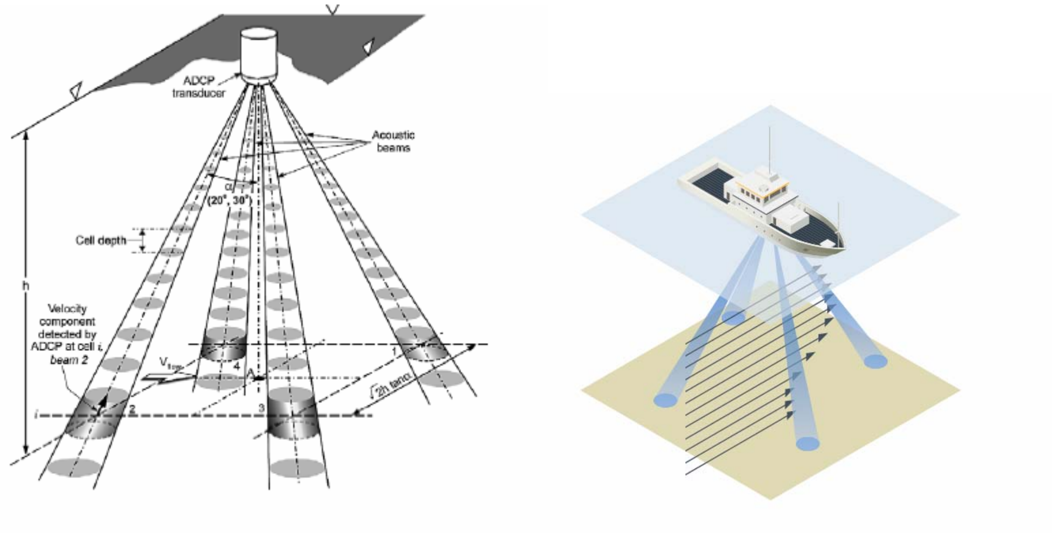

Figure 3-8. a) ADCP b) vertical profile from a moving vessel.

3.4 Multi-beam Echo Souder (Bed Relief and Sediment characteristics)

The bed relief of the area was measured by coupling MBES technique with high accuracy positioning system. The sea floor map was established by means of the multi-beam echo sounder EM 3000^{TM} from Simrad-Kongsberg. The minimum operating depth is 1 m below the sonar head and in typically sea water conditions the depth range can exceed 150 m. The used frequency is of range 300 kHz with a ping repetition rate of 15 kHz. The nominal apex angle is 1.5^0 along track and 120^0 across track during transmission. During the receiving the nominal angle is 30^0 along-track and 15^0 across track. The swath width is of the range 64 m at a water depth equal to 18.5 m. The spatial resolution of the multi beam echo sounder is equal to 2 m [STOCKMANN 2009].

4 Data Analysis

The data sets from the multi beam echo sounder and RDCP are post processed and available. As it was mentioned in the description of the multi beam echo sounder the grid size of the produced terrain model is 2 m x 2 m. On the other hand, the radial bin of RDCP is equal to 15 m. The datasets from both instruments have been re-gridded on a common mash size, with spatial resolution 15 m. Local gradients in both sets of maps (bathymetry and current speed) are calculated. After the localization of the maxima in the gradients of the scalar fields the positions of the highest change in the surface current values are correlated with the position of the sand dunes crests. This analysis is accomplished for both tidal phases.

4.1 Bathymetry

A bathymetric map shows the sea floor relief or terrain as contour lines (called depth contours or isobaths). The bathymetric map of the area was created, by the measurements obtained from the multi-beam echo sounder, in the environment of ArcGIS 9.2. In order to display the sea floor topography a Digital Elevation Model, (DEM) was created. The DEM is a computerized representation of an elevation surface. Specifically, the DEM is a raster in which the value in each cell represents the surface elevation at that location in the scene.

The DEM (figure 4-1), was created with a raster resolution equal to 15 m, to match it with the resolution of the RDCP as the measurements (echo sounder and radar) should be projected in a same geo-referenced grid. A map with the isolines of the depth in the area of research was also created with interval equal to 2 m (figure 4-2). The projection coordinate system is the Gauss Krueger system.

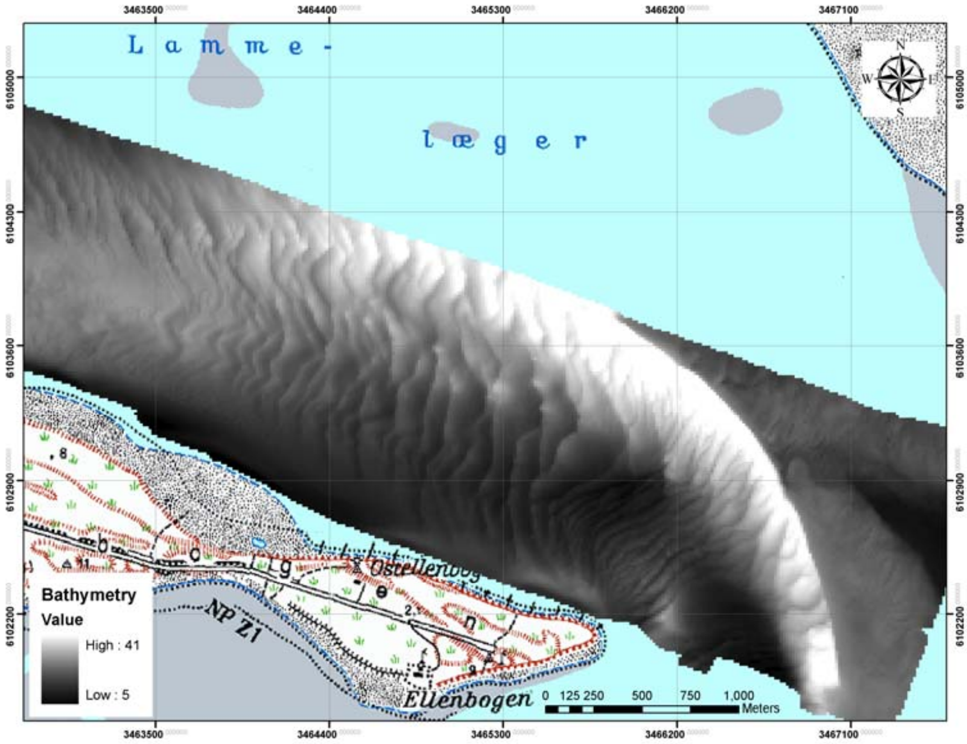

Figure 4-1. Digital elevation model of Lister Tief,
[source base map: TOP50 Schleswig Holstein and Hamburg].

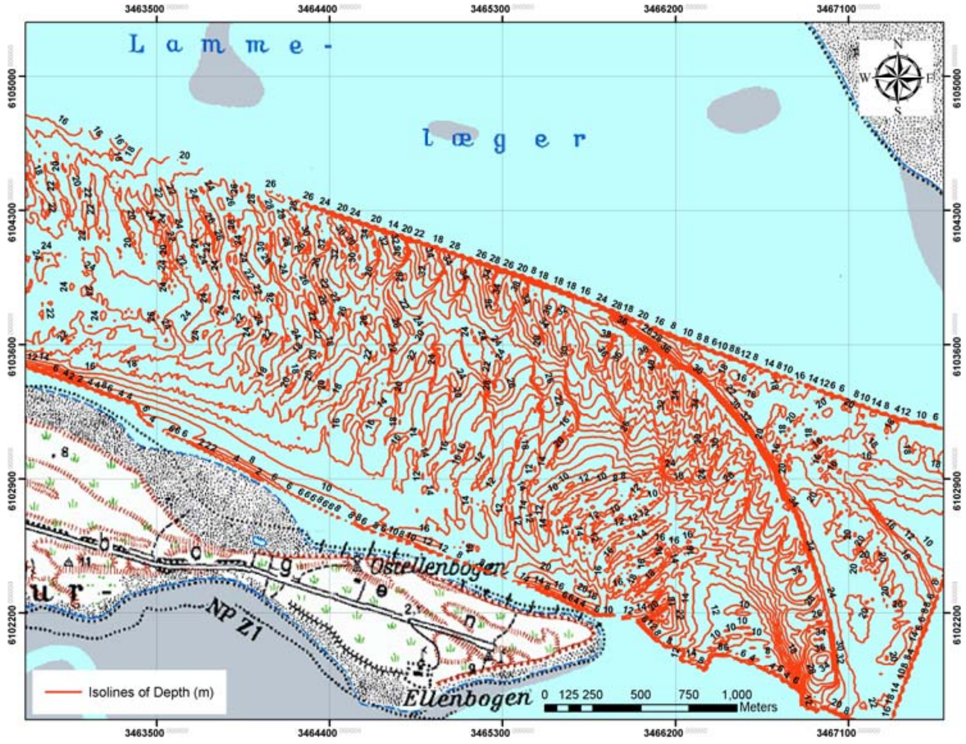

Figure 4-2. Isolines of depth in Lister Tief,
[source base map: TOP50 Schleswig Holstein and Hamburg].

4.1.2 Slope

In many cases the information about the slope of the ground is useful. Slope identifies the steepest downhill slope for a location on a surface. Slope is calculated for each cell in a raster. For raster surfaces, slope is the maximum rate of change in elevation over each cell and its eight neighbors. Every cell in the output raster has a slope value. The lower is the slope value, the flatter the terrain; the higher the slope value, the steeper the terrain [ESRI USER GUIDE]. The output slope raster is calculated as percent of slope or degree of slope. The slope of the bathymetry of Lister Land Tief was calculated in degrees (figure 4-3). The steeper parts of the area are with dark brown color and with light yellow color are the less steep nearly to flat areas. According to the data the highest values of slope is of range 20^0–27^0 and were observed at the eastern part of the area of interest as it was expected as it is the deepest part of the area.

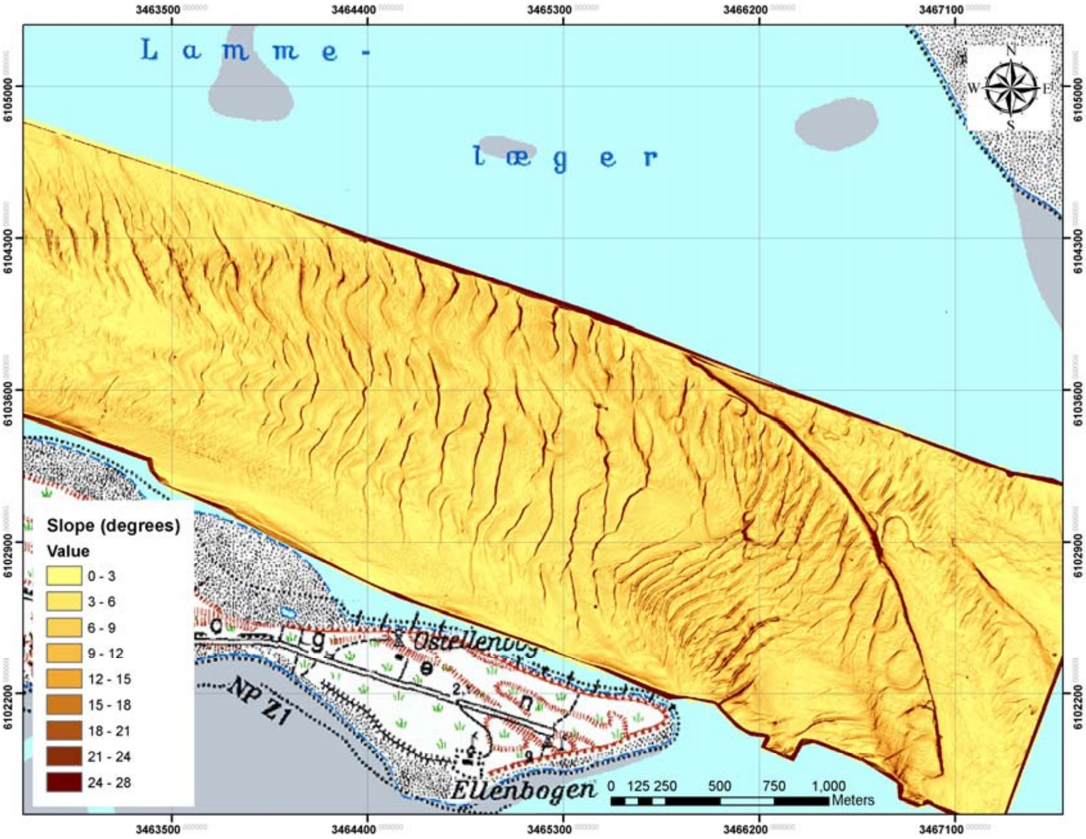

Figure 4-3. Slope of the Lister Tief,
[source base map: TOP50 Schleswig Holstein and Hamburg].

4.2 Determination of the Surface Current Speed

The measured components of the surface current velocity from the RDCP, Ux and Uy, (x-direction corresponds to East and y- to North) are written into a geo-coded grid. In the following lines post processing procedure of composing the full surface current vector by merging the two components into a common grid is analyzed.

The output of the RDCP is the surface current field into x and y components. The current magnitude of each vector was calculated by the formula

$$\mathrm{U} = \sqrt{U_x^2 + U_y^2} \tag{3}$$

And the direction with the formula

$$\tan(a) = \frac{U_x}{U_y} \tag{4}$$

In the environment of ArcGIS the visualization of the current magnitude and the current direction was implemented with the IDW method. Two hundred fifty dataset from the RDCP where visualized and five datasets were chosen to be discussed. Identification numbers of the five selected data sets are 252, 292, 318, 346 and 392. All of them are during flood phase (Table 4-1), the datasets during ebb phase, due to technical difficulties and environmental ambiguities were not suitable for further analysis. The values of the current magnitude to the area of investigation based on past experiments do not exceed the value of ± 2 m/s; the data were filtered with this value and the exceed current magnitudes were excluded.

Table 4-1. Characteristics of selected datasets.

Dataset	Zone	Tide phase	Date	Time	Hours after low tide
252	4	Flood	29.05.2007	12:10-12:34	LW+4
296	5	Flood	31.05.2007	13:48-14:14	LW+5
318	3	Flood	01.06.2007	11:22-11:44	LW+2
346	3	Flood	02.06.2007	12:08-12:34	LW+2
392	4	Flood	05.06.2007	13:24-13:58	LW+2

The spatial plots for the surface current speed and direction were created by the interpolation method Inverse Distance Weighted. IDW was used because the data sets from the RDCP are dense enough and can capture the extent of the local surface variations. IDW is a simple method of interpolation that estimates cell values by averaging the values of sample data points in the neighborhood of each processing cell. The closer a point is to the center of the cell being estimated, the more influence it has in the averaging process [LONGLEY & BATTY 1996]. Therefore, the assumption is that the neighboring data samples are more alike than those that are further apart. For the cells that there is no measurement, IDW uses the measured values that are surrounding them, the missing data are mainly to the boundaries of the RDCP results grid. The simple function of the IDW algorithm according to Shepard (1968) is:

$$w(d) = \frac{1}{d_p} \tag{5}$$

Where the

$w(d)$ = weight indicator

d = distance

and p = the power parameter (p>0)

The characteristics of the surface are controlled by a fixed search radius and by the power parameter. A fixed search radius requires a neighborhood distance and a minimum number of points. The distance presets the radius of the circle of the neighborhood (in map units). The distance of the radius is constant, so for each interpolated cell, the radius of the circle used to find input points is the same. The power parameter controls how the weighting factors drop off as distance from the reference point increases [LONGLEY & BATTY 1996] and the value is specified by the user. Specifying a lower power will give more influence to the points that are farther away, resulting in a smoother surface. By defining a higher power, more emphasis is placed on the nearest points, and the resulting surface will have more detail (be less smoothed).

For the spatial surfaces that were created the weight power parameter was to be 1, the fixed search radius equal to 25 m, due to the fact that the input data samples from the RDCP are plentiful and are regularly spaced every 15 m. In addition the output raster cell size is equal to 15 m. The following figures 4-4 – 4-7, illustrate examples of the surface current speed and direction of two dataset, 346 and 296, from the RDCP. The rest of the five datasets can be viewed in the Appendix.

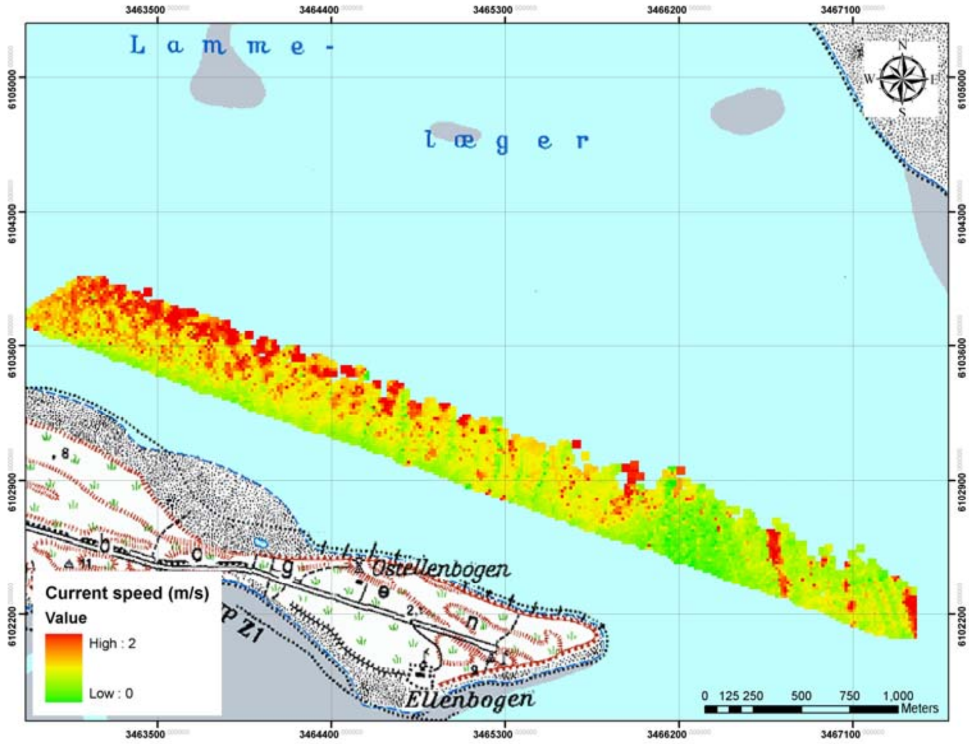

Figure 4-4. Spatial plot of surface current speed of the RDCP dataset 346, [source base map: TOP50 Schleswig Holstein and Hamburg].

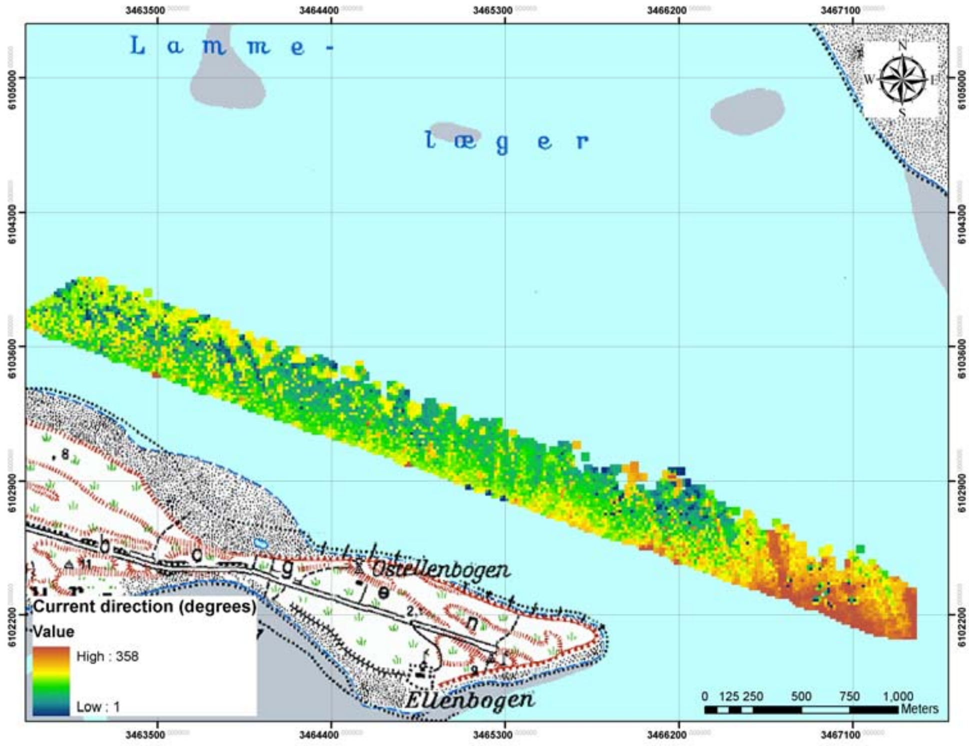

Figure 4-5. Spatial plot of the surface current direction of the RDCP dataset 346, [source base map: TOP50 Schleswig Holstein and Hamburg].

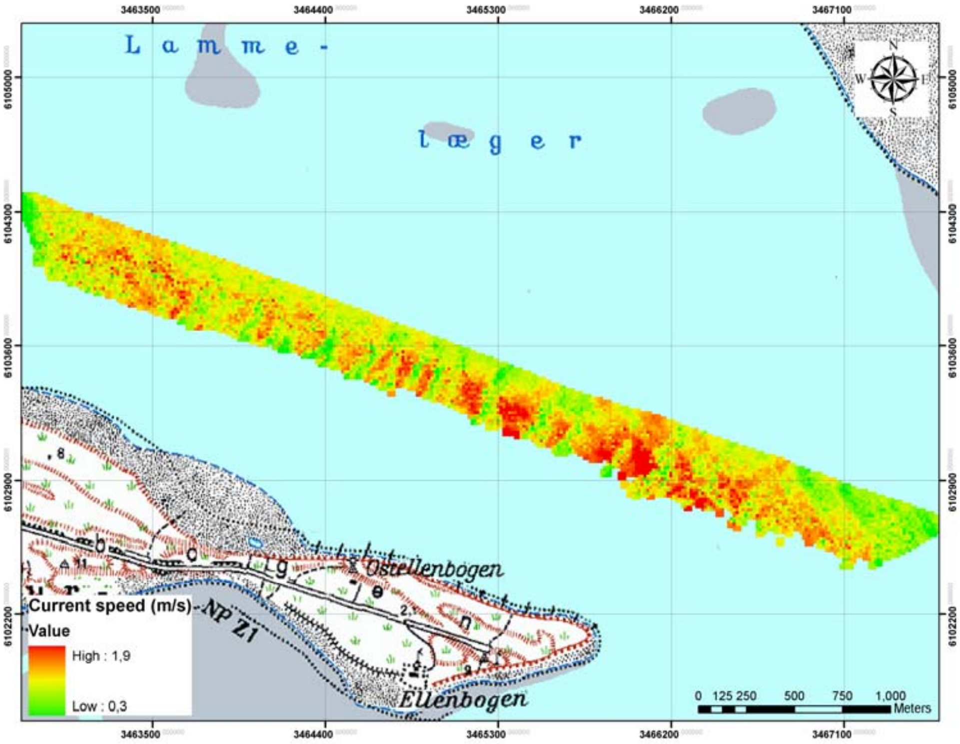

Figure 4-6. Spatial plot of surface current speed of the RDCP dataset 296, [source base map: TOP50 Schleswig Holstein and Hamburg].

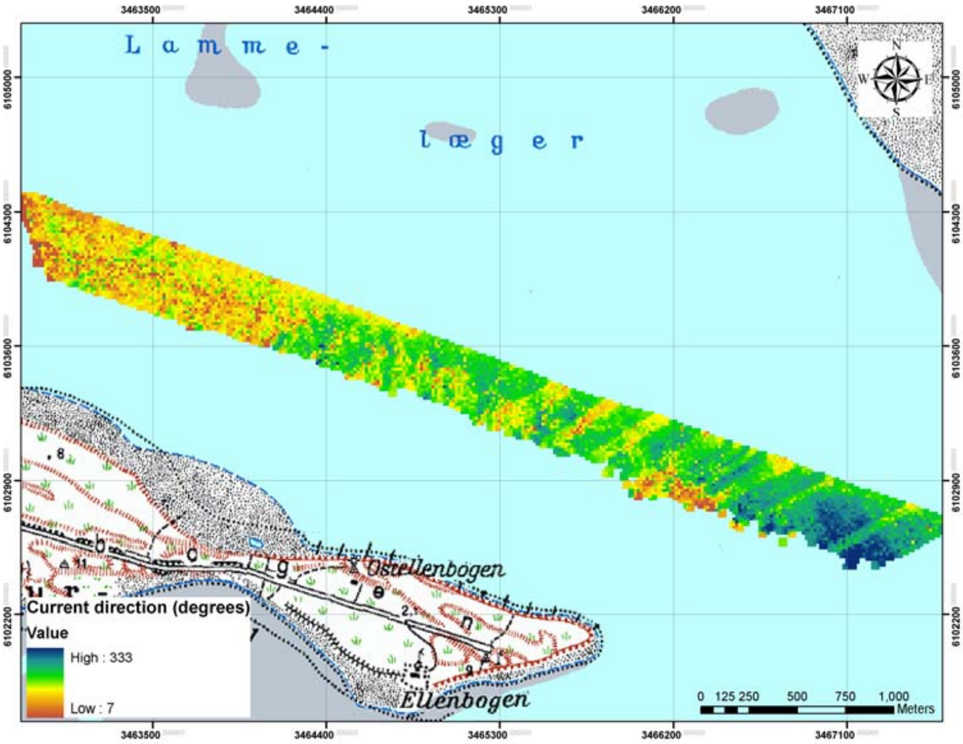

Figure 4-7. Spatial plot of surface current direction of the RDCP dataset 296, [source base map: TOP50 Schleswig Holstein and Hamburg].

The next step is the calculation of the effect of the space gradient of velocity, in x and y direction, that is being transported together with the water flow. The acceleration of the current speed in space was calculated because the gradient of the current velocity plays an important role at the radar imaging mechanism of sea bottom topography [HENNINGS 2004]. It is assumed that the law of conservation of mass is valid, so it is expected that over the crests of the sand dunes, the water mass accelerates (figure 4-8).

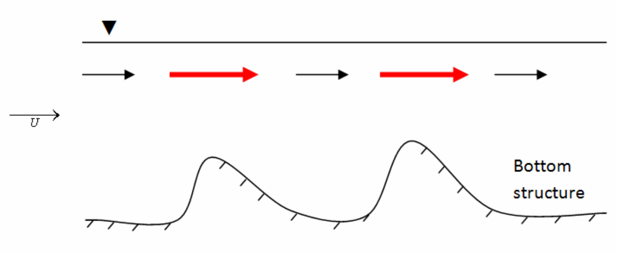

Figure 4-8. Vertical cross section of water flow and the expected changes of the current speed.

The calculation of the ∂Ux/∂x and ∂Uy/∂y was implemented with spatial surfaces in the environment of ArcGis. In contrast to the surface plots of the surface currents speed and direction were IDW was used, for the acceleration was made use of the term slope. For the creation of the spatial plots of the localization of the acceleration, the slopes of the surface currents speed components were calculated into percentage. Afterwards, they were divided by 100 in order to have the acceleration into m/sec^2 and not in percentage. In a raster surface of a slope, if a value of one cell is equal to 45 degrees if you convert it in percentage it will be equal to 100 %. If the value of the slope is equal to 90 degrees then the percentage of the slope it tends to infinitive

Except of the above analysis for the detection of the correlation between the bathymetry and the surface current speed field some additional analysis were carried out. Due to the mass conservation law, the current speed in shallow waters should be higher than in deeper waters. The concentration of the investigation was focused on the area that anomalies of the surface current speed were observed, this area was the same for all the datasets that were examined.

In order to measure parallel the changes of the surface current speed, the local acceleration, the bathymetry and the slope, cross-sections were defined by the user (different from those of the ADCP). The cross-sections were located in the central part of the area of investigation, were irregularities in the magnitude of velocity over big sand dunes were observed. The lengths of the cross-sections defined by the user for the RDCP's datasets, 296 and 346, were 1.338 m and 2.000 m respectively and oriented from West to East (like the track of the ship during the campaign).

4.3 Analysis of the Vertical velocity profile

The analysis of the current vertical profile was obtained by the collected data from the moored ADCP on the vessel. The ADCP was configured to record an ensemble of data (depth and vertical velocity profile) every 3sec, with bin size resolution 0.25m. The ADCP records horizontal velocity components relative to compass directions for each cell north and east. For each cell, the total horizontal velocity was resolved into stream wise U and transverse V components. The first velocity measurements were collected at the depth of 2.5 m beneath the sea surface. The ADCP measures the total depth of one water column but except near sea bottom boundary. Velocities near solid boundaries and free surfaces cannot be measured with ADCP's because of interference in the acoustic signals resulting from boundary reflectance. As a result, for an angle of 20 degrees between the transducer beam and the vertical, the velocity measurements in the lower 6 % of the distance from the ADCP to the reflecting surface are highly unreliable [GONZALEZ 1996].

The total horizontal distance of the transect, for the ADCP datasets 296 and 346 was 5.320 m and 6.108 m respectively. In the collected data files the following parameters are recorded, date, hour, depth, length of the cross-section, easting and northing coordinates in meters, the averaged velocity of each vertical layer, the East-West (U) and the North-South (V) velocity of currents relative to the ship, for each bin, the direction, and quality control of each bin.

The basic processing of the ADCP data involves removing pitch, roll, and heading variations from the velocity data; correcting for speed of sound; subtracting the ship's velocity from the data; and finally averaging the data in space or time. The collected data were pre-processed with the commercial software RDI WinRiver. The data were exported in ASCII format from WinRiver and then program algorithms were written, in Matlab, for the final processing.

High velocities near the bed often indicate an ambiguity in the phase measurement for velocity, and produce an opposing vector direction of unrealistic magnitude which is not correctable after acquisition [GORDON 1996]. The ADCP manufacturer suggests that one measurement is good when the quality control of each bin is equal to 100 %. The first filtering extracted empty ensembles, which were easily identified by a full set of null values, and measurements that the parameter of the quality control was less than 100 %. After the extraction of the dummy measurements, the data were sorted into a grid with X-coordinate the length of the cross section and Y-coordinate the relative depth. The velocity of the lowest bottom cell, which extends from the last cell measured by the ADCP to the streambed, was settled equal to 0 (this allows to make a linear interpolation and to find the values of intermediate points). In order to have a first impression of the variability of the velocity along the cross section, the mean velocity of each water column versus depth was calculated. Afterwards, the data were vertically averaged for ten sequential profiles and horizontally for one meter (four bin cells), in order to produced a smoother grid. The averaged velocities and direction were visualized over bathymetry by displaying vector ensembles colored according to vector magnitude and direction. From these visualizations, the variability of the velocity magnitude and the changes in direction through the water column, over the seabed topography can be assessed. The accuracy of the ADCP is ± 0.5 m/s.

5 Development of a Hydro-dynamical model

A two-dimensional depth integrated model covering the area of investigation was developed on the basis of Delft3D developed by WL Delft Hydraulics in the Netherlands. A system of nonlinear (hyperbolic or parabolic) partial differential equations using the shallow water and the Boussinesq approximation are solved. The system of equations is derived from the three-dimensional Navier-Stokes equations for incompressible free surface flow under shallow water. Vertical accelerations are neglected leading to the hydrostatic pressure equation. The equations, in combination with an appropriate set of initial and boundary conditions, are solved on a finite difference grid [DELFT 2007]. Two-dimensional flow models are based on the following equations:

Continuity/Mass balance equation:

$$\frac{\partial h}{\partial t} + \frac{\partial}{\partial x}(h\bar{u}) + \frac{\partial}{\partial y}(h\bar{v}) = 0 \qquad (6)$$

Momentum balance equation in x-direction:

$$\frac{\partial}{\partial t}(h\bar{u}) + \frac{\partial}{\partial x}(h\bar{u}\bar{u}) + \frac{\partial}{\partial y}(h\bar{u}\bar{v}) + gh\frac{\partial}{\partial x}(h + z_b) \pm k_x h(\frac{\partial^2 \bar{u}}{\partial x^2} + \frac{\partial^2 \bar{v}}{\partial y^2}) - \frac{\tau_{bx}}{\rho} - \sum \frac{F_x}{\rho} = 0 \, (7)$$

Momentum balance equation in y-direction:

$$\frac{\partial}{\partial t}(h\bar{v}) + \frac{\partial}{\partial x}(h\bar{v}\bar{v}) + \frac{\partial}{\partial y}(h\bar{v}\bar{u}) + gh\frac{\partial}{\partial y}(h + z_b) \pm k_y h(\frac{\partial^2 \bar{v}}{\partial x^2} + \frac{\partial^2 \bar{u}}{\partial y^2}) - \frac{\tau_{by}}{\rho} - \sum \frac{F_y}{\rho} = 0 \;\; (8)$$

Where:

$\bar{v}$, $\bar{u}$ = fluid velocities in y, x – directions (m/s)

h = water depth (m)

ρ = fluid density (kg/m^3)

t = time (s)

k = effective dispersion coefficient

z_b = bed level above reference datum (m)

τ_{bx}, τ_{by} = bed shear stress in x, y directions (N/m^2)

F = External driving force (wind, waves, Carioles')

5.1 Flow Model Set-up

5.1.1 Model Grid

The first and the most important step of the set up of the numerical model is the generation of the grid. The grid must be able to capture the real world and transfer it in the numerical model.

The strategy adopted for the creation of the grid was to have more nodes in the regions with higher gradient (water depths, current, and velocities). In the study area, high resolution of the grid is demanded in the area of the main channel of Lister Tief and the surrounding channels. The grid should follow the geometry, direction and changes of the bathymetry in the area of interest.

The curvilinear grid was generated under DELFT–GRID module. During the designing of an “efficient” numerical grid, several considerations regarding the user needs and the numerical scheme were taken into account. Firstly, the orthogonality which is defined as the cosine of the angle between the grid lines in M and N direction. The value of the orthogonality (cosφ) is recommended to be under 0.02 [DELFT 2007]. Secondly, the grid smoothness which is the ratio of the neighboring grid cell dimensions. A grid should be smooth enough to minimize errors in the finite difference approximation. The approved value for the smoothness is under 1.2. Finally, the grid resolution is defined as the square root of a grid cell area. The horizontal resolution of the grid depends on the characteristic length and scale of the bathymetry, the land water boundary and the flow patterns which are wished to be solved [DELFT 2007]. The three previous described properties are the main properties of a grid which are affecting the accuracy of the numerical solution. Steps of the construction of the grid are presented in figure 5-1.

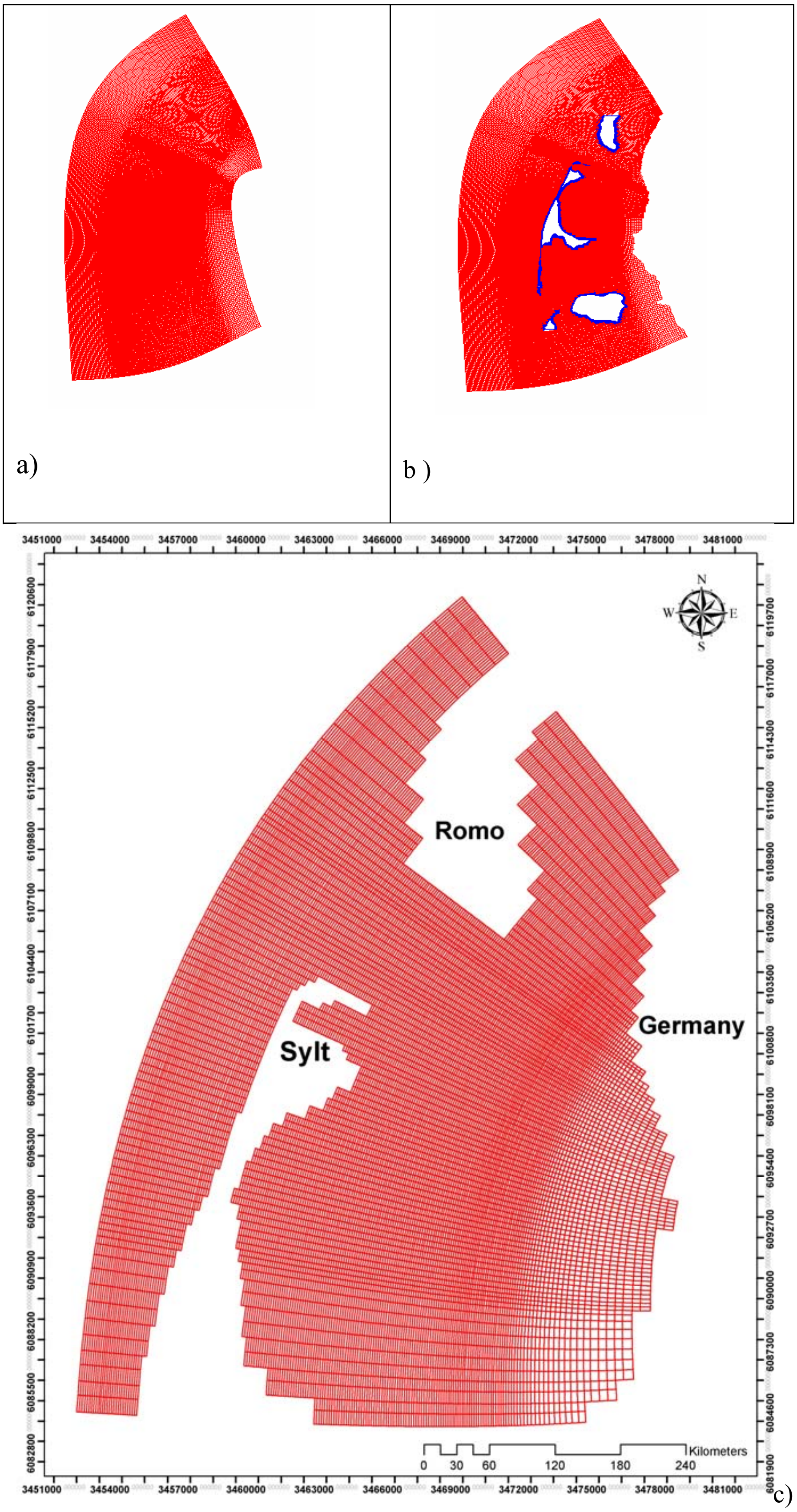

Figure 5-1. a) & b) Steps from the generation of the grid c) Reference grid.

The model domain covers an area of about 510.552 km^2 this includes the Sylt Island until Westerland, the south part of Romo Island, the north-west coastline of Germany and a small part of Denmark. The reference curvilinear grid has a grid spacing from 90 to 130 m (figure 5-2b). The orthogonality (figure 5-2a) varied from 0.01–0.00 in the entire grid. In figure 5-3 the grid smoothness in M and N direction are visualized, with ranges of 1–1.07 and 1–1.37 respectively.

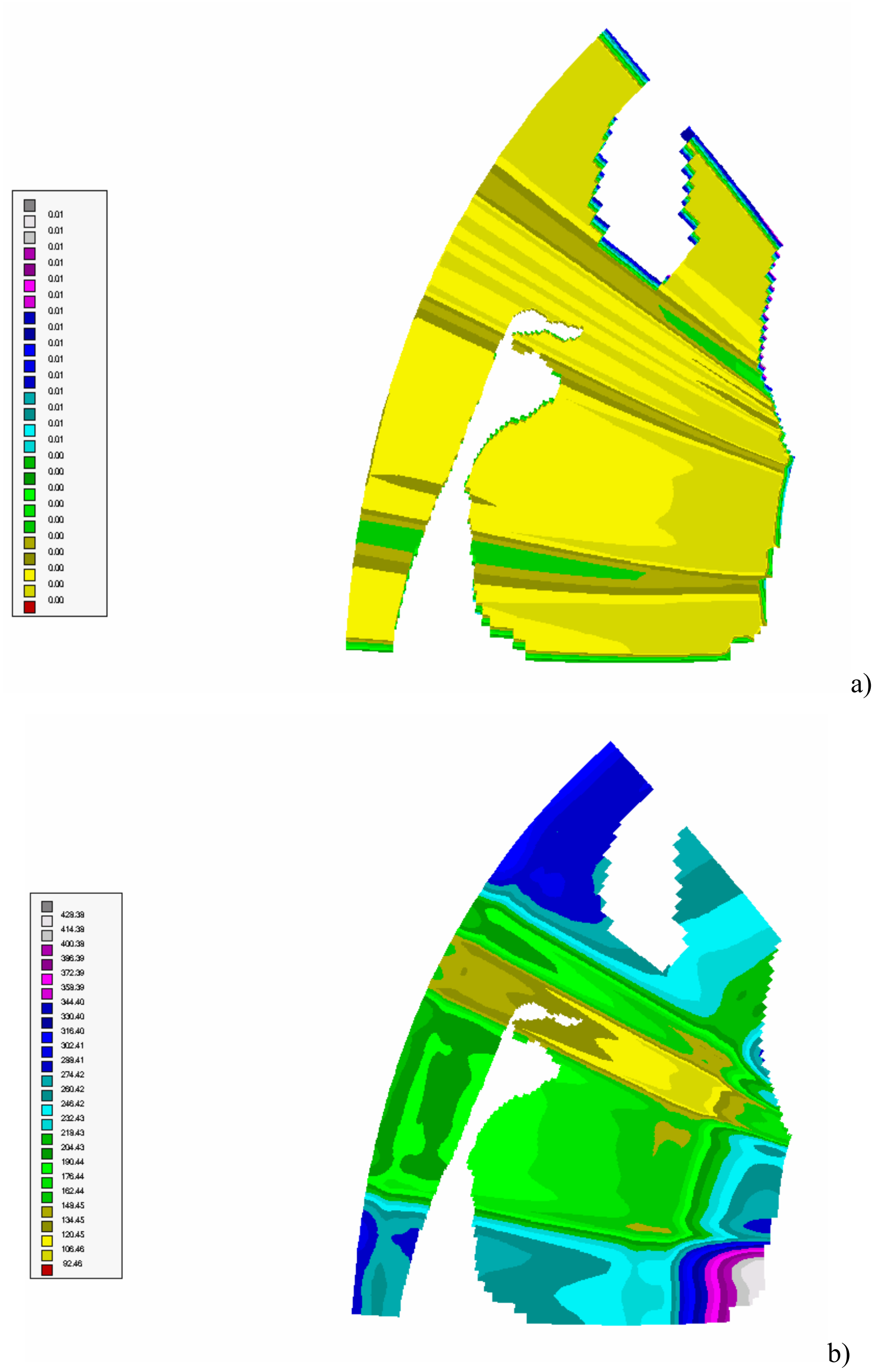

Figure 5-2. Orthogonality (a) and resolution (b) of the reference grid.

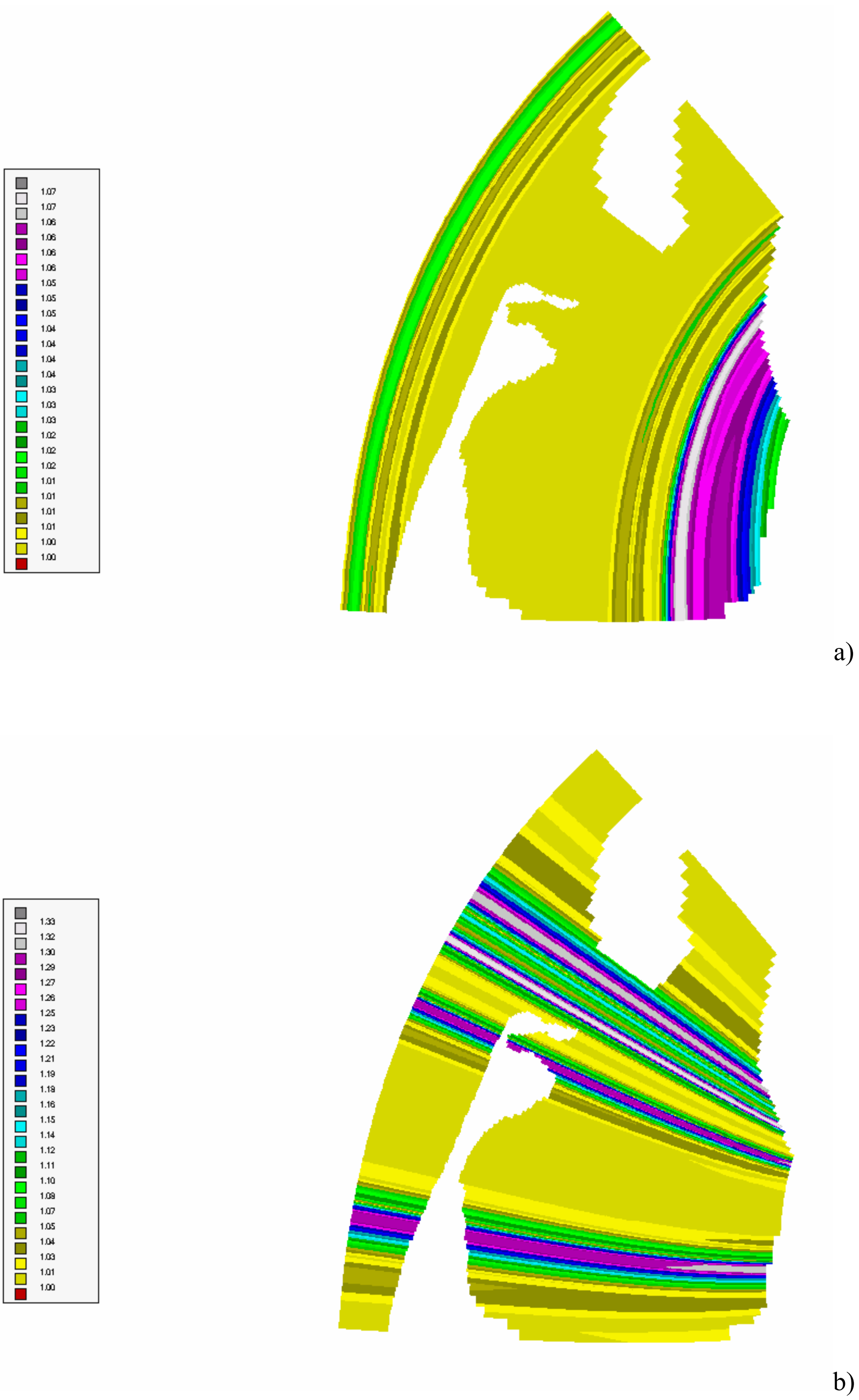

Figure 5-3. Smoothness of the reference grid in M (a) and N(b) direction.

5.1.2 Model Bathymetry

Two model bathymetries were created from bathymetrical datasets of 1994 and 2007 covering the whole model domain (figure 5-4 & 5-5) provided by the LNK, the BSH and the Danish authorities,. The resolution of the bathymetrical datasets was coarser than the model grid hence different interpolation methods, averaged interpolation and triangular interpolation, were used to generate the respective model bathymetry. For the dataset of 1994, where the sample points were dense "averaged interpolation" was applied.

The bathymetry of 2007 is a combination of the data provided by the previous mentioned institutes and the bathymetric samples obtained by the multi-beam echo sounder (see section 3.4), which cover only the area of interest with a resolution of 2 m. For the first dataset of 2007, the "triangular interpolation" was applied due to the fact that the points were scarce. For the multi-beam echo sounder the "averaged interpolation" was applied. Afterwards, the generated model bathymetry for each dataset was checked for irregularities like blank points. The internal diffusion method was applied to fill the blank points (missing) and to make the bathymetry homogeneous.

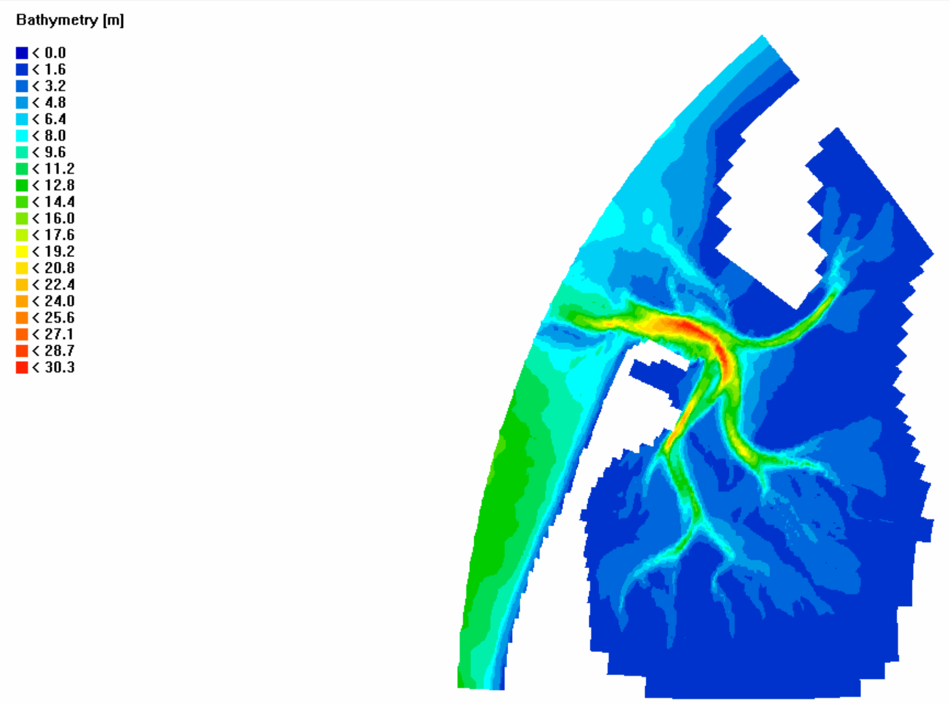

Figure 5-4. Model Bathymetry of 1994.

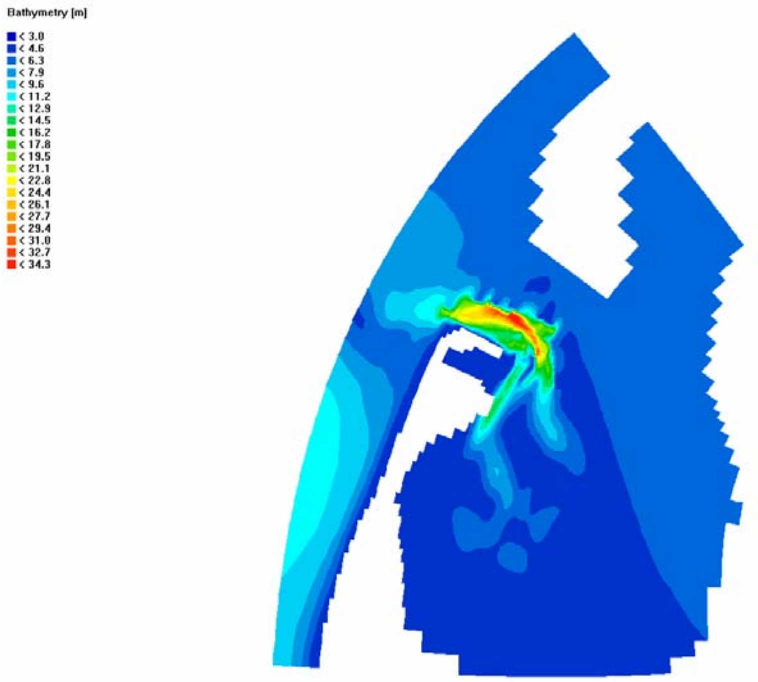

Figure 5-5. Model bathymetry of 2007.

5.1.3 Time Step

The time interval at which the results of the simulation are computed is called time step; it is given in minutes. The time step is highly connected with the grid cell cize. The time is checked through the Courant number, expressed with the formula [DELFT 2007]:

$$Cr = 2 \cdot \Delta t \cdot \sqrt{g \cdot H} \cdot \sqrt{\frac{1}{\Delta x^2} + \frac{1}{\Delta y^2}} \tag{9}$$

Where:

C_r = the Courant Number (-)

g = the acceleration due to gravity (m/s^2)

H = is the average depth (m)

Δt = the time step (s)

Δx = is the cell width in x direction (m)

Δy = the cell width in y direction (m)

The Courant number gives the velocity with which the waves with maximum celerity (or the fastest moving disturbance) can travel on the numerical grid. Formula 9, indicates that the Courant number is inverse proportional to the time step. Based on previous studies, Courant numbers larger than $4\sqrt{2}$ have as a result to produce instability to the model. On the other hand, large values of the time step minimize the computing time of the simulations.

5.1.4 Open boundary conditions

Open boundaries conditions represent the influence of the outer world i.e. the area beyond the model area which is not modeled. In a numerical model open boundaries are introduced to restrict the computational area and therefore the computational effort [DELFT 2007]. At an open boundary the flow and transport boundary conditions are required. The flow may be forced by imposing water level, currents, or discharges. The hydrodynamic forcing can be prescribed using harmonic or astronomical components or time series of measurements. Theoretically, the same type of boundary should be avoided, if there is more than one open boundary in the model area, because this may lead to continuity problems. In practice, the type of the open boundaries depends upon the available data.

The locations of the open boundaries should be selected very carefully, taking into account several parameters. The open boundaries should be located far away from the region of interest in order to avoid the wave's reflections. It is recommended the open boundarues to be located in deep water regions where the variation of the bathymetry is not as high as in shallow areas. If the gradient of the bathymetry is high, then the segment number of the open boundaries should increase, in order to capture these variations. Regions with high turbulence and sediment transport should be avoided. In addition a preferable location is where measurements are available.

In the model domain, besides the wide open boundary at the west part, a clear closed boundary is defined along the east part where the German and the Danish coast are located. The model domain with locations of the open sea boundaries are shown in figure 5-6. For prescribing boundary conditions along the domain's open sea boundaries, a nesting sequence has been employed, see section 5.5.

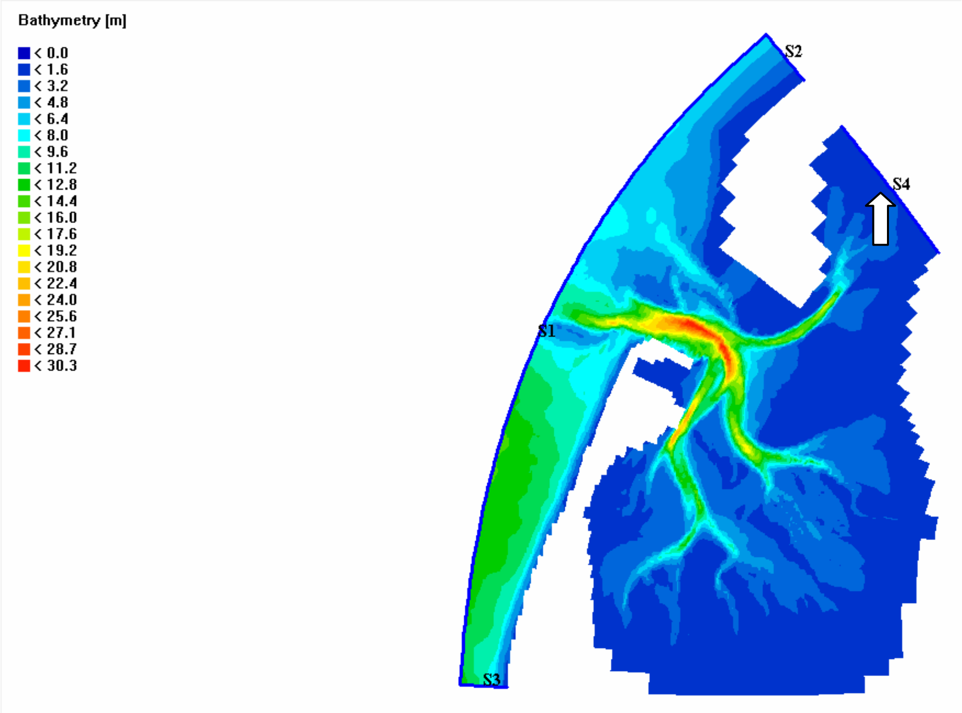

Figure 5-6. Open boundaries and land boundaries of the model domain.

5.1.4.1 Observation points

Observations points are grid locations where all the quantities computed during the simulations are stored at a user-defined time interval [DELFT-3D manual]. Observation points (figure 5-7) were set along the three channels, Lister Ley (south), Hojer Dyb (southeast) and Romo Dyp (northeast)., Romo, in the domain. The observations point “Station” (figure 5-8) was set in the position where measurements of water level and wind were available. The density of the observation points was higher in the area of investigation than in the rest modeled area.

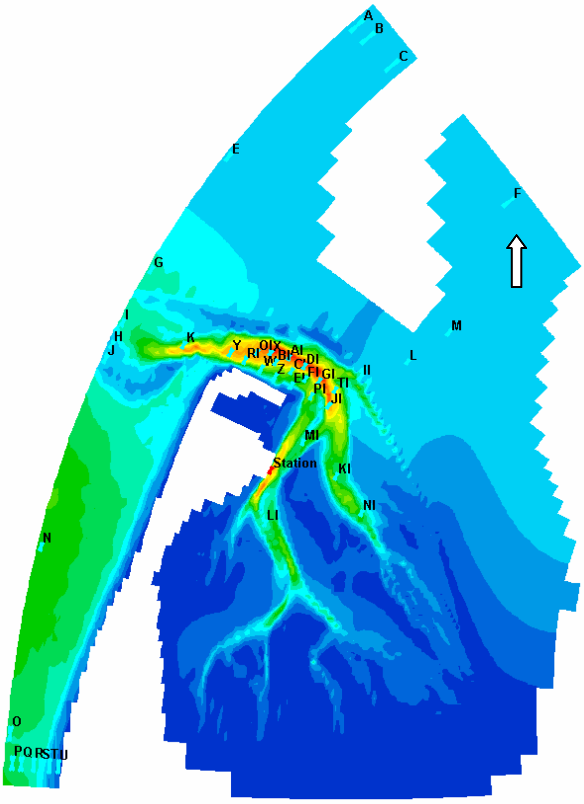

Figure 5-7. Observation points of the model domain.

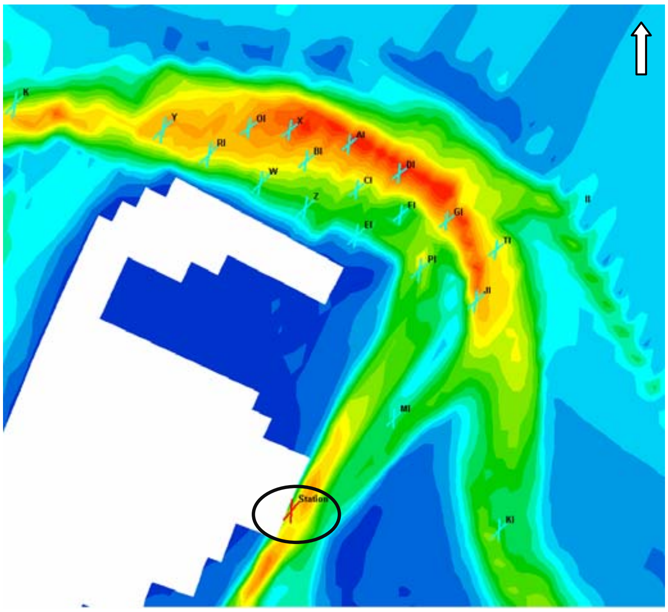

Figure 5-8. Observation points in the area of interest, with red cross the observation point "Station".

5.1.5 Nesting

The open boundary conditions for the flow model were obtained by nesting sequence of two-dimensional, depth-averaged current models. The nested models receive boundary values from the coarser model. The nested sequence consists of three model configurations (figure 5-9) [WILKENS et al. 2005]:

A) A coarse-resolution outer model, Continental Shelf Model (CSM) which was developed by Delft Hydraulics in the Netherlands. Astronomical components and wind were forced along the open boundaries.
B) A fine-resolution inner model covering the German Bight, named German Bight Model (GBM). At the open boundaries of the GBM water levels are obtained from the CSM.
C) And a very fine-resolution model for the Sylt Island.

Flow conditions along the open-sea boundaries of the investigation area were obtained by nesting the model of Sylt Island in the GBM, which in turn is nested in the north-west CSM.

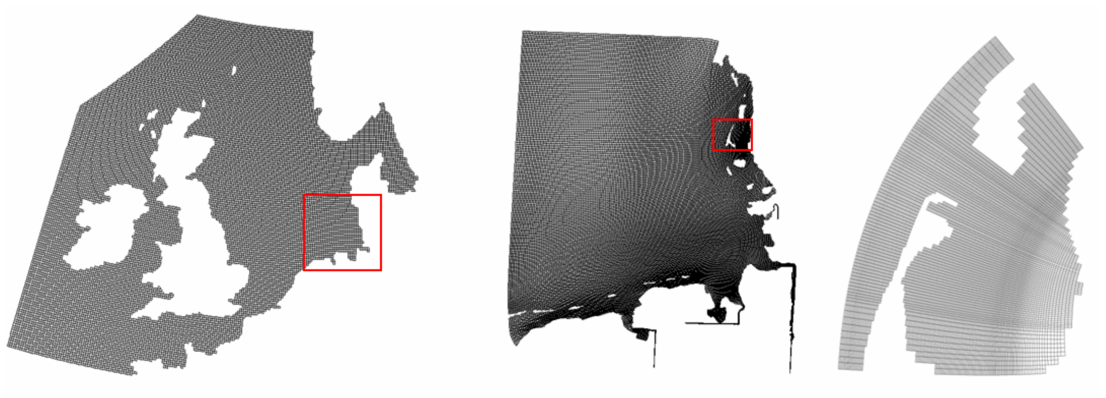

Figure 5-9. Model nesting (from left to right CSM, GBM, Sylt model).

5.1.6 Initial Conditions

The dynamic equations for momentum, temperature are Partial Differential Equations, and therefore need initial and boundary conditions in order to be solved. Initial conditions are required for dependant variables used in the model set up, such as water level, flow velocity componets [DELFT 3D MANUAL]. The initial conditions are either from observations, idealised, or simply set to uniform for the entire area or taken from previous run.

At each start of a simulation the velocities and water level (in respect to the reference level) are set to zero. The physical parameters that were kept constant for all simulations are summarized in table 5-1.

Table 5-1. Constant Physical parameters for all models.

Parameter	Value
Acceleration due to gravity	9.81 m/s^2
Water density	1025 kg/m^3
Threshold depth	0.1 m
Smoothing time	60 min

6 Sensitivity analysis for the Numerical parameters

The sensitivity analysis of the input parameters is the guide to any further use of the model. Through the sensitivity studies the relationship between input quantities and output quantities of the model are investigated [DELFT 2007].

The analysis was made in terms of the influence of different input parameters on the water level. The effect of time step, grid spacing, and approaches adopted for prescribing open sea boundary conditions on water levels and currents at several locations was tested. As it is mentioned in chapter 3, the water level and the wind measurements were available from the German authorities from the station in List Port. In the model the station is represented by the observation point named “Station”.

The time frame of the sensitivity simulations is set from the 22nd of May 00:00:00 up to 7th of June 00:00:00. This period was selected due to the availability of the in situ measurements, for the currents.

6.1 Effect of the Grid Resolution

Three curvilinear grids with element spacing ranging between 30 and 90 m (finer grid), 60 and 180 m (reference grid) and 120 and 360 m (coarser grid) were tested. The grids were adjusted to bathymetrical samples of 1994 (described in section 5.2).

The reference grid was one time refined general and then in partial in the area of study that high resolution was acquired (Finer grid). A second grid was created but this time the reference grid was de-refined (Coarser grid). Afterwards, the grid properties were checked for each grid separately in order to follow the recommendations of DELFT-3D. In order to avoid significant influences of the time step on the results during the grid comparison, a same time step was assumed for every grid, take into account the Courant criterion (<10). The criteria for the selection of the appropriate grid are the minimization of the volume difference between the grid and the actual bathymetry and the minimization of the computing time. The characteristics of the three grids are presented in table 6-1.

The volumetric differences in percentage of the grid were calculated by the following formula:

$$\Delta V = \frac{V_{f-}V_i}{V_f} \times 100\% \tag{10}$$

V_f = volume below the MSL of the finer grid

V_i = volume below the MSL of the examined grid

Table 6-1. Characteristics of the selected grids.

	Grid Resolution (m)	ΔV% of III	Time step	Courant Number	Computing time	Orthogonality
I (Reference Grid)	94–130	1.35	0,5 min	1.8	1h	0.00
II (Coarser Grid)	172–298	3.44	0,5min	0.47	15min	0.01
III (Finer Grid)	40–60	0	0,5 min	9.47	6h	0.00

Figure 6-1 shows the time series of the water level of the three simulations of the different grids and the water level measurements at the reference station. The grid [II] and the grid [I], have a good agreement with water level measurements. On the other hand, the grid [III] overestimates significantly the water level. By checking the volume of the grid [I] and the grid [II] in comparison with the finer, the volume of the reference does not have significant differences with the volume of the [III] grid. As it concerns the computing time, the simulations with the finer grid took approximately 6 hours to run and on the other hand the simulation with the reference grid took 1 hour. Therefore, the reference grid [I] has been selected as an optimum grid for this investigation, with grid resolution 90 m and 130 m.

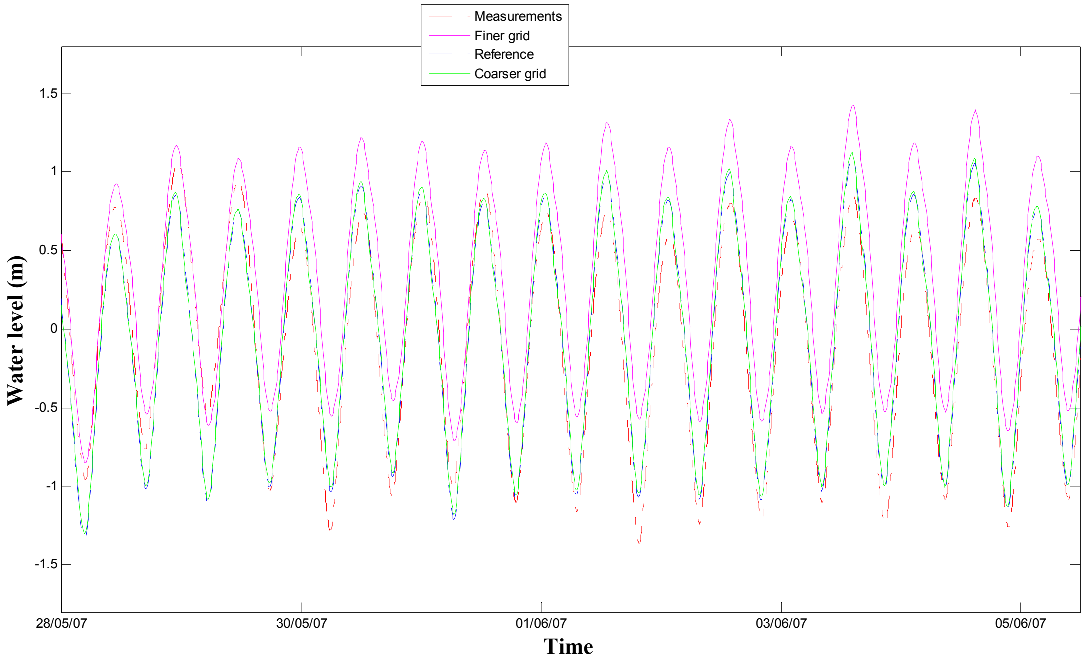

Figure 6-1. Water level time series at observation point “Station”.

6.2 Effect of Time step

In order to identify if the time step introduces any instability to the model, four simulations were run with different time steps. The recommended Courant number has to be less than 10; in table 6-2 the characteristics of the models with the different time step and the corresponding Courant numbers are summarized.

Table 6-2. Time step and Courant number for the sensitivity studies of the reference grid.

Model	Time Step (min)	Courant number
Model 1	0.1	0.6
Model 2	0.25	1.2
Model 3	0.5	1.8
Model 4	1	4

In figure 6-2, time series of the water level at the monitoring station in List Port (observation point named “Station”) with the time series of the models are presented. The differences between the computed water level time series of the four simulations with respect to the reference model (Model 4) were calculated and illustrated in figure 6-3. The differences between the four different time steps are insignificant with maximum value of the water level being equal to 0.0139 m, between the models 4 and 1. Due to the fact that the higher time step does not produce any instability, time step of 1 min was selected for the further simulations to save computing time.

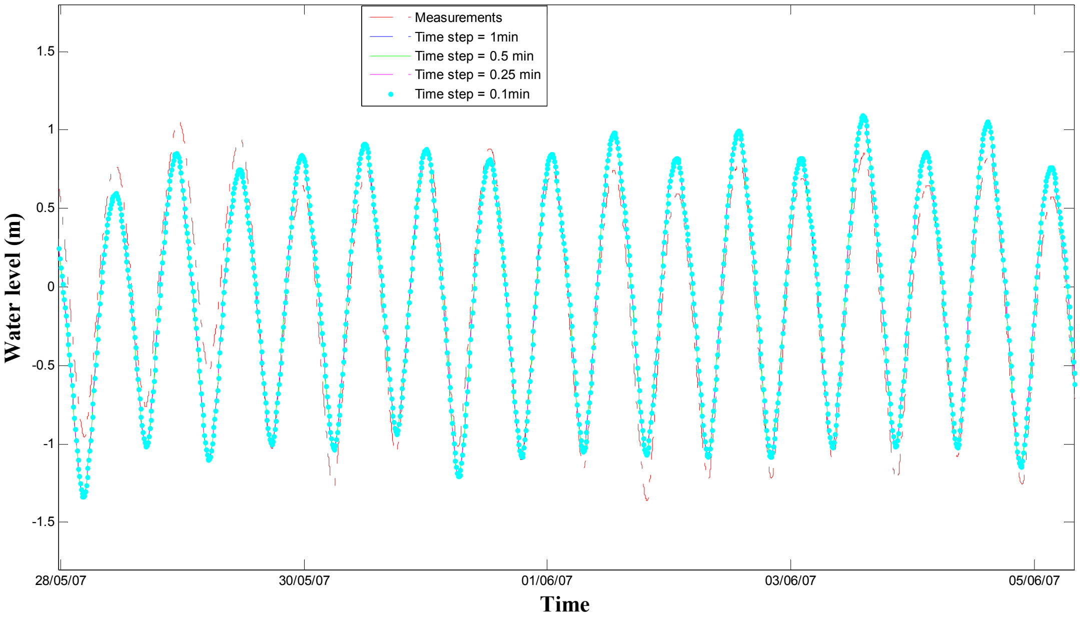

Figure 6-2. Comparison of the computed water level time series at the observation point “Station”, for different time steps.

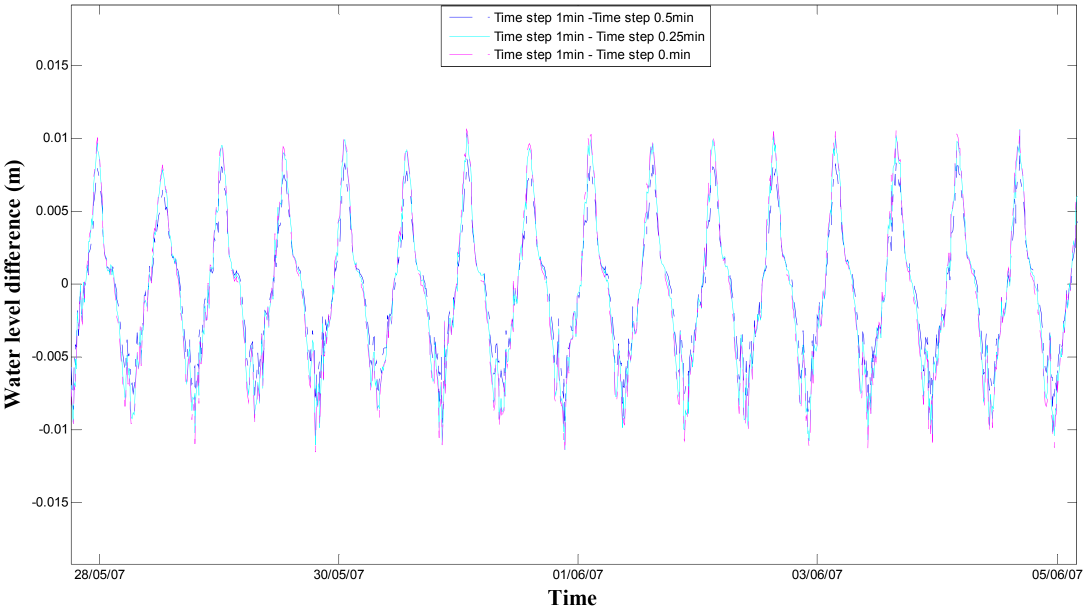

Figure 6-3. Water level differences between the model simulations.

6.3 Effect of the Open Boundary conditions

The model was set to run with open boundaries defined at the west (S1), at the north (S2, S4) and at the south (S3) of the model domain (figure 5-6). Water level and currents obtained from the nesting in the GBM, were forced along the open boundaries, due to the fact that there were no measurements available near the open sea boundaries; afterwards four different cases were selected for the investigation of the open boundaries effect. All the simulations of the cases were carried out with the default values (from DELFT 3D) of the physical parameters, with the reference grid [I] and with a time step of 1 min.

6.3.1 Case 1of the Open boundary

Case 1 investigates the effect of the water level (Model 1, figure 6-4a) and the currents (Model 2, figure 6-4b) imposed to all the segments of the open boundaries.

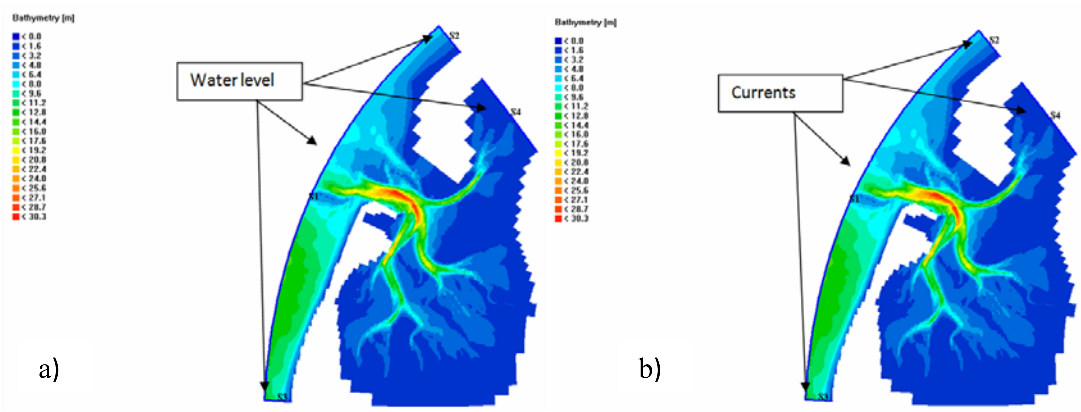

Figure 6-4. Case 1 for the sensitivity analysis of the open boundaries a) water level imposed b) currents imposed.

Figure 6-5 indicates the results of the water level series for case 1 at the monitoring point “Station”. Obviously the time series of the model with the imposed currents does not follow the tendency of the measurements, especially after the 30rd of May. On the other hand, the simulation with the water level, has a good agreement with the measurements from the station with the highest difference in the amplitude of the range 0.5 m.

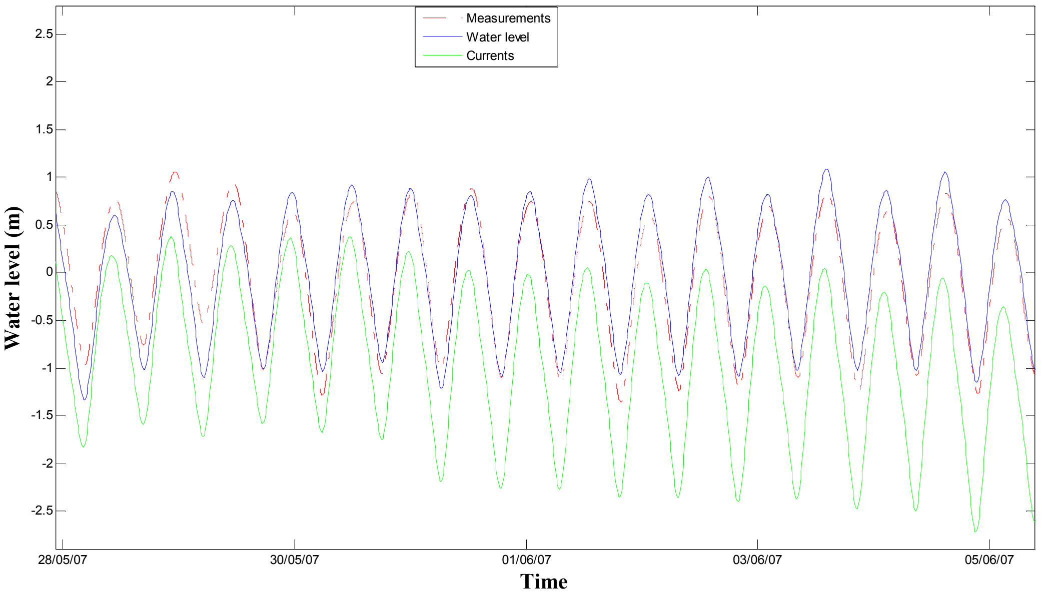

Figure 6-5. Water level time series of Case 1, at the observation point “Station”.

6.3.2 Case 2 of the Open boundary

In case 2, the segments S2 and S3 were considered as close boundaries (Model 3, figure 6-6a). Moreover, a simulation only with the segment S1 set as open boundary was run (Model 4, figure 6-6b). In case 2 only water level was imposed along the open boundaries.

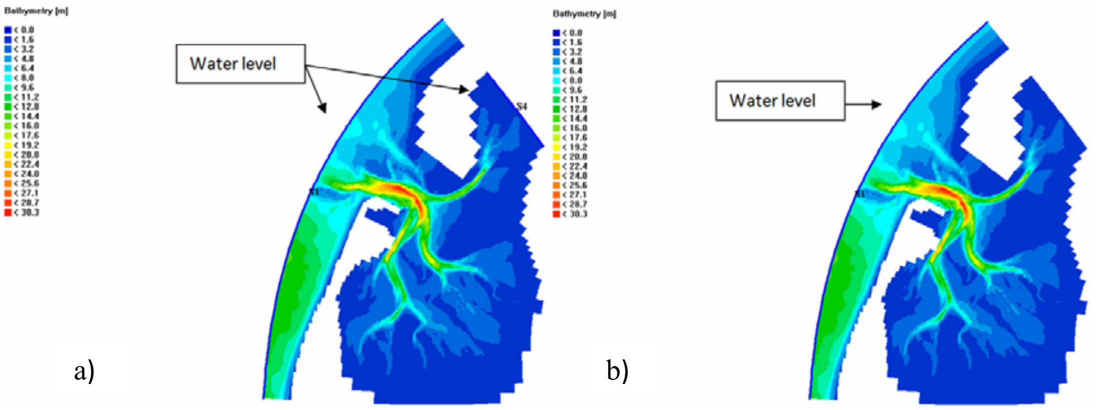

Figure 6-6. Case 2 for the sensitivity analysis of the open boundaries
a) water level imposed at S1 and S4 b) only S1 as open boundary.

The water level series obtained from the models of the case 2 are presented in figure 6-7. Comparing the resulted water level time series from the two models with the measurement at the observation point “Station”, they are insignificant differences between the two models of case 2. This was expected as the flow pattern at the segments S1 and S2 is insignificant.

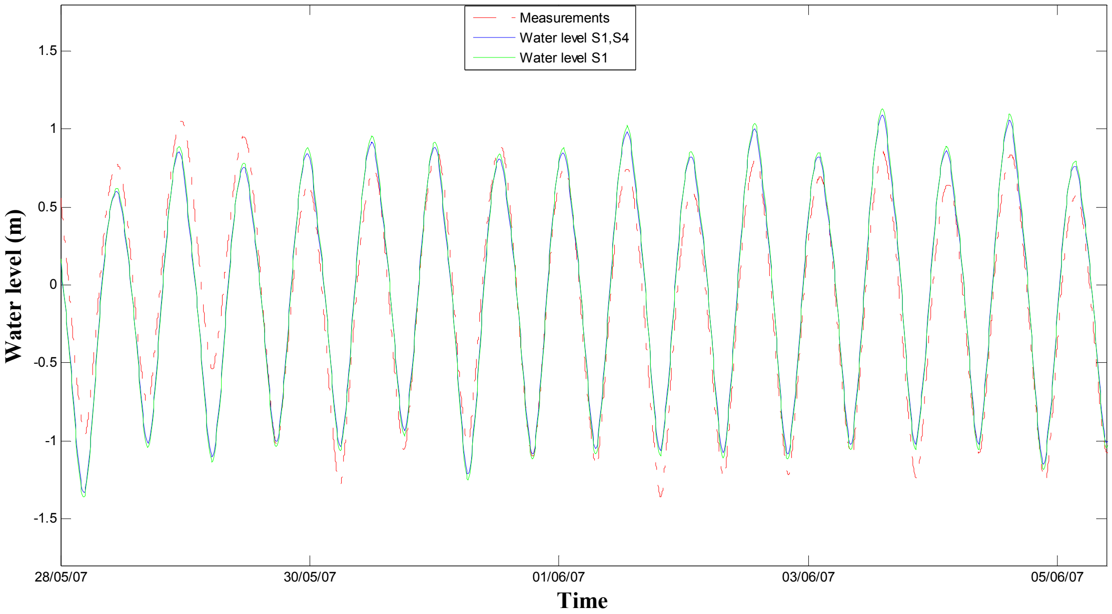

Figure 6-7. Water level times series of the models for the case 2 at the observation point "Station".

6.3.3 Case 3 of the open boundary

In case 3, water level (Model 5, figure 6-8a) and currents (Model 6, figure 6-8b) were imposed only to the segments S1 and S4.

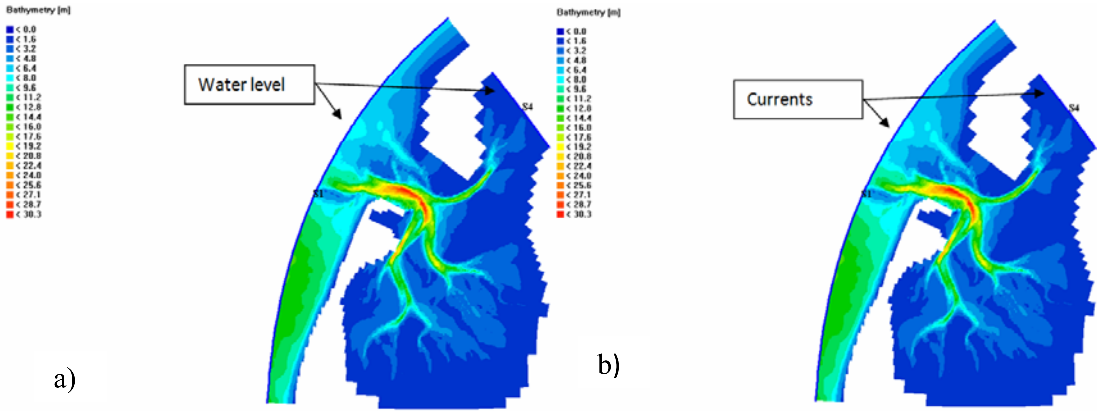

Figure 6-8. Case 3 for the sensitivity analysis of the open boundaries a) water level imposed at S1 and S4 b) currents imposed at S1 and S4.

In comparison with the simulation ran with currents imposed along all the segments in case 2, the simulation in case 3 in which currents were imposed only to the segments

S1 and S4 follows in a better way the measurements. Furthermore, in the present case the simulation that water level was imposed to the open boundaries, shows better agreement than the simulations with the currents. The difference of the amplitude between the measurements and the computed water level from the two models of case 3, is of the range 0.5 m, figure 6-9.

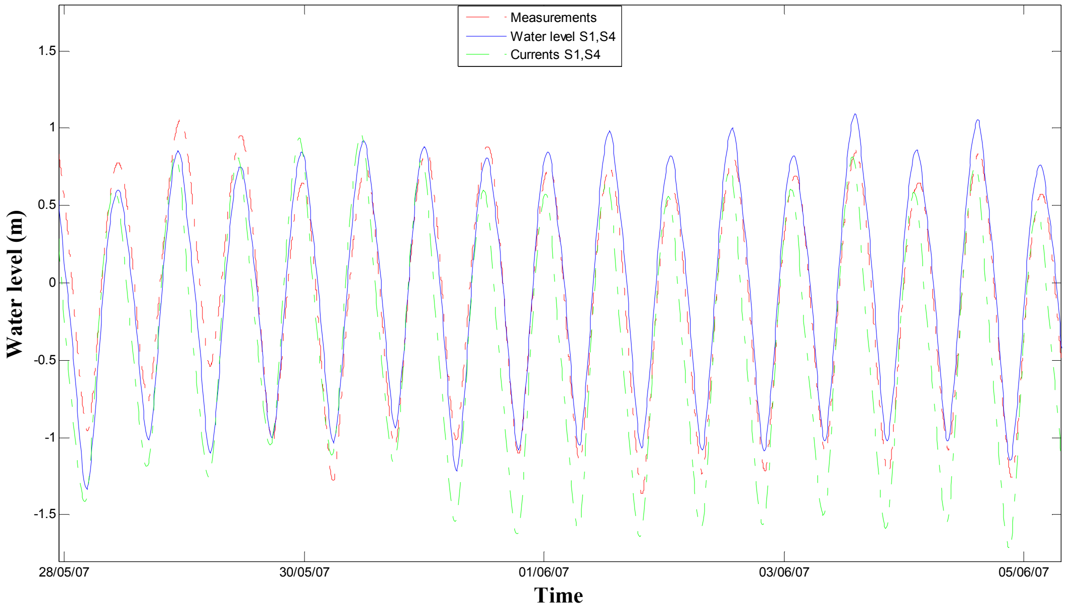

Figure 6-9. Water level times series of the models for the case 3 at the observation point “Station”.

6.3.4 Case 4 of the open boundary

Case four is the last case for the sensitivity studies of the open sea boundary in the present study. A combination of water level and currents imposed to the segments S1 and S4 was established. The first model was run with water level imposed on S4 and currents imposed on S1 (Model 7, figure 6-10a). The second model currents were imposed at the segment S4 and water level at S1 (Model 8, figure 6-10b).

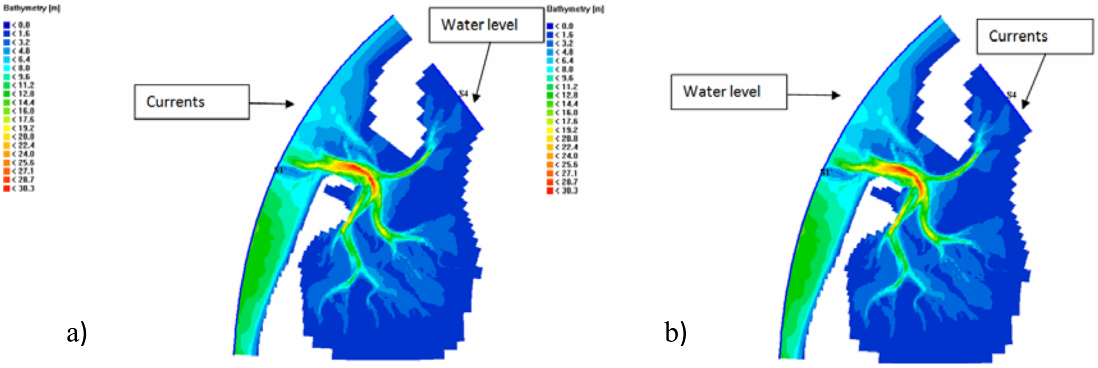

Figure 6-10. Case 4 for the sensitivity analysis of the open boundaries
a) currents imposed at S1 and water level at S4 b) currents imposed at S4 and water level at S1.

Model 8, as it can be observed from the figure 6-11 shows a better agreement with the measurements than the model 7. The difference in the amplitude of the two models is approximately 0.15 m.

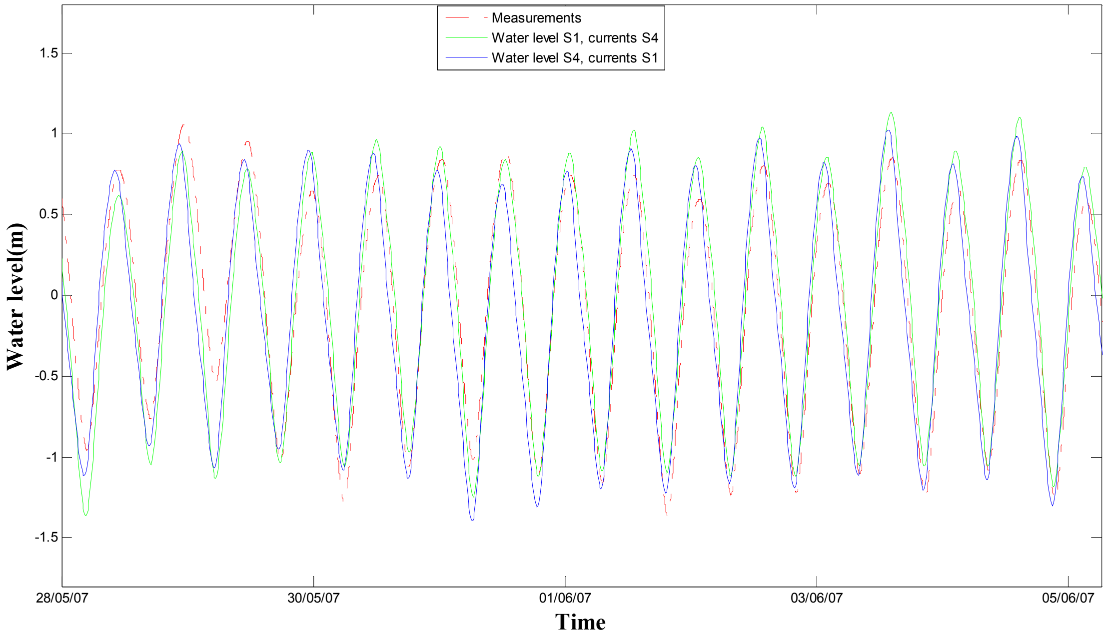

Figure 6-11. Water level times series of the models for the case 4
at the observation point “Station”.

On the basis of the analysis of the effect of the open boundaries on the model, and after the creation of different cases, the simulation that water level was imposed to segment S1 and currents to S4 (figure 6-10b) from the case 4 was selected for the further simulations. The results from this simulation had the smallest difference in the amplitude, compared with the measurements.

7 Calibration of the Physical parameters

The calibration is the stage that the model inputs are tuned in order to achieve the best agreement possible between the measurements and the model. In addition, the model calibration should include comparisons between model-simulated conditions and field conditions for the physical parameters. During the calibration is attempting to minimize the difference between model simulations and field measurements [SUTHERLAND et al. 2004]. Adopting the results from the sensitivity studies, the model calibration was carried out using the water levels recorded at the tidal gauge in Lister Port The same period that was used for the sensitivity analysis, 22nd of May until the 5th June 2007, will be used for the calibration.

7.1 Bed Shear Stress

The bed shear stress induced by a turbulent flow, for the 2DH flow model, is given by a quadratic friction formula [DELFT 2007]:

$$\vec{\tau}_b = \frac{\rho_0 g \vec{U} \left| \vec{U} \right|}{C_{2D}^2} \tag{10}$$

Where:

$\vec{\tau}_b$ = the bed shear stress vector

ρ_0 = the water density (kg/m^3)

g = the acceleration due to gravity (m/s^2)

$\vec{U}$ = the vector of the horizontal velocity (m/s)

C_{2D} = the 2D Chezy coefficient (m$^{1/2}$/s)

According to Delft-3D the 2D Chezy coefficient can be calculated according to three formulas

- The Chezy formulations :

  C_{2D} = the 2D Chezy coefficient (m$^{1/2}$/s) (11)

- Manning’s formulation

  $$C_{2D} = \frac{\sqrt[6]{H}}{n} \tag{12}$$

  Where:

  H = the total water depth (m)

  n = the Manning’s coefficient

- White Colebrook's formulation

$$C_{2D} = 18\log\left(\frac{12H}{k_s}\right) \qquad (13)$$

Where:

H = the total water depth (m)

k_s = the Nikuradse roughness length

The bed shear stress was considered as uniform for the formulation of Chezy and Manning's in both directions U, V over the whole model domain. In the case of the White Colebrook's formulation the bed shear stress was defined as space varying. The equivalent geometrical roughness of Nikuradse k_s, was specified. The k_s was calculated by the formula

$$k_s = 2.5d_{50} \qquad (14)$$

where, d_{50} is the median bed size of the sediments.

The d_{50} values were obtained by a multi-beam echo sounder during the ship campaign of 2007 (section 3.3.3). A rough map of the k_s was created and imported in the model. Due to the fact that the d_{50} values were available only in the area of the investigation, the k_s map was created by interpolating the results of the formula 13, for the whole model domain. The k_s in the area of investigation is presented in figure 7-1.

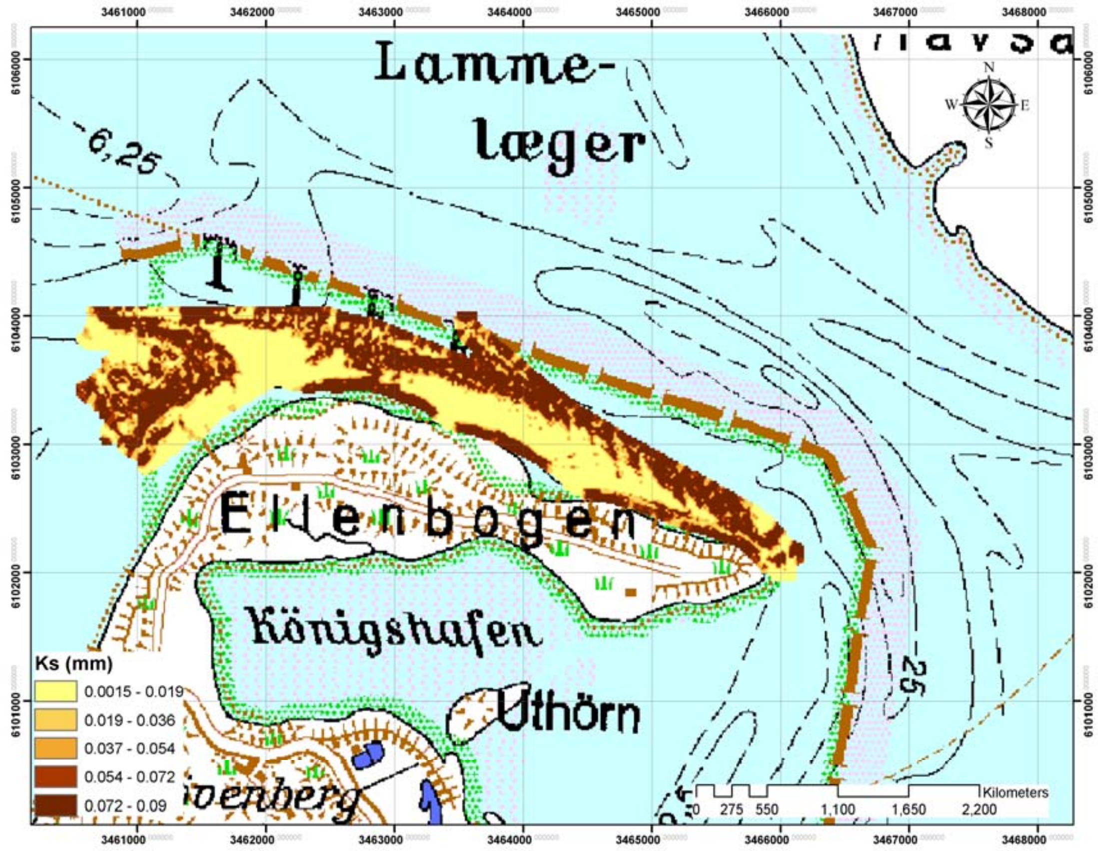

Figure 7-1. Ks map in the area of study.

Several simulations where carried out for defining the value which will give the closest result of the model with the measurements. Firstly, different values higher (75 $m^{1/2}/s$, 85 $m^{1/2}/s$, 95 $m^{1/2}/s$) and smaller than (35 $m^{1/2}/s$, 45 $m^{1/2}/s$, 55 $m^{1/2}/s$) the default value (65 $m^{1/2}/s$) of the Chezy coefficient were tested. The results showed no differences between them. Secondly, the Manning's coefficient was changed, with the same results as in Chezy. Finally, one simulation defining the 2D Chezy coefficient with the White Colebrook's formulation was set. In figure 7-2, three model are represented, each one with different formulation for the calculation of the bed shear stress. As it is observed from the results, the models with the Chezy and the Manning formulation have insignificant differences in the amplitude of the water level about 0.0715 m. The difference in the amplitude between the model with the White Colerbrook's formulation and the model with Chezy formulation is about 0.118 m. Comparing the computed water level time series from the three models and the measurements no significant discrepancies are observed. The results from the models do not show any phase lag with respect to the measurements. The only difference is in the amplitude which is about 0.65 m. As a consequence, the Manning's formulation was set for the further simulations. In table 5 the parameters used for these simulations are presented.

Table 7-1. Model's parameters for the bed roughness.

	Formula of Bed Roughness	**Value of Bed Roughness**
Model 1	White-Colebrook	Ks map
Model 2	Manning	0.02
Model 3	Chezy	65 ($m^{1/2}/s$)

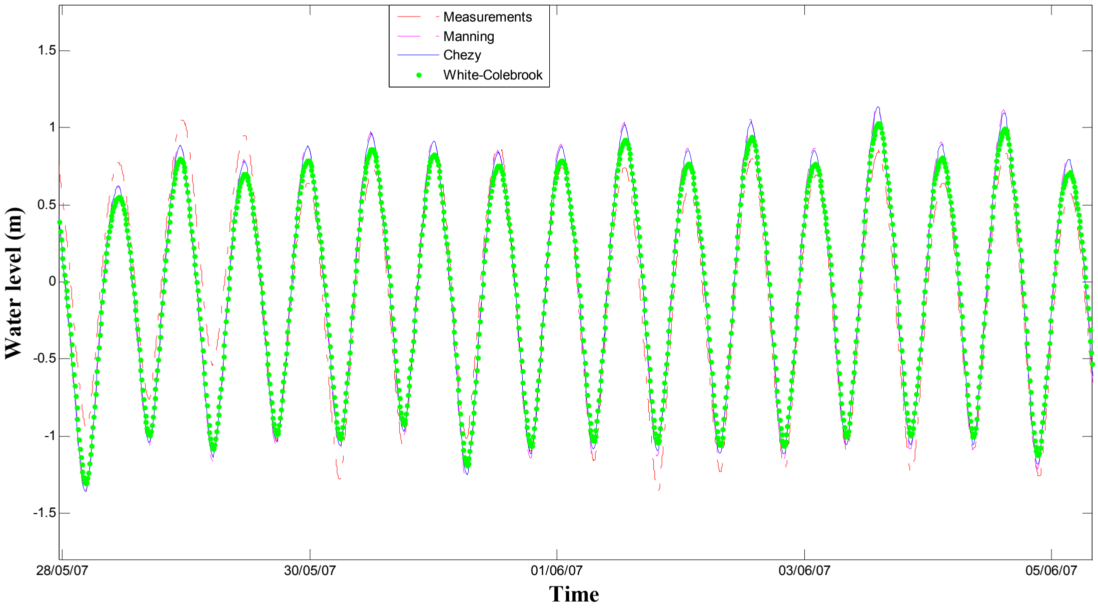

Figure 7-2. Water level time series of the Models with different formulas of the calculation of the Chezy coefficient, at the observation point "Station".

7.2 Eddy Viscosity

The next step was to investigate if with the change of the viscosity, better computed results will be obtained with respect to the measurements. The eddy viscosity is a property of the flow, not of the fluid. It varies in space and time but a constant value was used in the modeling. To analyze the effect of the eddy viscosity coefficient onto the model, three different values of 2 m^2/s, 0.002 m^2/s and 0.0002 m^2/s were applied. In figure 7-3, the computed water levels from the three simulations are plotted. As it is observed, the eddy viscosity has a negligible effect on the output water levels. Concluding, the eddy viscosity was set to a constant value of 0.002 m^2/s.

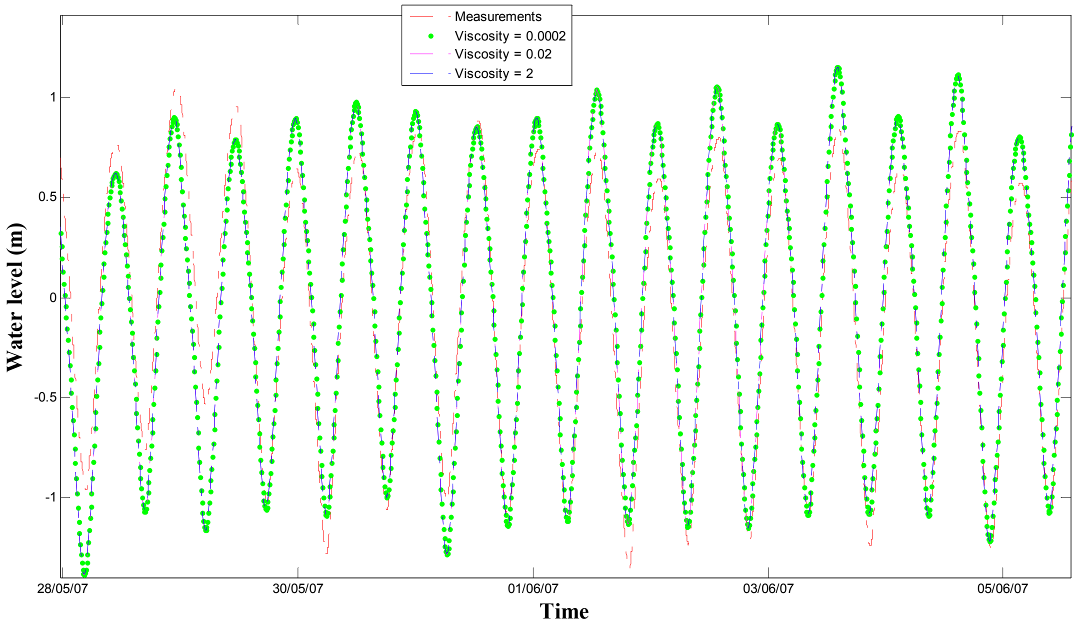

Figure 7-3. Computed water level time series of the investigation of the eddy viscosity.

7.3 Impact of the Bathymetry

The last physical parameter that was investigated was the bathymetry. The available bathymetric datasets were for the years 1994 and 2007. The computed results are from the tidal gauge in Lister Port. The computed water level time series for the two models, with the different bathymetries show discrepancies, figure 7-4. The model of 2007 compared with the measurement has a difference in the height amplitude approximately 0.5 m. On the other hand comparing the model of 1994 with the measurements from the gauge station the difference in the height amplitude is about 0.4 m.

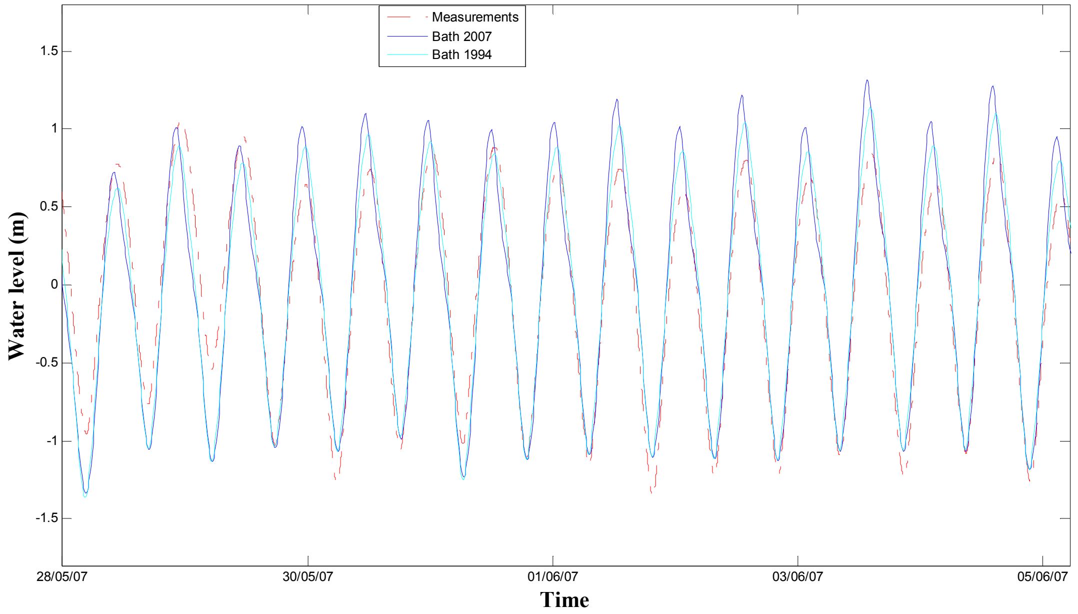

Figure 7-4. Water level time series of the models with the bathymetries of 1994 and 2007.

The model bathymetries of the years 1994 and 2007 were subtracted in order to investigate the changes of the depth in the area of investigation (figure 7-5). The maximum positive difference is observed in the channels Lister Dyb, Hoyer Dyb and Lister Lay that indicates accumulation of sediment. Moreover positive depth values can be found in the West part of the Sylt Island and near the coastline at the north part. In the area of study, Lister Tief channel, negative maximum values are observed of a range between -8 m and -19 m, which is an indication of sediment reduction. Therefore, the effect of the topography in the model is significant. Due to the fact that the ship campaign was carried out in 2007, the model with the bathymetry of 2007 will be taken into consideration for the validation of the numerical flow model.

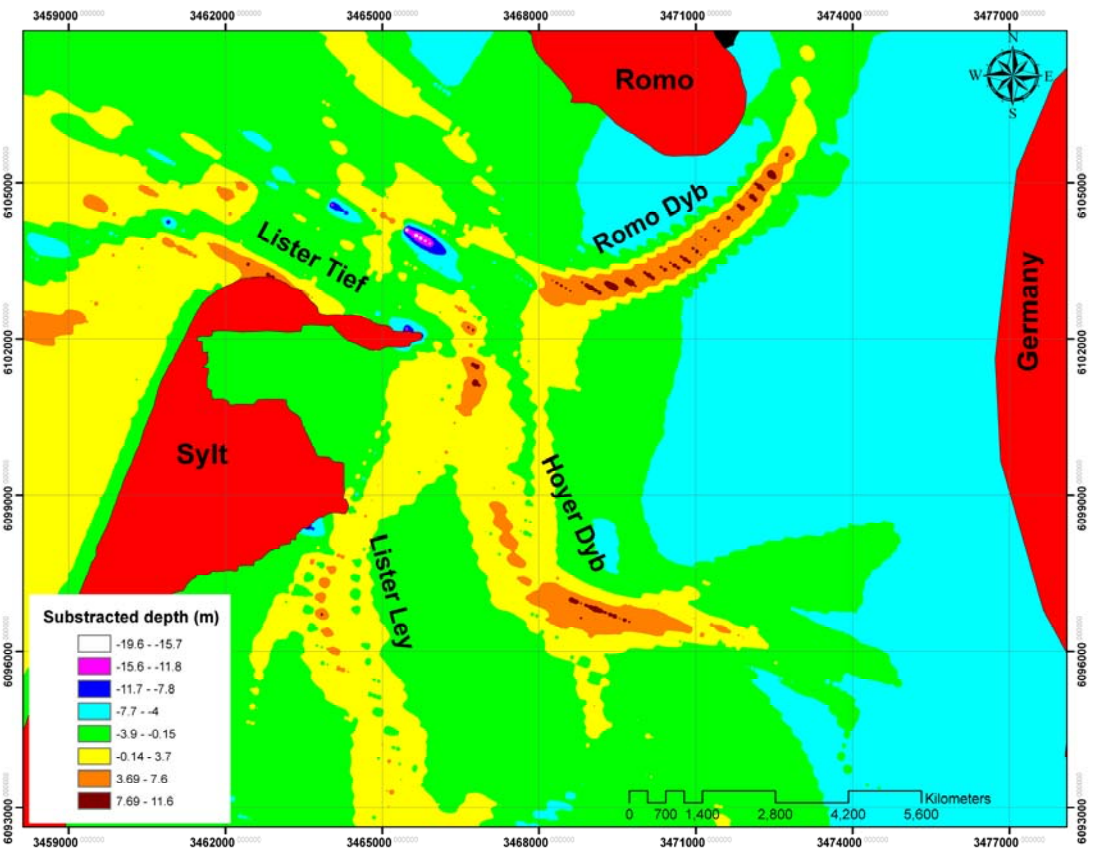

Figure 7-5. Result from the subtraction of the bathymetry of 2007 from the bathymetry of 1994.

7.4 Performance of the Model

The statistics below have been used to evaluate the performance of the numerical model. The statistical parameters used for checking the performance of the model were the Relative Mean Absolute Error (RMAE) and the Mean Absolute Error (MAE). These values may be scalars, wave height or water level, or vectors, currents. The statistical analysis was on the base of the water level at the observation point “Wind Station”. The measurements of the tide gauge station in Lister Port were taken into account.

The formula of RMAE and MAE are the following:

$$RMAE = \frac{\sum_{j=1}^{n} \left| Mod_j - Mea_j \right|}{\sum_{j=1}^{n} \left| Mea_j \right|} \qquad (14)$$

$$MAE = \frac{\sum_{j=1}^{n} \left| Mod_j - Mea_j \right|}{n} \quad (15)$$

Where:

$\sum_{j=1}^{n} Mod_j$ = sum of the computed values from the model

$\sum_{j=1}^{n} Mea_j$ = sum of the measurements

n = number of values

A classification table has been adopted, that categorizes the results according to RMAE. The quality of the model is classified from excellent to bad (table 7-2). The standards for the quality of the results from the model were proposed by [WALSTRA, 2001]. These standards are for current velocities computed from models in the North Sea coast. A RMAE value of zero implies a perfect match between predictions and observations. This will never, in practice, be achieved as the RMAE includes contributions from the measurement error [VAN RIJIN et al 2000].

Table 7-2. Classification of the model quality in a tidal inlet, [Walstra et al. 2001].

Qualification	**RMAE**
Excellent	<0.2
Good	0.2–0.3
Reasonable / Fair	0.4–0.7
Poor	0.7–1.0
Bad	>1.0

Two models are checked for their performance; the model with the bathymetry of 1994 and the model with the bathymetry of 2007. The quality of both models is characterized as Reasonable/Fair with a very small difference of the range 0.0025, table 7-3.

Therefore, for the spatial resolution of the order of 100 m applied here, and for the low wind conditions during the period of the study, the field of the geo-structure presented in the inlet, has impact on the overall performance of the model. The degrees of freedom have not been taken into consideration for the determination of the calculated accuracy. The standard deviation of the difference of the computed water level series of the bathymetry 1994 and bathymetry 2007 is 0.1162.

Table 7-3. RMAE and MAE for the models of 1994 and 2007.

	MAE	**RMAE**	**Quality of Model**
Model with the bathymetry of 1994	0.04510	0.6644	Reasonable / Fair
Model with the bathymetry of 2007	0.04493	0.6619	Reasonable / Fair

8 Results – Discussion

8.1 Surface observations

The visualization and the discussion of the results consist the final part of the study, following the methodology of the previous section, about the analysis of the spatial data. The dataset 296 from the RDCP was selected to be discussed. The magnitude of the surface current speed (color scale) overlaid by the DEM of the bathymetry (gray scale), are geo-gridded in a common mash with same spatial resolution (15 m), figure 8-1.

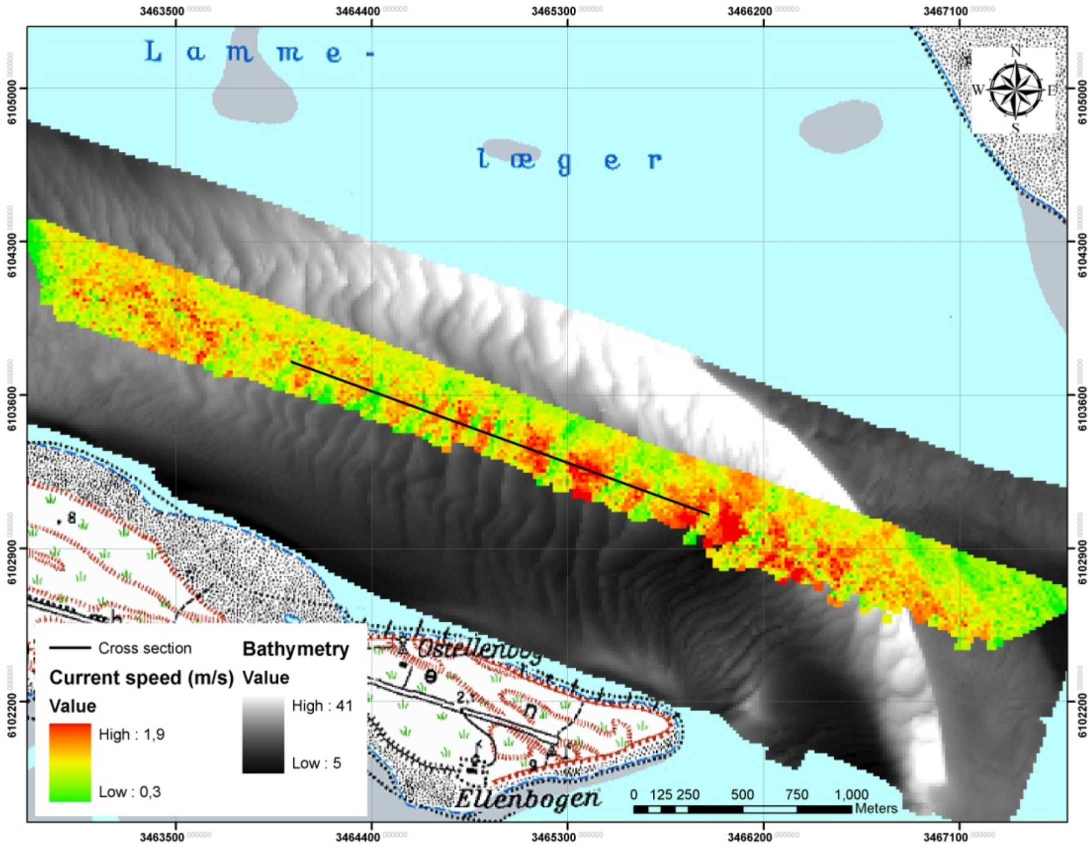

Figure 8-1. Cross section defined by the user, RDCP dataset 296, (source base map: TOP50 Schleswig Holstein and Hamburg).

The variation of the large sand geo-structures causes alterations to the surface current field. The first derivative of the vector velocity in x and y direction with respect to the North and the East were calculated and added in the same mash grid with the bathymetry, figures 8-2, 8-3.

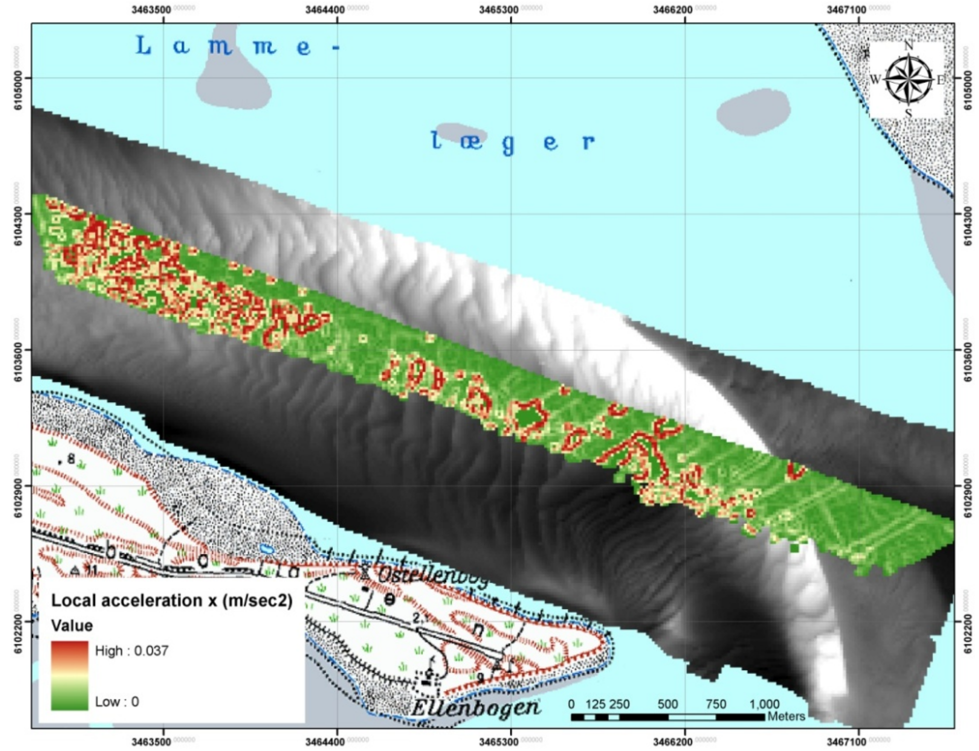

Figure 8-2. Local acceleration (m/s^2) in x-axes over layered to the bathymetry in the area of investigation, (source base map: TOP50 Schleswig Holstein and Hamburg).

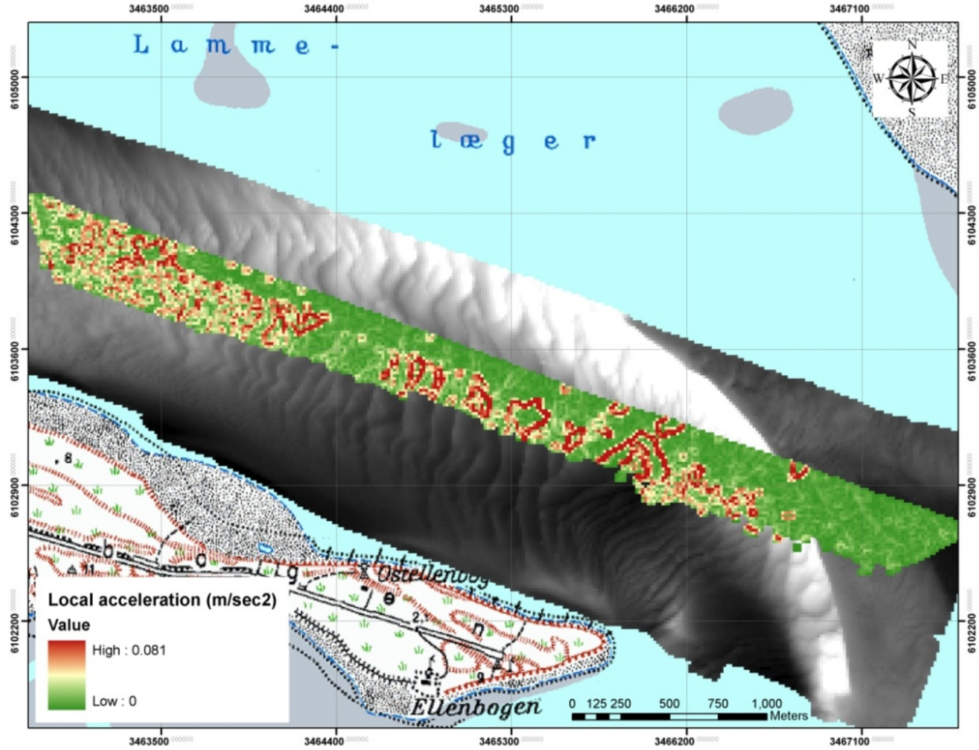

Figure 8-3. Local acceleration (m/s^2) in y-axes over layered to the bathymetry in the area of investigation, (source base map: TOP50 Schleswig Holstein and Hamburg).

The strips in figures 8-2 – 8-3 at the east end of the cross section result from a wrong estimation of the valid velocity caused by the rolling of the ship.

Even though, the RDCP dataset 296 was obtained one hour before high water, it shows signatures on the sea surface, which are related to the geo-structures of the seabed. Those irregularities were observed by the radar above the steepest regions of the subaqueous dunes, figure 8-4. The observations indicate extensive water turbulence parallel to the crests of the sand dunes. The indentified inhomogeneties of the current field with regard to the direction of the current at the water surface appeared downstream of the crests. The sea surface accelerates before the crests and decelerates over the trough of the sand dunes. In the area of investigation the length of the sand waves from crest to crest varies from 100 up to 300 m or more, and their height up to 11 m [OROMA, 2004].

The values of the surface current velocity over the sand dunes range between 1 m/s and 1.8 m/s. A small shift maybe is due to the fact that the bathymetric samples from the echo sounder were not obtained the same time as the RDCP dataset (31.05.2007–02.06.2007)

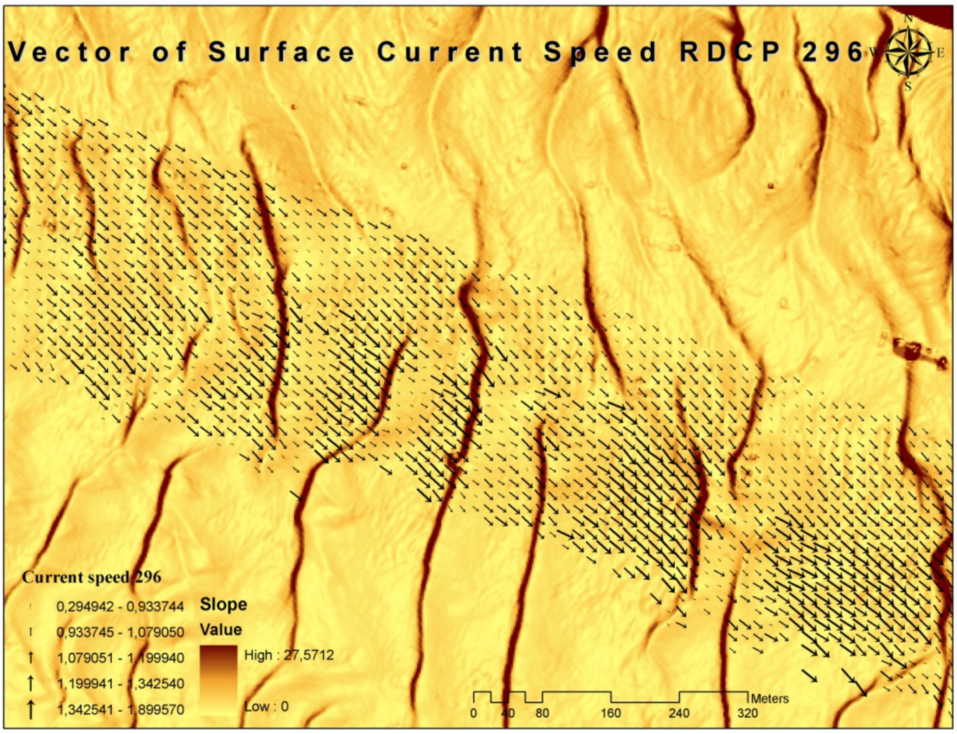

Figure 8-4. Surface current speed over layered the slope (degrees) of the bed relief in the area of investigation.

For the deepest investigation of the velocity fluctuations according to the bathymetry, a user defined cross section in the area of study, was selected to focus on. Vertical profiles of the absolute depth, the slope of the bed relief, the surface current speed, the localization of the acceleration were taken along the length, of the referred cross section 2.000 m (figure 8-5). The highest value of the depth in that specific area is 24 m and the slope of the sand dunes exceed the 10^0. The peak values of the acceleration are observed above the steepest slopes; this phenomenon is not observable at the depths greater than 17 m. The red lines in figure 48 indicate points of high values of the surface velocity and the corresponding values of the depth, slope, and acceleration.

At the point 800 m, the surface current magnitude is 1.38 m/sec and the velocity direction, 130^0, over a sand dune with a slope approximately 3^o at the depth of 17 m. The corresponding values of $\partial Ux/\partial x$ and $\partial Uy/\partial y$ are of the range 0.05 and 0.02 m/s^2 respectively. This mechanism is expected from the continuity law of the water mass, contrary to that in some areas the law is not valid, as it is examined over the cross section; fact that proves the complexity of the tidal inlet system and the necessity for a three dimensional observations of the hydrodynamics. An example of that is observed at the end of the cross section, where high values of the current velocity occurred at a water depth of 24 m.

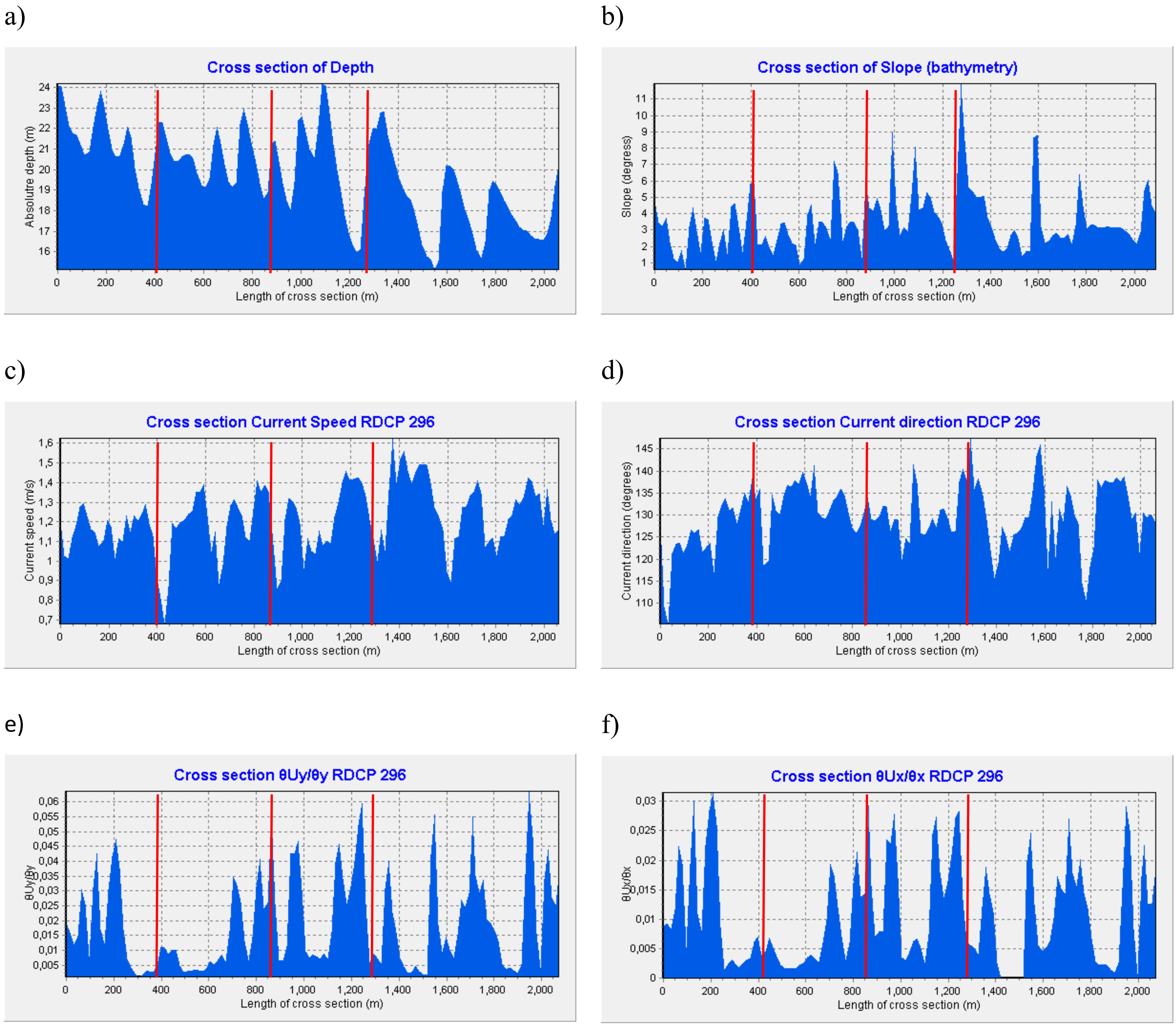

Figure 8-5. Vertical profiles of the user defined cross section.

The correlation of the surface current speed as a function of the depth was investigated (figure 8-6). The surface current speed was averaged according to the depth (every one meter). For the identification of the trend, four different approximations were tested, the linear based on the continuity mass law, that in shallow waters the velocity is higher than in deeper waters. The 3rd order polynomial was tested, due to the fact that in figure 51, were observed three different situations. At depths between 15 m and 17 m the velocity is constant; from 18 up to 21 m the velocity a variation over from 22 m becomes constant again. Finally, the second and the logarithmic approach were tested. The four equations and the square residual, for all regression types are summarized in table 8-1.

The R^2 of all four models proves strong correlation between the bathymetry and the current speed. The 3rd order polynomial indicates that the velocity less than 17 m is not increased over 1.4 m/s and over 21 m depth is not decreased more than 1.1 m/s. This fact proves that there are low and high conditions of stability of the current field.

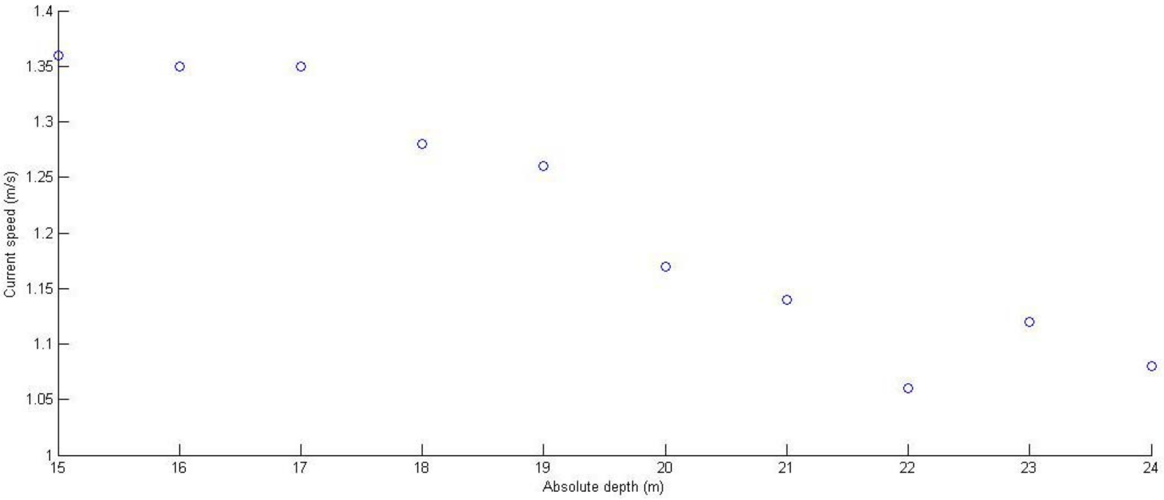

Figure 8-6. Current speed versus absolute depth.

Table 8-1. Information about the tested trend lines.

Trend Type	**Equation**	**R^2**
Linear	$y = -0.0369x + 1.9367$	0.9166
Logarithmic	$y = -0.709\ln(x) + 3.3142$	0.9163
2nd order Polynomial	$y = 0.0007x^2 - 0.065x + 2.2045$	0.9189
3rd order polynomial	$y = 0.0014x^3 - 0.0792x^2 + 1.4728x - 7.531$	0.9658

8.2 Vertical profile Observations

The next step is the verification of the impact of the bathymetry on the current field by evaluating the water column data from the ADCP. The analysis is based on the cross section, dataset 296 (figure 8-7), one hour before high water, obtained on the 31st of May 2007, (13:48–14:14). The orientation of the cross section is from West to East and it is followed in all figures of the section.

The vertical mean magnitude and direction of the water column were calculated over depth for the ensembles of the ADCP cross section (acquired at 5.320 m) and correlated with the depth, figure 8-8, 8-9. The red lines perpendicular to x-axes, indicates the starting and ending point of the user's defined cross section, from the section 8.1, figure 43.

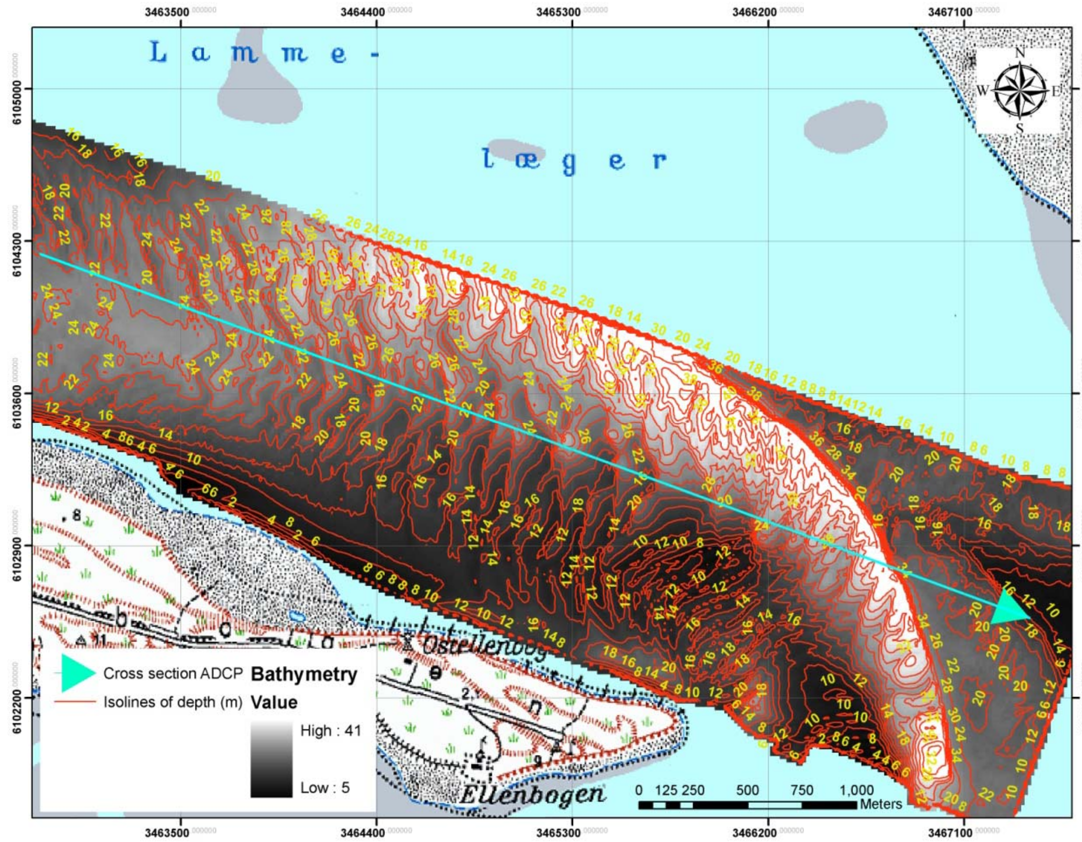

Figure 8-7. The sea way of the cross section 296 from the ADCP over layered to the bathymetry and the isobaths, (source base map: TOP50 Schleswig Holstein and Hamburg).

The vertical profile has the same behavior in the area where the user's defined cross section is located, concerning the high variation of the velocity. The maximum and the minimum values of the mean velocity are 1 m/s and 0.5 m/s. On the other hand, the mean direction of the vertical velocity fluctuates between 110^0 and 140^0.

Noticeable is the change of the mean velocity after the crossing of the ship over the channel (deepest part of the area), between the points 3.000 m and 4.000 m, which it seems to be inverse proportional to the depth and don't follow the continuity law, here the cross section widen in the horizontal direction. Simultaneously with the mean velocity, the mean direction from a constant phase starts to increase up to a point that reaches the highest peak during the whole profile.

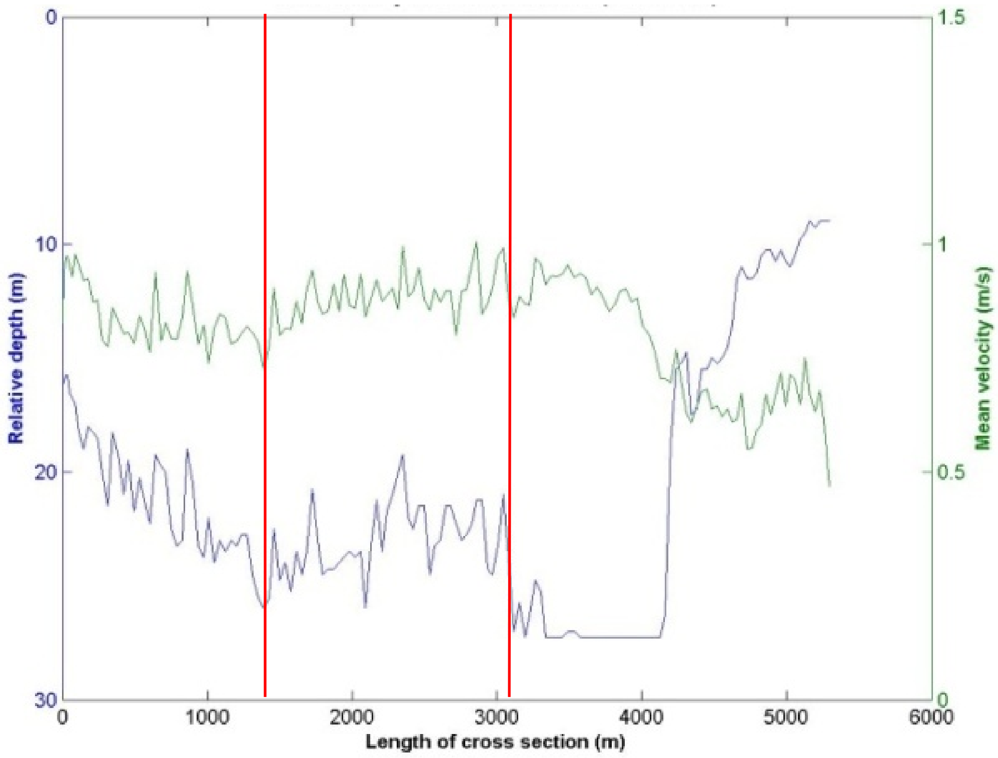

Figure 8-8. Mean velocity of the water column of the ADCP cross section 296.

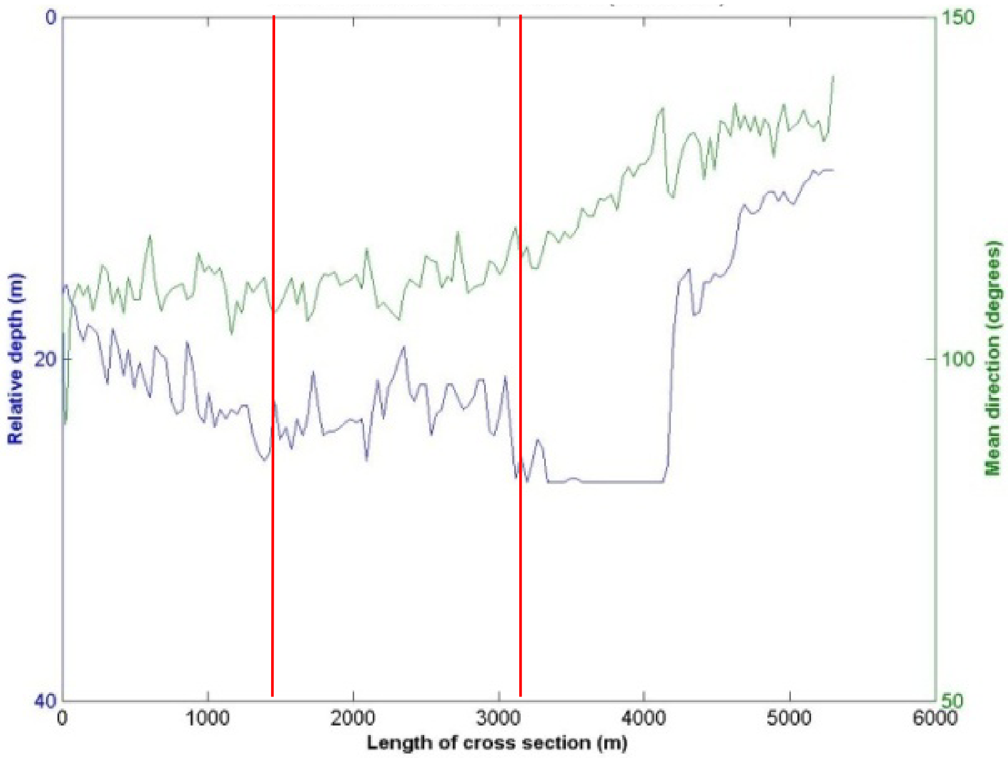

Figure 8-9. Mean direction of the water column of the ADCP cross section 296.

From the ensembles of the ADCP measurements, the average velocity and direction over space and time was calculated. The integration time is every 10 sec and the depth's integration is every 1m, figure 8-10, 8-11. As in the previous figures the same variations are observed. The highest values of velocity, 1m/s and 1.2m/s, are observed at depths from 5 up to 13 m, at the start of the cross section and between the points 2.500 and 3.700 m of the cross section. Near the sea surface and sea bottom these fluctuations of the current are not so strong. This phenomenon can be explained that the impact from the boundaries layers is constant and significant to the water column.

The occurrence of the low velocity at shallow water is remarkable once more, theoretically it should have accelerated. This is due to the channelization effect. The channel direction reference to the north is approximately 140^o. As it was mentioned previously, the vertical velocity direction has insignificant fluctuations. The change of the velocity direction ranges between 135^o–140^o in the water column, is observed after the crossing of the channel.

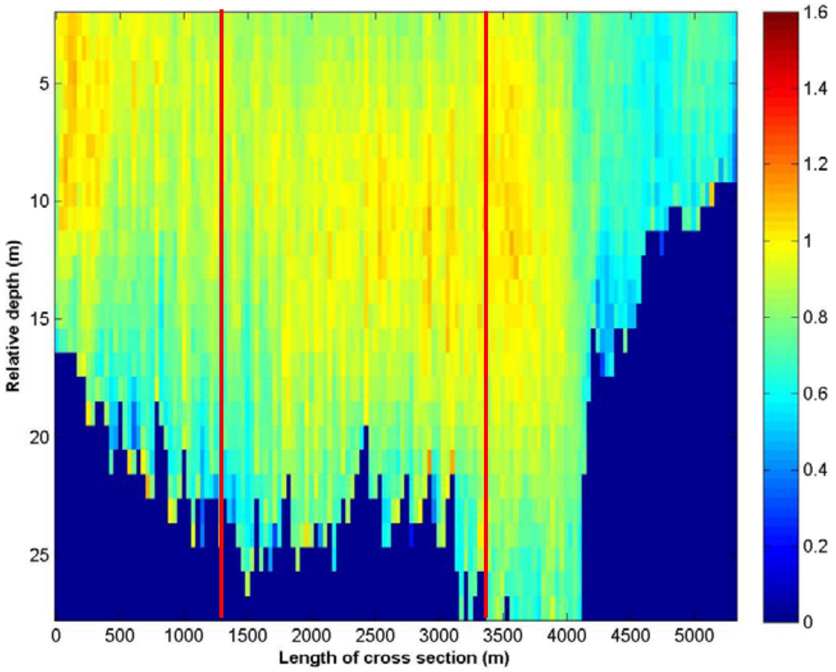

Figure 8-10. Averaged velocity magnitude (m/s) over 10 s and 1 m, ADCP cross section of dataset 296.

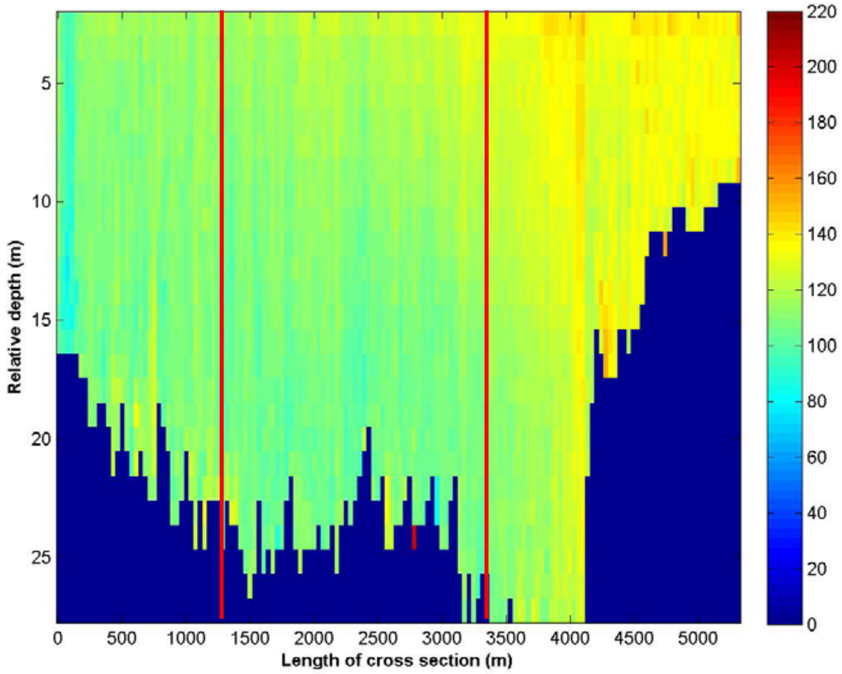

Figure 8-11. Averaged velocity direction (degrees) over 10 s and 1 m, ADCP cross section of dataset 296.

As the thesis focus on the fluctuations of the sea surface current field observed over the geo-structures, a characteristic example of one sand dune is selected for deeper investigation of the phenomenon. In figure 8-12 the blue circle defines the location of the sand dune. Starting from the trough of the sand dune and for every 30 m the vertical profiles of the depth average velocity were calculated and presented in figure 8-13. The vertical profiles show an increase of the value of the velocity in the middle of the water column and a decrease near the surface and the bottom, similar to the general mechanism described in the previous paragraphs. The velocity in the whole water column diversifies highly. (Each plot presents ensembles approximately every 30 m along a sand dune with length approximately 180 m).

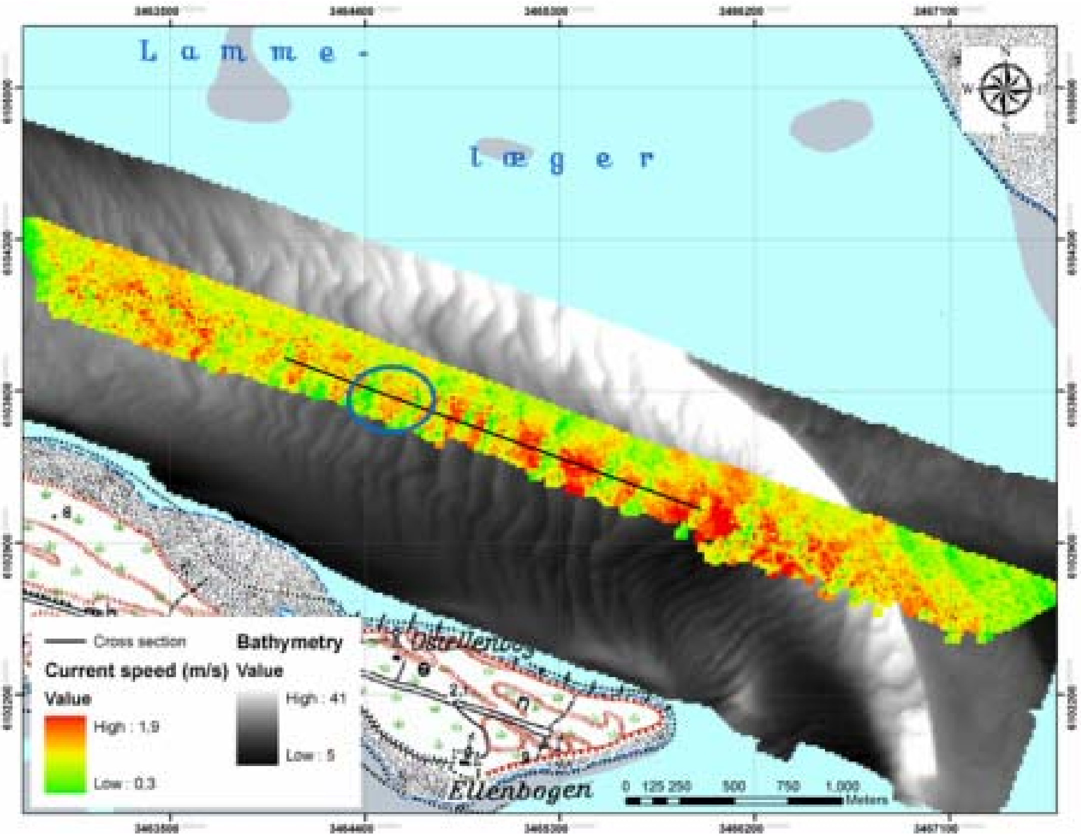

Figure 8-12. Map of the location of the investigated bottom structure, (source base map: TOP50 Schleswig Holstein and Hamburg).

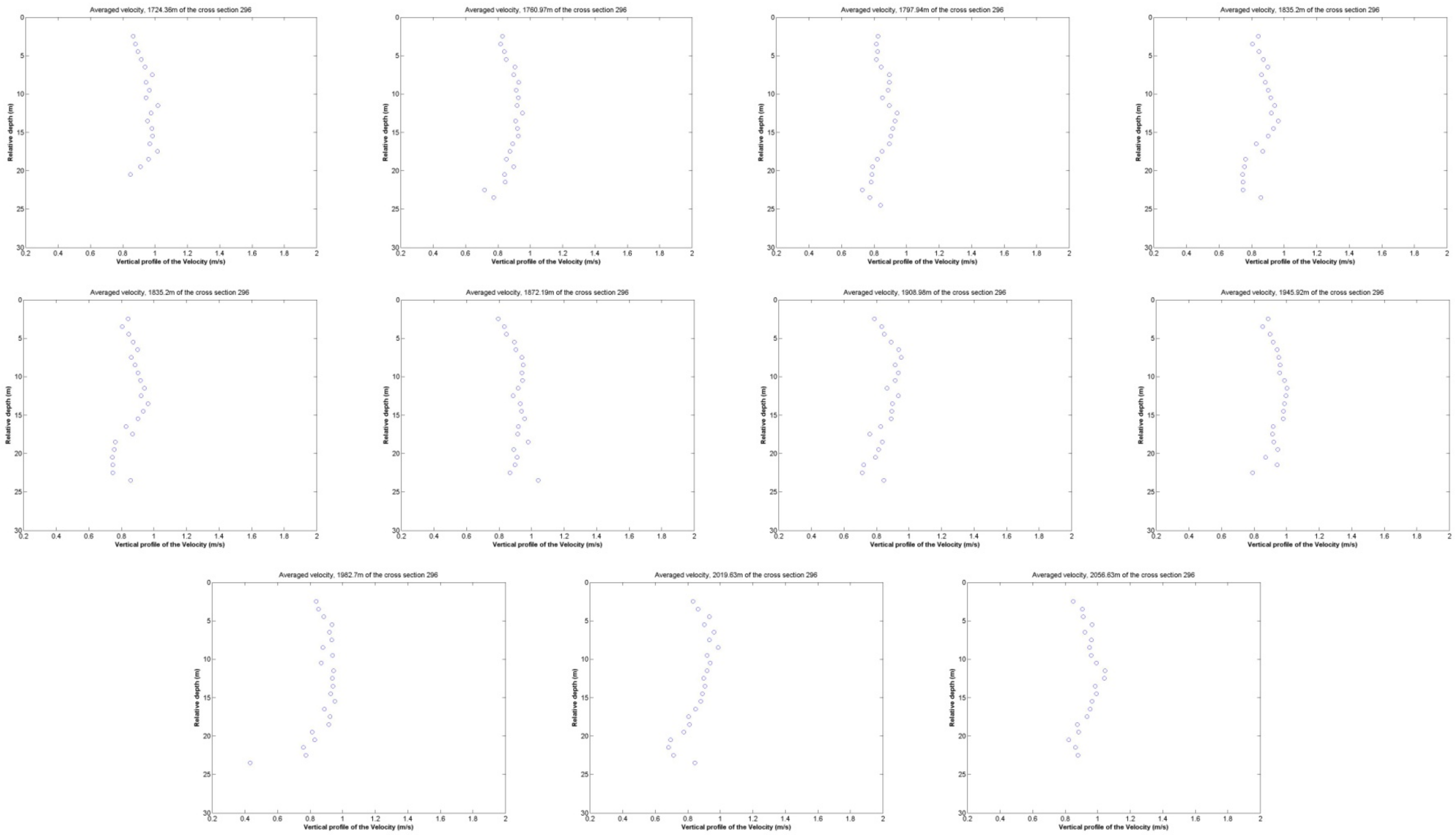

Figure 8-13. Vertical profiles of velocity over a sand dune every 30 m (starting upper- left up and finishing lower right).

8.3 Comparison of the 2DH Hydrodynamic Model with field Observations

The validation of the model was implemented in terms of the current velocity. The origin of the data measurements for the validation is from the RDCP. Due to the fact that time series from the observation data were not available, the comparison between the model and the observation data was made by checking the areas of the model with that the RDCP measurements cover. This is from the few model validations following this methodology.

The selected dataset for the validation is the 392 measured on 5th of June at 13:24–13:58. The geographical location of the areas of the model and the measurements are illustrated in figure 8-14. According to the tide calendar (BSH 2007) at the Lister Port the high water is at 06.19am and 18.28, the low water at 11.57.

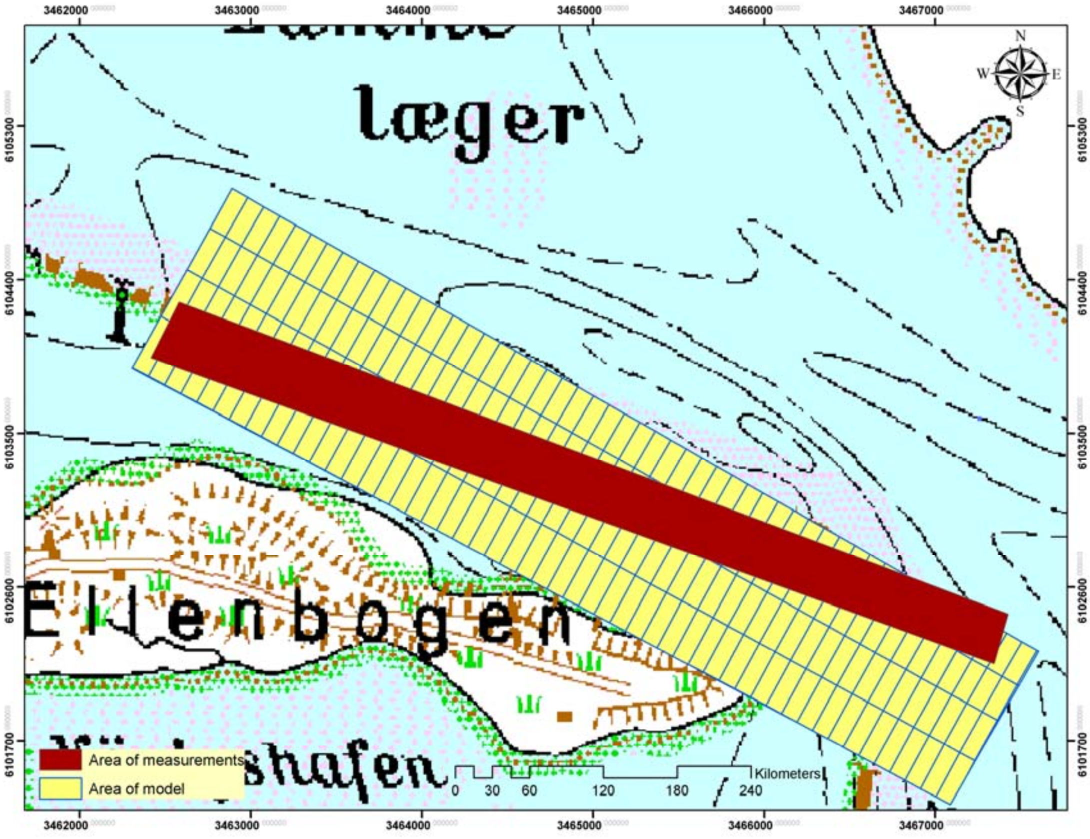

Figure 8-14. Polygons with the limits of the areas covered by the measurements and the model, (source base map: TOP50 Schleswig Holstein and Hamburg).

As the measurements last approximately 30 min, it is impossible to have exactly simulations model results, due to the fact that the output data storage is every 10 min. Therefore, time series of the computed depth averaged velocity vector field are utilized for the comparison of the measurements.

In order to be precise with the validation and to capture the alterations of the velocity, the depth averaged velocity was displayed before, during and after the surveying starting time, from 13:20 until 14:10 every ten minutes, figures 8-16 – 8-21. Between 13:20–13:40 the computed depth averaged velocity, in the area of interest, ranges between 1.2 m/s and 1.7 m/s, which are the highest computed values. After 14:10, the velocity is decreased and reaches the value of 0.9 m/s due to the fact that the slack water will follow. The highest values of the computed velocity existed in the channel of Lister Tief during the entire period of the simulations. Even though the significant difference of the measurement and model grid size, it is remarkable that the model simulates reasonably the eddies observed by the measurements (figure 8-15).

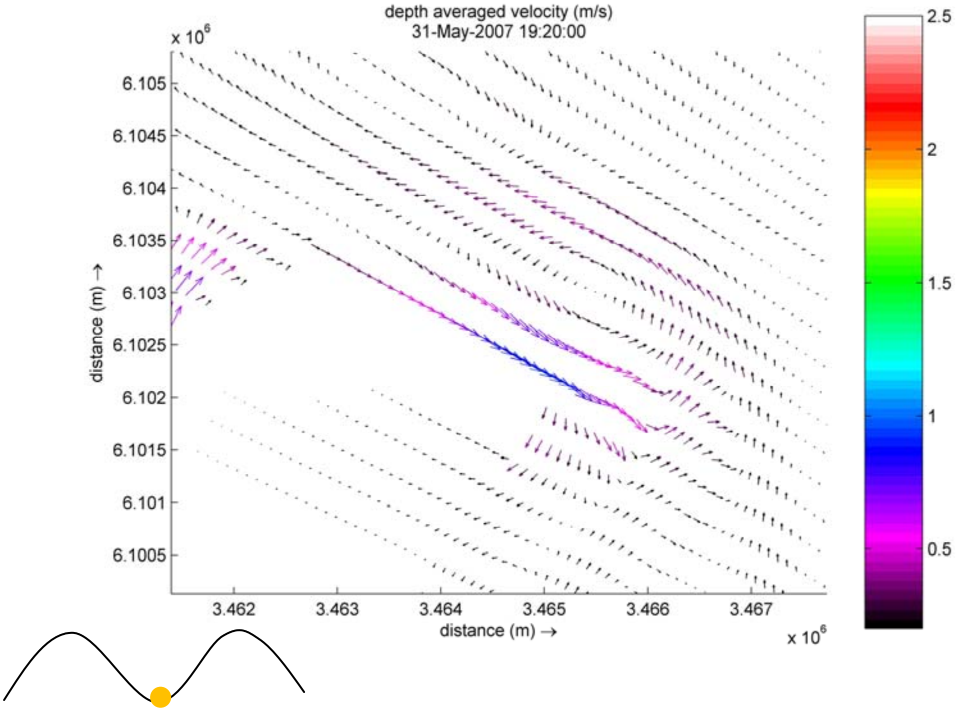

Figure 8-15. Eddies in the area of interest captured by the model.

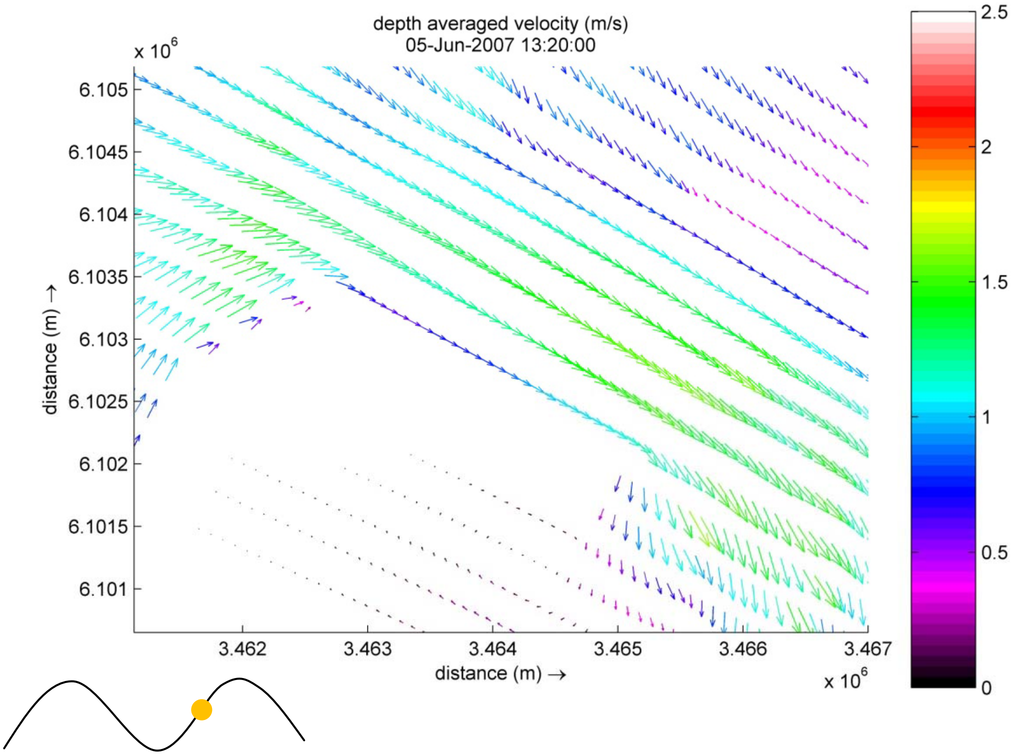

Figure 8-16. Computed depth averaged velocity in the area of interest at 13:20.

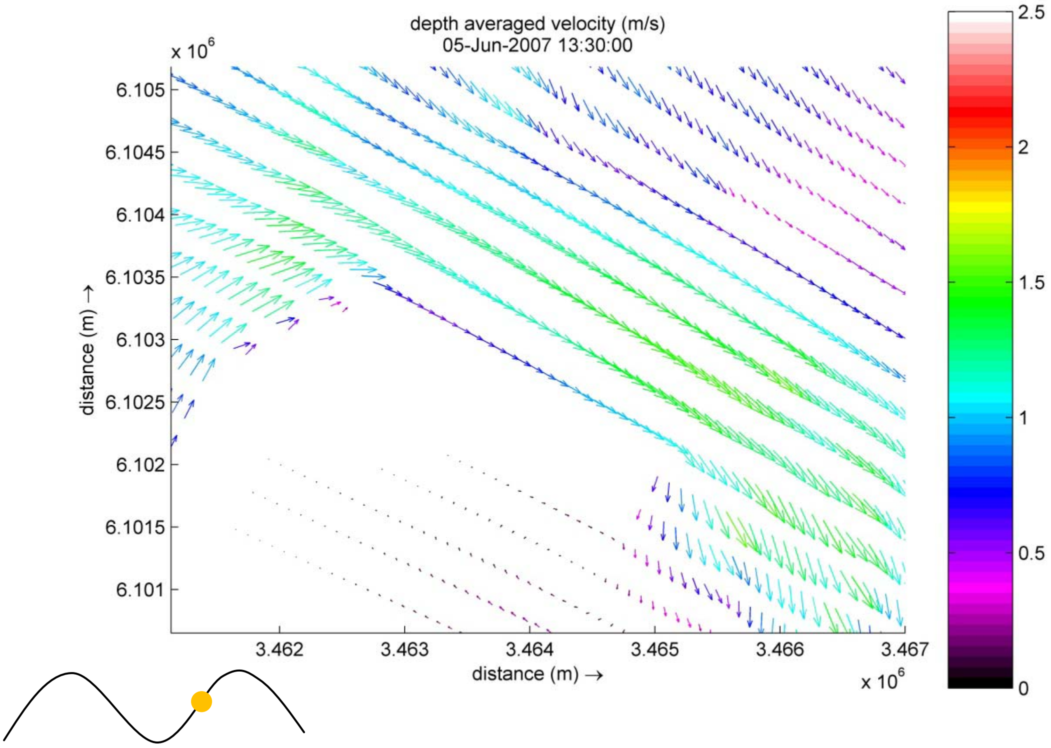

Figure 8-17. Computed depth averaged velocity in the area of interest at 13:30.

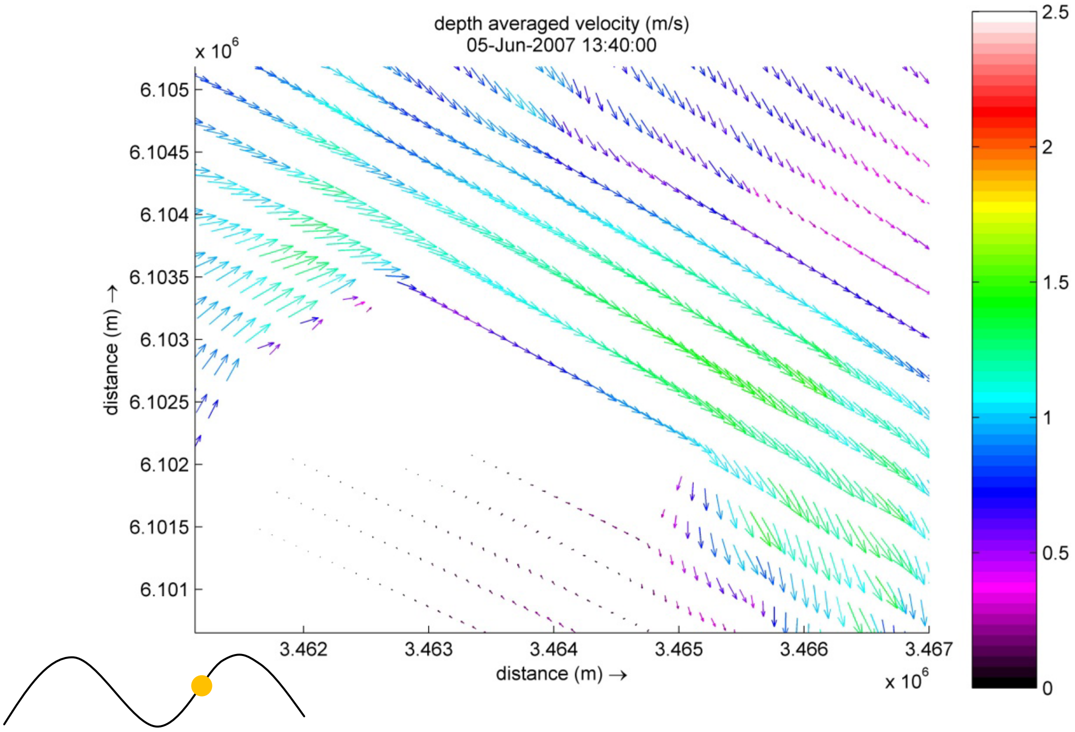

Figure 8-18. Computed depth averaged velocity in the area of interest at 13:40.

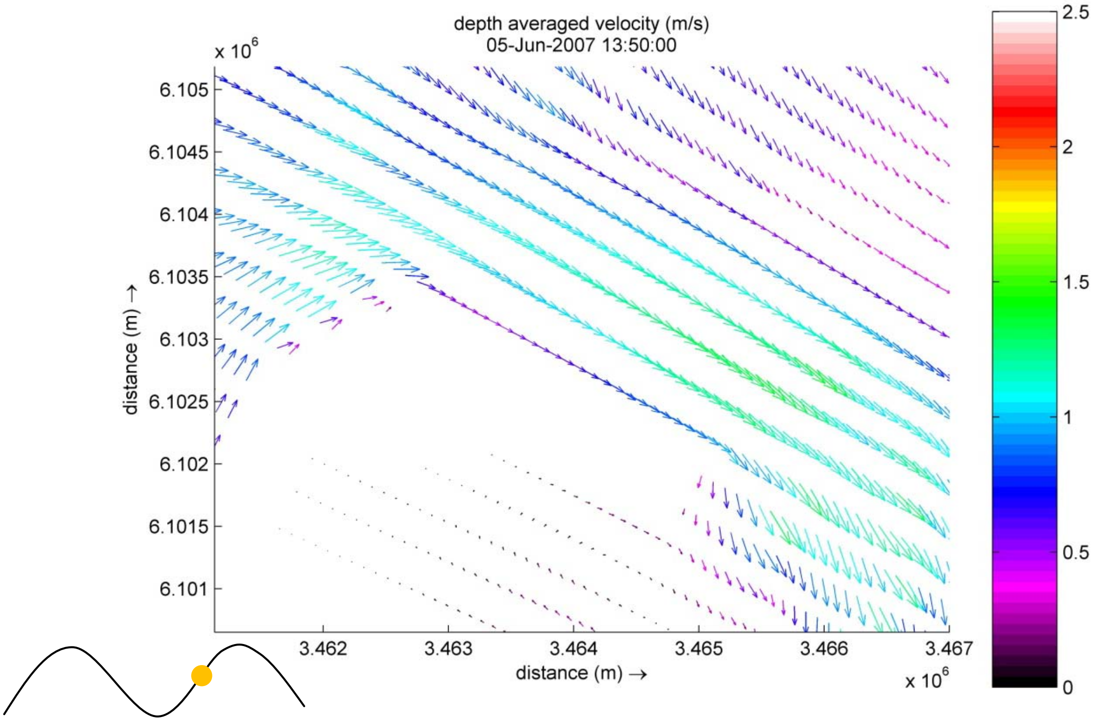

Figure 8-19. Computed depth averaged velocity in the area of interest at 13:50.

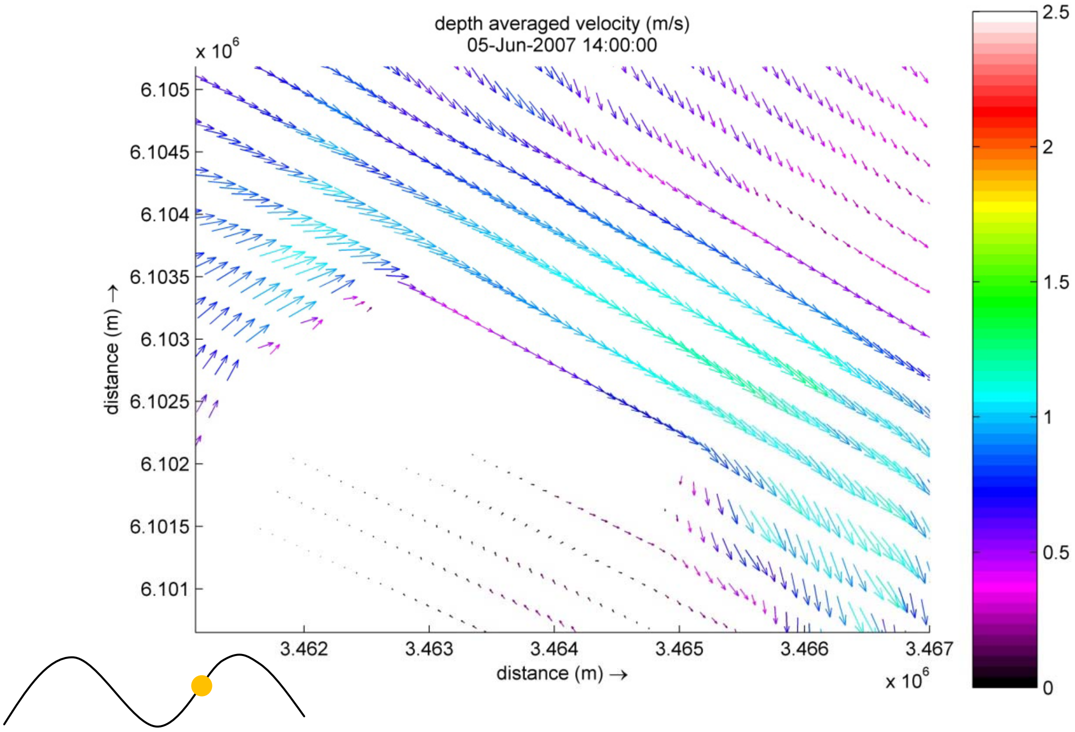

Figure 8-20. Computed depth averaged velocity in the area of interest at 13:50.

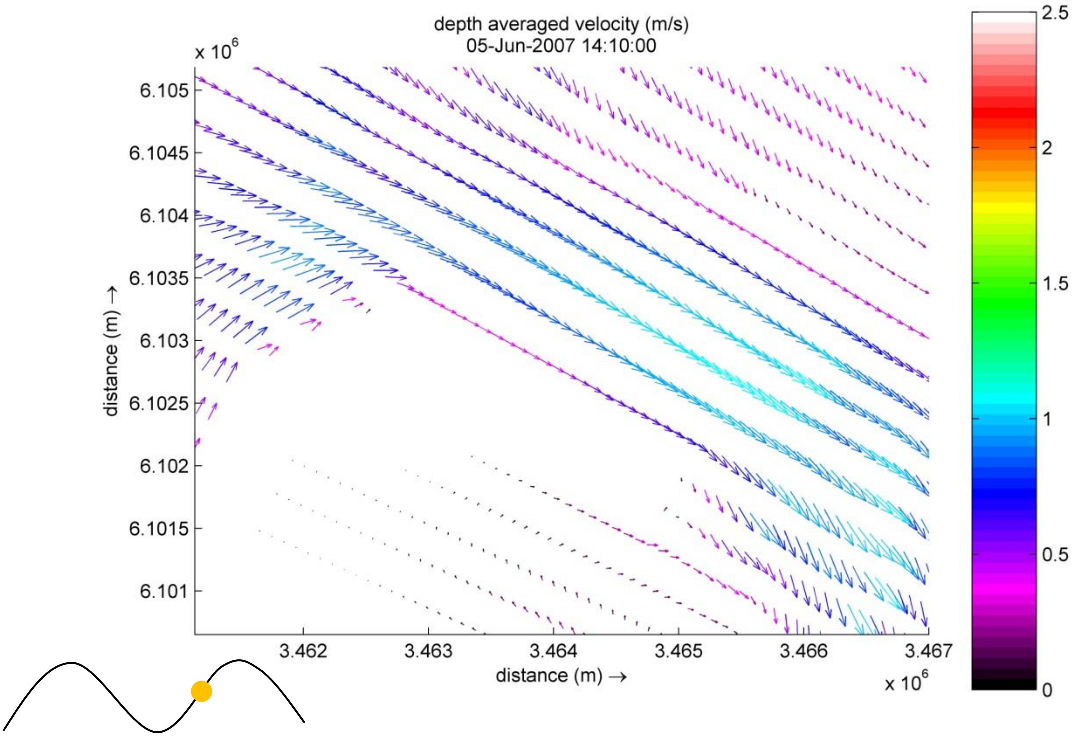

Figure 8-21. Computed depth averaged velocity in the area of interest at 14:10.

Even it is necessary the direct visualization for the data and the avoidance of the distortions due to the interpolation method, for the unbiased validation of the model is accomplishable. In the area of interest, the grid horizontal resolution of the model is 100 m; On the other hand, the grid cell size of the datasets from the RDCP is 15 m. The computed depth averaged velocity was linear interpolated in order to succeed the same resolution between the measured and the computed data, figures 8-23–8-25. The measurements were kept untouched to conserve the signatures from the sea bottom structures. Three datasets from the model with a time interval of 20 min were interpolated, at 13:20, 13:40, and 14:00.

The depth average velocity show higher values at 13:20. It is obvious that at the start (west) and the end (east) of the channel the velocity is lower than in the middle of the channel. These alterations are due to the topography of the area.

The comparison between the surface observed data and the computed data show good agreement in terms of velocity magnitude, even though that the result from the 2DH model is the depth averaged velocity. In table 8-2, the maximum and the minimum values of the velocity of the RDCP dataset 392 and the three computed dataset are summarized. The difference between the values of the current surface velocity from the RDCP and the computed velocity of the model, (for the selected time series of the model) ranges from 0.3–0.7 m/s.

Table 8-2. Maximum and minimum values of the velocities from the RDCP and the model.

Dataset	Maximum velocity (m/s)	Minimum velocity (m/s)
RDCP 392	1.9	0.3
model 13:20	1.6	0.6
model 13:40	1.4	0.5
model 14:00	1.2	0.4

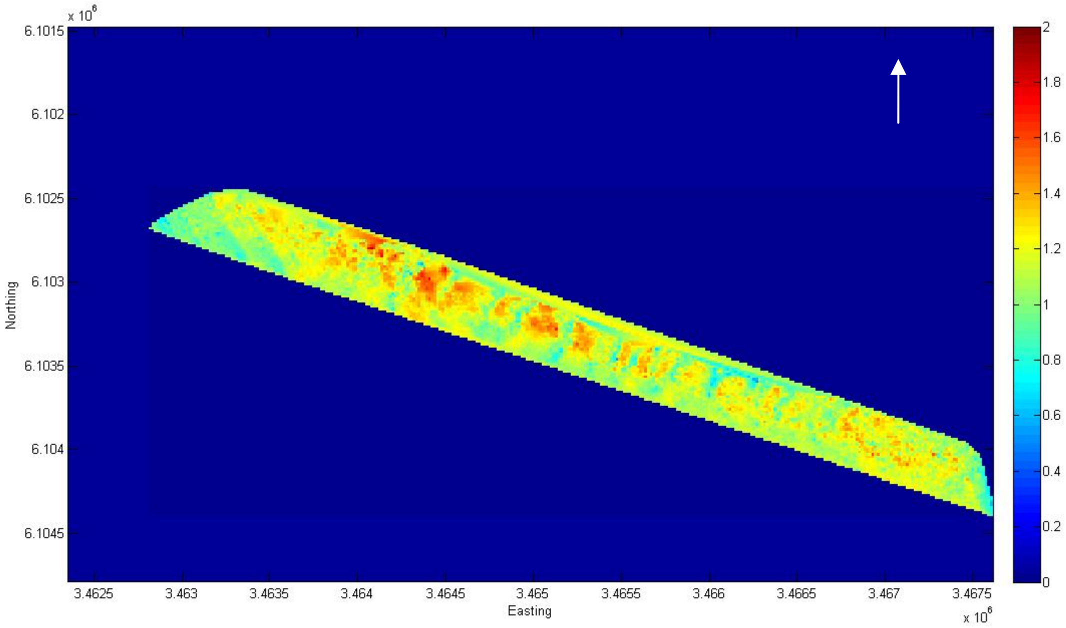

Figure 8-22. Surface current speed (m/s), RDCP dataset 392 measured on the 5th of June at 13:24–13:58.

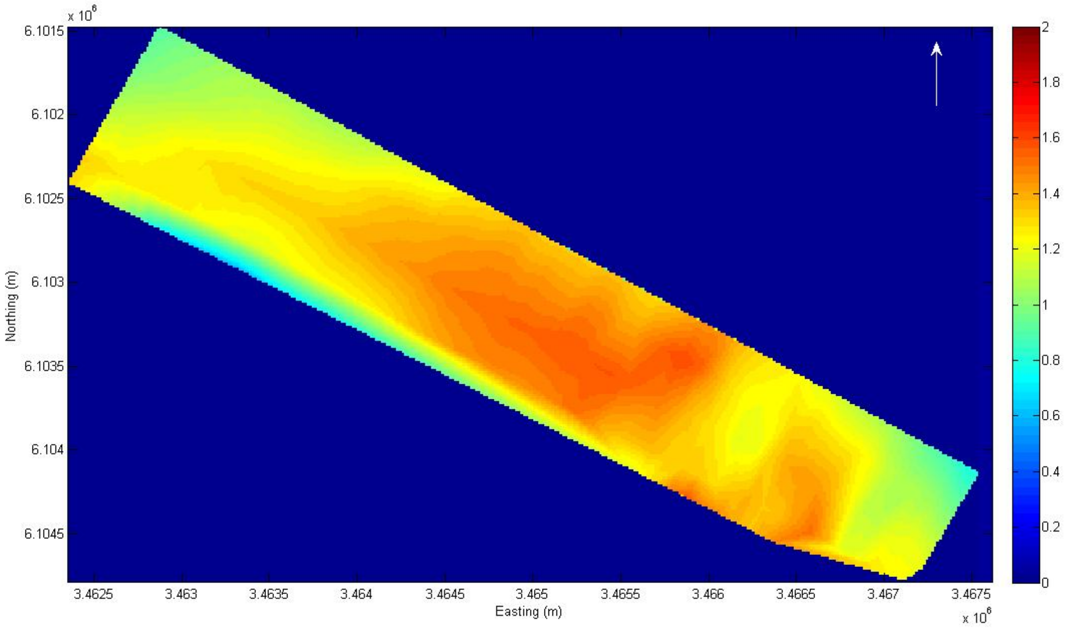

Figure 8-23. Computed Depth averaged velocity (m/s), on the 5th of June at 13:20.

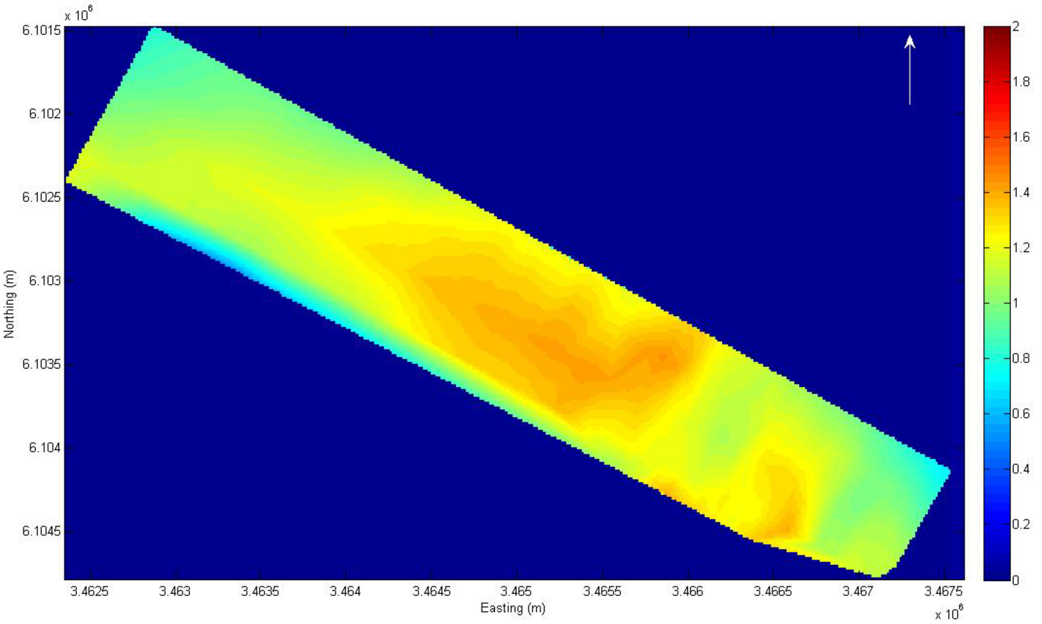

Figure 8-24. Computed Depth averaged velocity (m/s), on the 5th of June at 13:40.

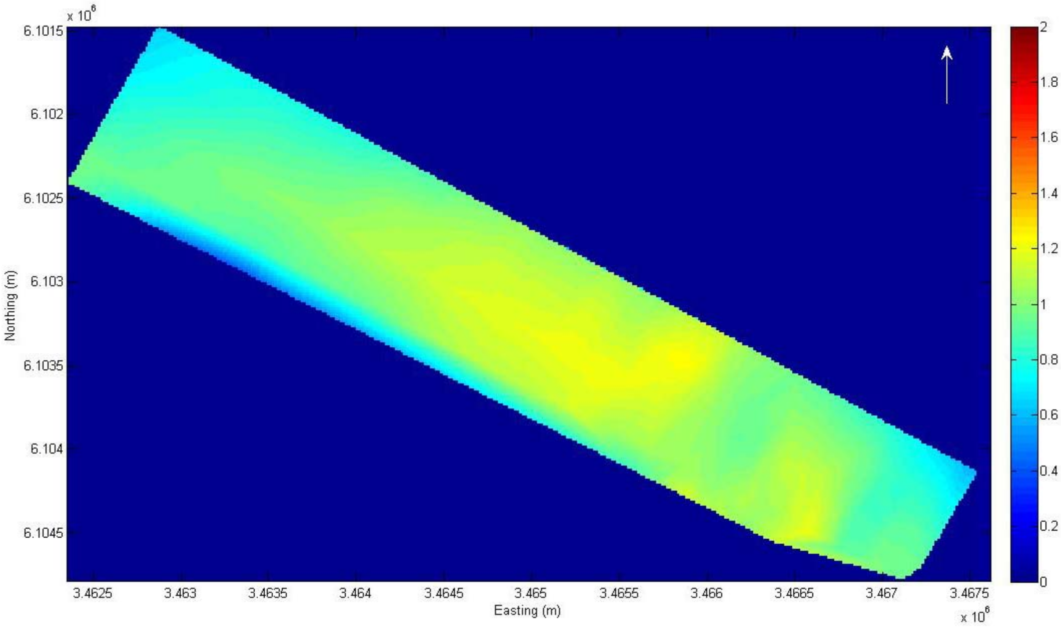

Figure 8-25. Computed Depth averaged velocity (m/s), on the 5th of June at 14:00.

9 Conclusions and Outlook

The complexity of the Lister Tief tidal inlet is proved by the observed and in situ data and also by the model results. The dominating hydrodynamic mechanisms were identified by the spatial monitoring of the current field in three dimensions. The Radar Doppler Current Profiler (RDCP) provides a two dimension horizontal profiles. The Acoustic Doppler Current Profiler provides vertical profiles of the water column current. A two dimension depth integrated flow model (2DH) was used to simulate the data.

The data from the RDCP and the echo-sounder were geo-gridded in a common mash with spatial resolution 15 m. The correlation between the surface current field and the bathymetry was determined. The development and validation of a 2DH hydrodynamic flow model for the Lister Tief, Sylt Island, on the basis of Delft-3D software was accomplished.

The Radar Doppler Current Profiler is a new radar system still under development that can provide a geo gridded map of the surface current field. The observation of the surface current by the RDCP, is possible only when low wind conditions exist at the surveying area, therefore the impact of waves is weak. Even if the radars signal cannot penetrate through the sea surface, it was observed that signatures of the bottom topography modify the surface current field. The modification is identified by the alterations of the surface current speed. The peak values of the surface current speed are observed above the crest of undersea sand dunes. If the bathymetry is not changing in time during the investigation, the fluctuation at the sea surface are steered by the bed relief. The bottom topography plays a prominent role in the hydrodynamics of the Lister Tief. The correlation between the surface current speed and the depth was found to be inverse proportional. The depth averaged velocity obtained by the ADCP confirms this relation. In the water column, the velocity at the boundary layers has low values contradict by the high values observed at the middle, therefore the effect of the bottom and the sea surface is significant. This phenomenon exists in both tidal phases. The results of the analysis of the ADCP data lead to conclude that the water transport over the narrowing channel accelerate, known as the phenomenon of channelization.

The hydrodynamics in the Lister Tief have been simulated using a 2DH model in the environment of DELFT-3D as the area is highly complex. Different model setting and parameters were checked for their effect on the model. A curvilinear grid with a resolution of 90–130 m and time step 1 min was found adequate for capturing the hydrodynamics in the area of study. The open sea boundaries for the flow model were determined according to nesting sequence covering the entire North Sea. The simulations covered a period of 15 days. During this period the effect of the wind is insignificant. Furthermore, the results lead to the conclusion that the only physical parameter having a significant influence on the model is the bathymetry. The validation of the model was carried out by comparing computed depth averaged velocities and surface current speed measured by the RDCP, for first time.
A good agreement in terms of velocity magnitude was shown, even though that the result from the 2DH model is the depth averaged velocity. Model performance statistics, based on water level measurements, were calculated to assess the model's ability to reproduce the measured currents. The quality of the model can be characterized as Reasonable/Fair due to the standards suggested by Walstra, 2001, which is reasonable for the complex system as a tidal inlet.

The shift between the speed maxima and the cross section is a normal effect of the advection, which becomes evident by the effect that the decorrelation increases with the increase of water depth. This must be described in later studies.

This is one large step towards the identification of the mechanisms, by measurements and model simulation, but still there are possibilities for improvement. In order to obtain a better performance of the model further improvements may be done. The development of a 3D model is mainly restricted due to the fact of the high fluctuations of the velocity in the Lister Tief. The bottom roughness was considered constant for the whole model domain; a creation of a roughness map may lead to better results.

References

AHRENDT K. (2001), Expected effect of climate changes on Sylt Island: results from a multidisciplinary German project, Climate Research, vol.18, pp.141–146.

ALPERS W., HASSELMANN K. (1982), Spectral Signal to Clutter and Thermal Noise Properties of Ocean Wave Imaging Synthetic Aperture Radars, *International Journal of Remote Sensing*, 3, pp 423–446.

ANDERSEN T.J. (1999), Suspended sediment transport and sediment reworking at an intertidal mudflat, the Danish Wadden Sea. *Meddelelser fra Skalling-Laboratoriet,* 37, pp. 1–72.

BAYERL K., KOSTER R. & MURPHY D., (1998), Verteilung und Zusammensetzung der Sedimente im Lister Tidebecken. In: C. Gätje and K. Reise, Editors, *Ökosystem Wattenmeer-Austausch, Transport-und Stoffumwandlungsprozesse, Chap. 1.1.2*, Springer, Heidelberg, pp. 31–38.

BAUMERT Z.H., SIMPSON H.J., SUNDERMANN J. (2005), Marine Turbulence Theories Observations and Models, Results of the CARTUM project, Cambridge University Press.

BERLINSKI D. (1996), The end of materialist science. Forbes ASAP, pp. 146–160.

BERTIN X., CHAUMILLON E., SOTTOLICHIO A., PEDREROS R. (2004), Tidal inlet response to sediment infilling of the associated bay and possible implications of human activities: the Marennes – Oleron Bay and the Maumuson Inlet, France, *Continental Shelf Research*, 25, pp. 1115–1131.

BOALCJ C. R., McMANUS J. (1989), Wave refraction pattern recognition off North Sea coasts using X-band radar. *Developments in Estuarine and Coastal Study Techniques,* J. McManus and M. Elliott, Eds., Olsen and Olsen, 79–84.

BRAUN N., ZIEMER F., BEZUGLOV A., CYSESKI M., SCHYMURA G. (2008), Sea surface current features observed by doppler radar, *IEEE Transactions on Geoscience and Remote Sensing*, vol. 46, no. 4.

DAVIS R.A. Jr. (1964), Tidal influence on Barrier Island Morphodynamics: Examples from Florida, USA, *Journal of Coastal Reasearch*, SI39, pp.97–101.

DALRYMPLE R.W., RHODES R.N (1995), Estuarine dunes and bars, Geomorphology and Sedimentology of Estuaries, Development in Sedimentology, 53, chapter 13.

DE SWART H.E., ZIMMERMAN J.T.F. (2009), Annual Review, Fluid Mechanics, 41, pp. 203–229.

ELIAS E.P.L, CLEVERINGA J., BUIJSMAN M.C., ROELVINK J.A., STIVE M.J.F. (2006), Field and model data analysis of sand transport patterns in Texel Tidal inlet (the Netherlands), Coastal Engineering, 53, pp.505–529.

FLAMPOURIS S. (2006), Investigation of correlations between radar deduced bathymetries due to the outer impact of a storm in the area "Salzsand". Master thesis, Coastal geosciences and Engineering, CORELAB, University of Kiel.

GERLAD D.M.F. (2005), Tidal Inlet, Encyclopedia of Coastal Science, M.L. Schwartz, Department of Geology, Western University, WA, USA, Springer.

GEYL WF. (1976), Tidal neo-morphs*, Z. Geomorphology*, 20, pp.308–330.

GONZÁLEZ J. A., CHARLES S. MELCHING, AND KEVIN A. OBERG (1996), Analysis of open-channel velocity measurements collected with an acoustic Doppler Current Profiler, Proceedings from the 1st International Conference On New/Emerging Concepts for Rivers Organized by the International Water Resources Association, Chicago, USA.

GORDON R.L. (1996), Acoustic Doppler Current Profilers: Principles of Operation – A practical Primer.

HAYES M.O. (1979), Barrier island morphology as a function of tidal and wave regime, In: S.P. Leatherman, Editor, Barrier Islands, Academic Press, New York, pp. 1–27.

HENNINGS I., HERBERS D., PRINZ K., ZIEMER F. (2004), First Results of the OROMA experiment in the Lister Tief of the German Bight in the North Sea, *Proceedings of the European Association of Remote Sensing*, 3, pp.86–104.

HENNINGS I., HERBERS D. (2006), Radar imaging mechanism of marine sand waves at very low grazing angle illumination caused by unique hydrodynamic interactions, *Journal of Geophysical Research*, vol. 111.

HUBBAN D.K, OERTEL G., NUMMEDAL D. (1979), The role of waves and tidal currents in the development of tidal-inlet sedimentary structures and sand body geometry; examples from North Carolina, South Carolina, and Georgia, *Journal of Sedimentary Petrology* Volume 49, Issue 4, pp. 1073–1092.

KAPPENBERG, J., FANGER, H.-U., MULLER, A. (1997), Currents and suspended particulate matter in tidal channels of the Sylt-Romo basin, Senckenbergiana maritima, 29 (1/6), pp. 93–100.

LESSER G.R., ROELVINK J.A., VAN KASTER J.A.T.M., STELLING G.S. (2004), Development and validation of three-dimensional morphological model, *Coastal Engineering*, 51, pp. 883–915.

LONGLEY P., BATTY M. (1996), Spatial analysis: modeling in a GIS environment, John Wiley and Sons.

LONGUET-HIGGINS M.S. (1952), On the statistical Distribution of the Heights of Sea Waves, *Journal of Marine Research*, 11, pp.245–266

OPEN UNIVERSITY (2000), Waves, Tides and shallow – water processes, 2nd edition, The Open University Press.

OROMA (2004), Results from the European project "Operational Radar and Optical Mapping in monitoring hydrodynamic, morphodynamic and enveronmental parameter for coastal management".

PEJRUP M., LARSEN M. & EDELVANG K. (1997), A fine-grained sediment budget for the Sylt–Rømø tidal basin. *Helgoländer Meeresuntersuchungen,* 51, pp. 253–268.

PICKARD L.G., EMERY J.W. (1990), Descreptive Physical Oceanography, An Introduction, 5th Edition, pp. 102, Oxford, Auckland, Boston, Johannesburg, Melbourne, New Dehli, Butterworth-Heinemann.

PINNET R.P. (2000), Invitation to Oceanography, Colgate University, Jones and Bartlett, Sudbury Massachusetts.

POND S., PICKARD L.G. (1983), Introductory Dynamical Oceanography, 2nd edition, p. 260, Elsevier Butterworth-Heinemann, Pregamont Press.

RODI W., LAURENCE D. (1999), Engineering Turbulence Modeling and Experiments 4, *Proceedings of the 4th International Symposium on Engineering Turbulence Modeling and Measurements*, Elsevier.

SCHAFER M. (2006), Computational engineering: introduction to numerical methods, Springer Science & Business.

SHIELDS D. F.,. KNIGHT JR., TESTA S. III, COOPER M. CH. (2003), Use of acoustic doppler current profiles to describe velocity disturbutions at the reach scale, *Journal of American Water Resources Association*, pp.1397–1408.

SHEPARD D. (1968), A two-dimensional interpolation function for irregularly-spaced data, *Proceedings of the 1968 ACM National Conference*, pp. 517–524.

SKINNER B., STHEPHEN J., PORTER C. (1989), The Dynamic Earth, John Wiley & Sons.

STOCKMANN, K., RIETHMÜLLER, R., HEINEKE, M., AND GAYER, G. (2009), On the morphological long-term development of dumped material in a low-energetic environment close to the German Baltic coast. *Journal of Marine Science* 75, 409–420

LUMBORG U., WINDELIN A. (2003), Hydrography and cohesive sediment modelling: application to the Rømø-Dyb tidal area, *Journal of Marine Systems* Elsevier, London, vol. 38, pp. 287–303.

SUTHERLAND J., WALSTRA D. J. R., CHESHER T. J., VAN RIJIN L. C., SOUTHGATE H. N. (2004), Evaluation of Coastal area modeling systems at an estuary mouth, *Coastal Engineering*, vol. 51, pp. 119–142.

Van DE KREEKE J. (1992), Stability of Tidal Inlets; Escoffier's Analysis, Journal of the American Shore & Beach Preservation Association, vol. 60, no.1, pp. 9–12.

Van DE KREEKE J., Hydrodynamics of Tidal Inlet, lectures notes on Coastal and Estuarine Studies.

Van DEN BAAREN A. (2006), Canadian Technical annual report of Hydrography and Ocean Sciences 210, 2000.

Van GASTEL K. (1989), Velocity profiles of tidal currents over sand waves, *Netherlands Journal of Research*, 21, 3, pp. 159–170.

VAN RIJIN L.C., GRASMEIJER B.T., RUESSINK, B.G. (2000), Measurements errors of instruments for velocity, wave height, sand concentration and bed levels in field conditions, University of Utrecht/Delft Hydraulics Report.

Van VEEN J., VAN DER SPEK AD.J.F., STIVE J.F., ZITMAN T. (2005), Ebb and Flood channel systems in the Netherlands Tidal waters 1, *Journal of Coastal Research*, 21, pp. 1107–1120.

WALSTRA D.J.R., SUTHERLAND J., HALL L., BLOGG H., VAN ORMONDT M. (2001), Verification and comparison of two hydrodynamic area models for an inlet system. *Proceedings of Coastal Dynamics '01, the Fourth Conference on Coastal Dynamics, Lund, Sweden*, ASCE, Reston, VA, pp. 433–442.

WENET C.D. (1980), Coastal Circulation and Wind-Induced Currents, Annual Review of Fluid Mechanics Vol. 12: 271–301 (Volume publication date January).

WU LI CHU (2008), Spatio-Temporal Wavelet Transform of Non-homogeneous Sea Surface Wave Field on a varying Topography, Phd dissertation.

WILKENS J., JUNGE I., HOYME H. (2005), Modelling of waves in a Tidal Flat Area in the South-Eastern German Bight, Die Kuste, No. 69.

ZIEMER F., CYSEWSKI M. (2006), High resolution Sea Surface Maps produced by Scanning with Ground Based Doppler Radar, eProceedings IGARSS.

Manual of DELFT-3D 2007

ESRI User Guide

Manual of RD Instruments

APPENDICES

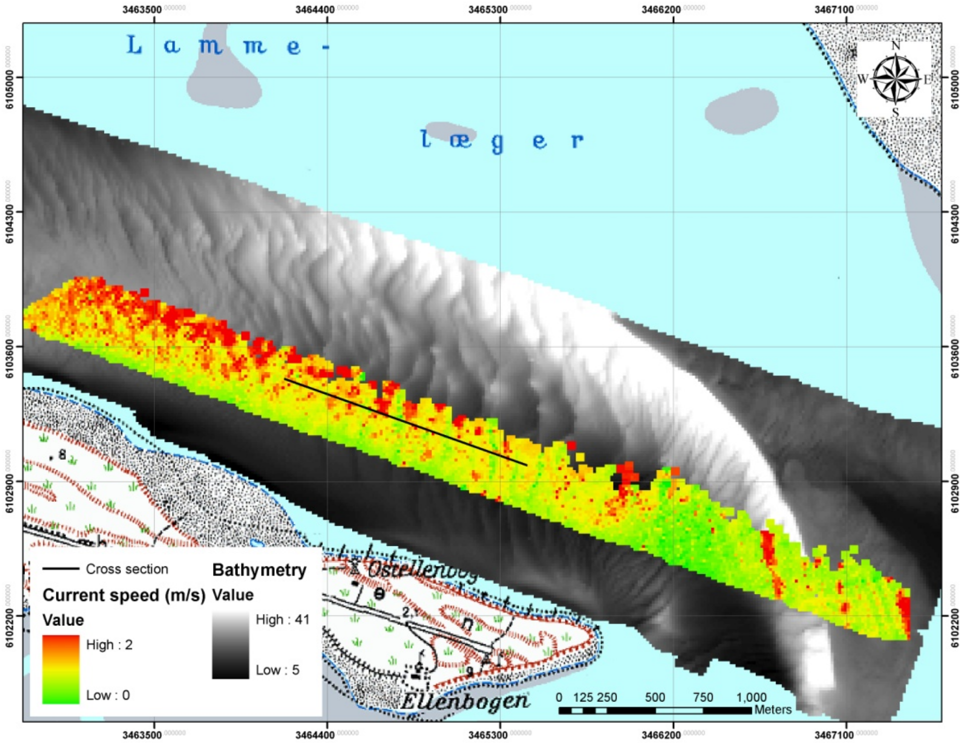
3463500
3464400
3465300
3466200
3467100
6105000
6104300
6103600
6102900
6102200
L a m m e -
l æ g e r
Ellenbogen
Cross section
Current speed (m/s)
Value
High : 2
Low : 0
Bathymetry
Value
High : 41
Low : 5
0 125 250 500 750 1,000
Meters
N
S
W
E

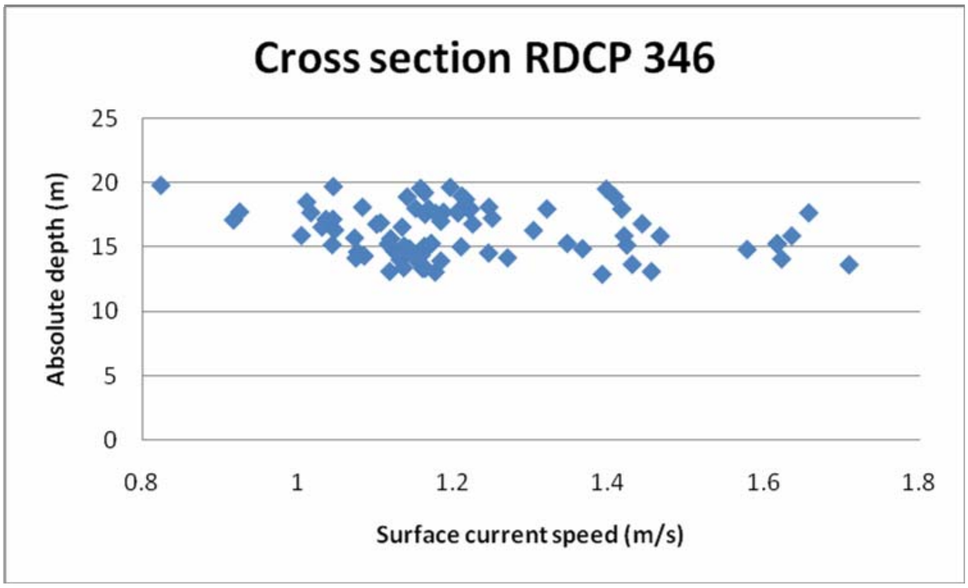
Cross section RDCP 346
Absolute depth (m)
25
20
15
10
5
0
0.8
1
1.2
1.4
1.6
1.8
Surface current speed (m/s)

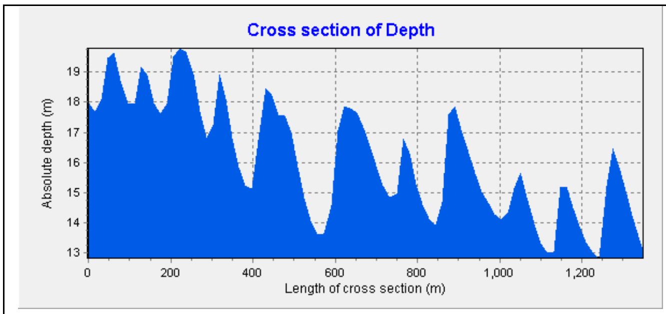
Cross section of Depth
Absolute depth (m)
19
18
17
16
15
14
13
0
200
400
600
800
1,000
1,200
Length of cross section (m)

a)

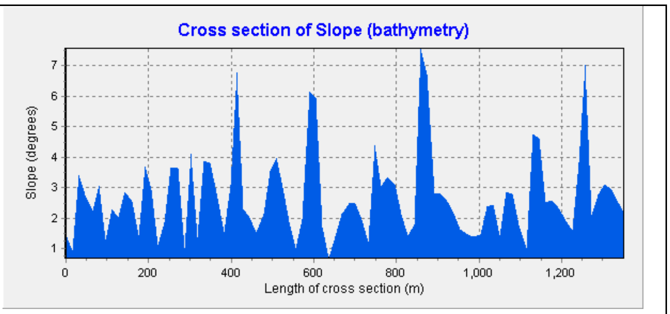
Cross section of Slope (bathymetry)
Slope (degrees)
7
6
5
4
3
2
1
0
200
400
600
800
1,000
1,200
Length of cross section (m)

b)

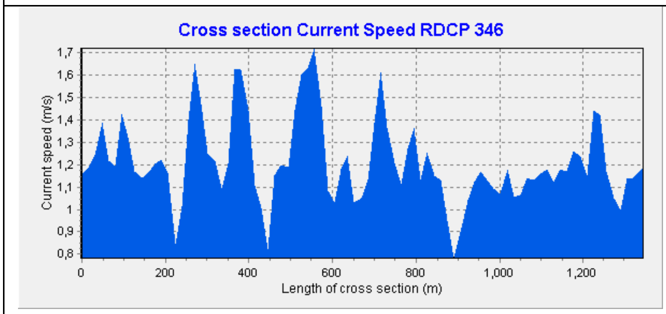
Cross section Current Speed RDCP 346
Current speed (m/s)
1,7
1,6
1,5
1,4
1,3
1,2
1,1
1
0,9
0,8
0
200
400
600
800
1,000
1,200
Length of cross section (m)

c)

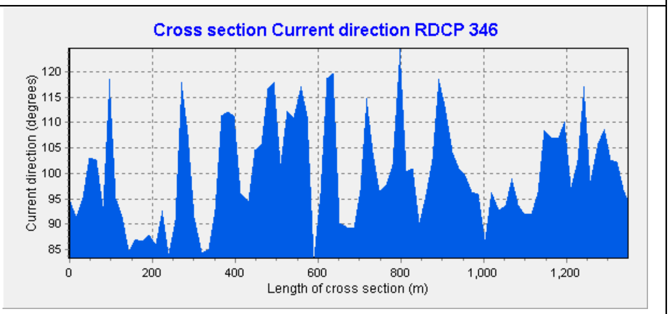
Cross section Current direction RDCP 346
Current direction (degrees)
120
115
110
105
100
95
90
85
0
200
400
600
800
1,000
1,200
Length of cross section (m)

d)

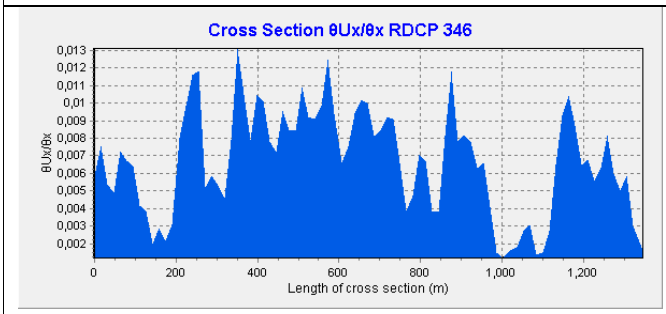
Cross Section θUx/θx RDCP 346
θUx/θx
0,013
0,012
0,011
0,01
0,009
0,008
0,007
0,006
0,005
0,004
0,003
0,002
0
200
400
600
800
1,000
1,200
Length of cross section (m)

e)

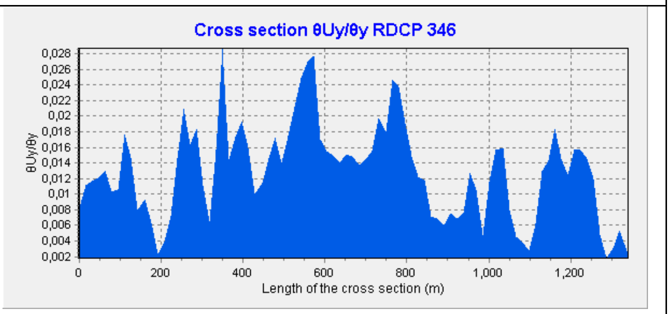
Cross section θUy/θy RDCP 346
θUy/θy
0,028
0,026
0,024
0,022
0,02
0,018
0,016
0,014
0,012
0,01
0,008
0,006
0,004
0,002
0
200
400
600
800
1,000
1,200
Length of the cross section (m)

f)

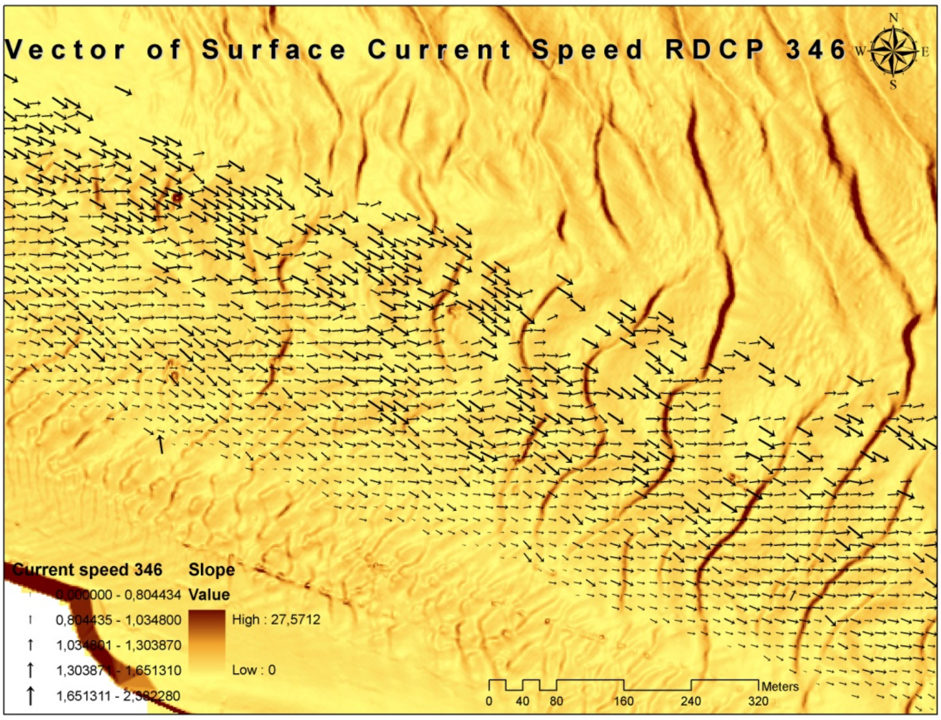
Vector of Surface Current Speed RDCP 346
N
W
E
S
Current speed 346
0,000000 - 0,804434
0,804435 - 1,034800
1,034801 - 1,303870
1,303871 - 1,651310
1,651311 - 2,382280
Slope
Value
High : 27,5712
Low : 0
0
40
80
160
240
320
Meters

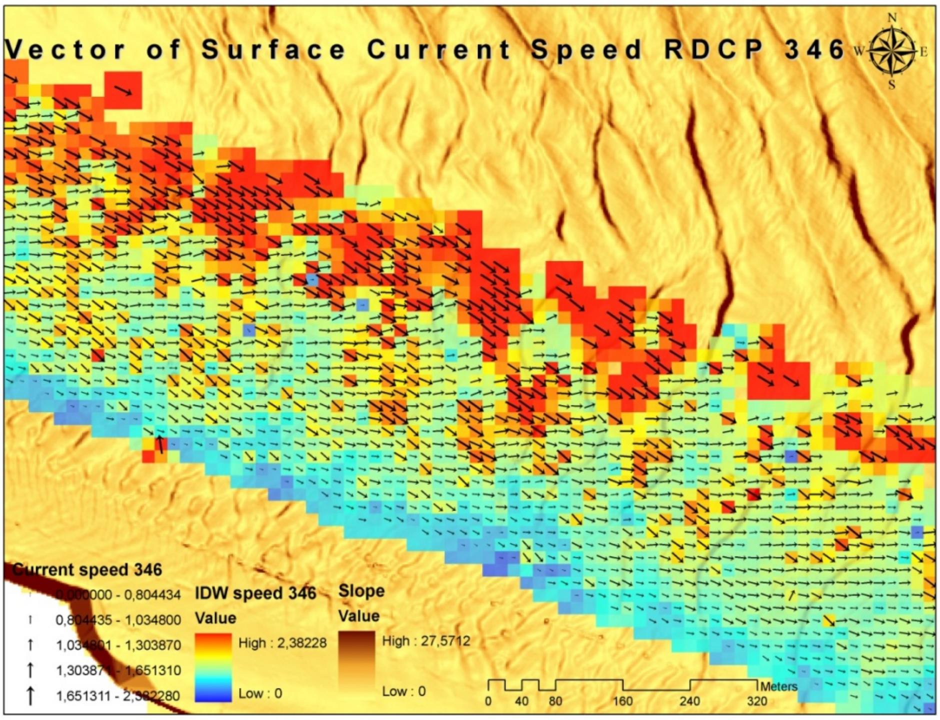
Vector of Surface Current Speed RDCP 346
N
W
E
S
Current speed 346
0,000000 - 0,804434
0,804435 - 1,034800
1,034801 - 1,303870
1,303871 - 1,651310
1,651311 - 2,382280
IDW speed 346
Value
High : 2,38228
Low : 0
Slope
Value
High : 27,5712
Low : 0
0
40
80
160
240
320
Meters

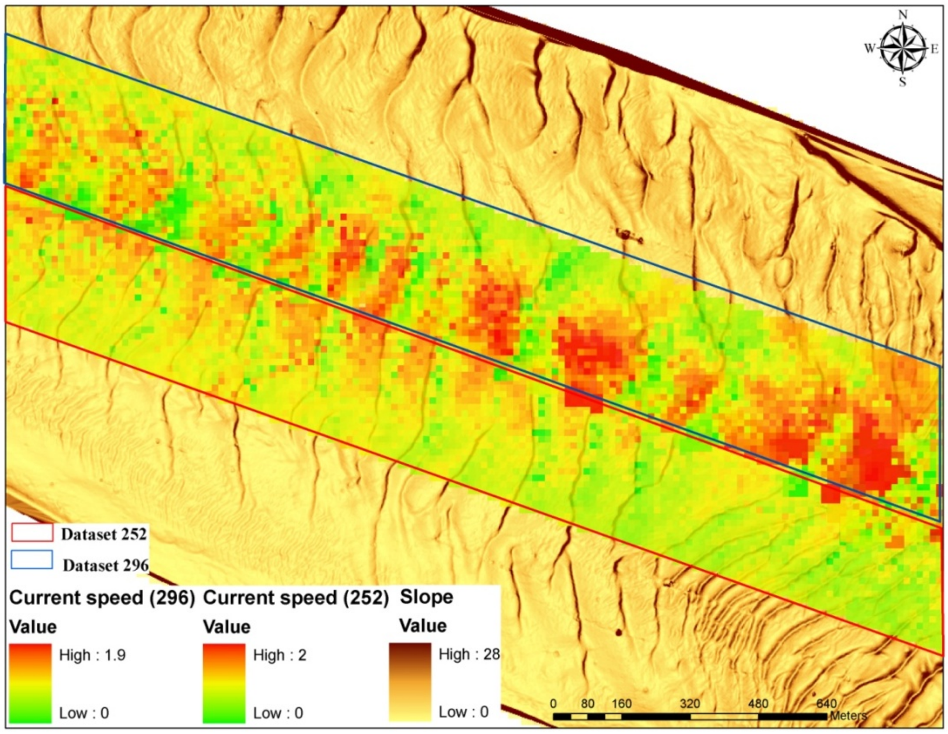
N
W
E
S
Dataset 252
Dataset 296
Current speed (296)
Value
High : 1.9
Low : 0
Current speed (252)
Value
High : 2
Low : 0
Slope
Value
High : 28
Low : 0
0
80
160
320
480
640
Meters

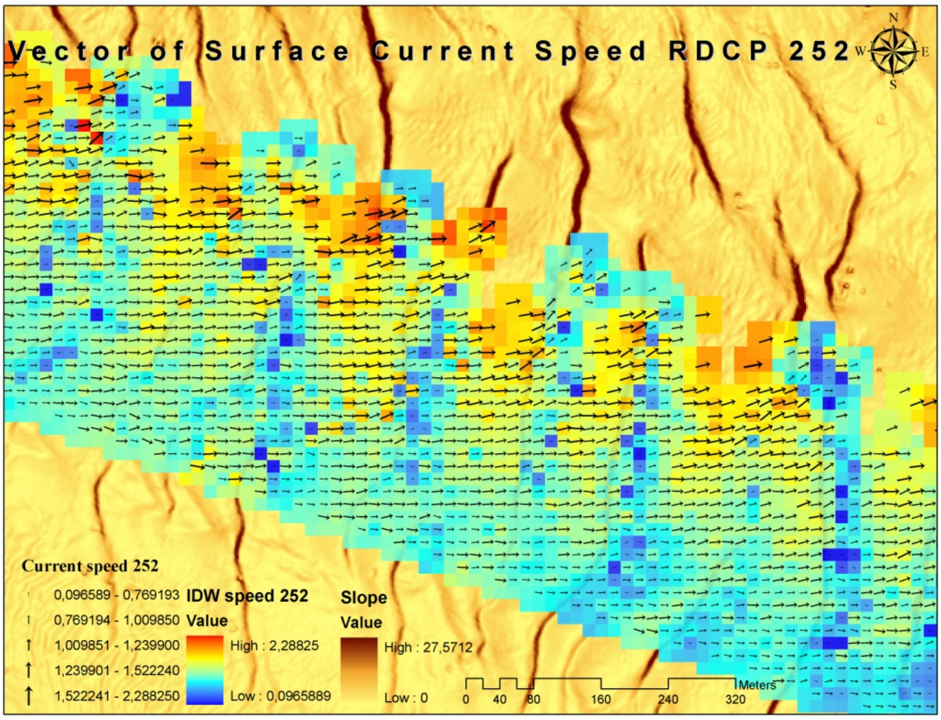
Vector of Surface Current Speed RDCP 252
N
W
E
S
Current speed 252
0,096589 - 0,769193
0,769194 - 1,009850
1,009851 - 1,239900
1,239901 - 1,522240
1,522241 - 2,288250
IDW speed 252
Value
High : 2,28825
Low : 0,0965889
Slope
Value
High : 27,5712
Low : 0
0
40
80
160
240
320
Meters

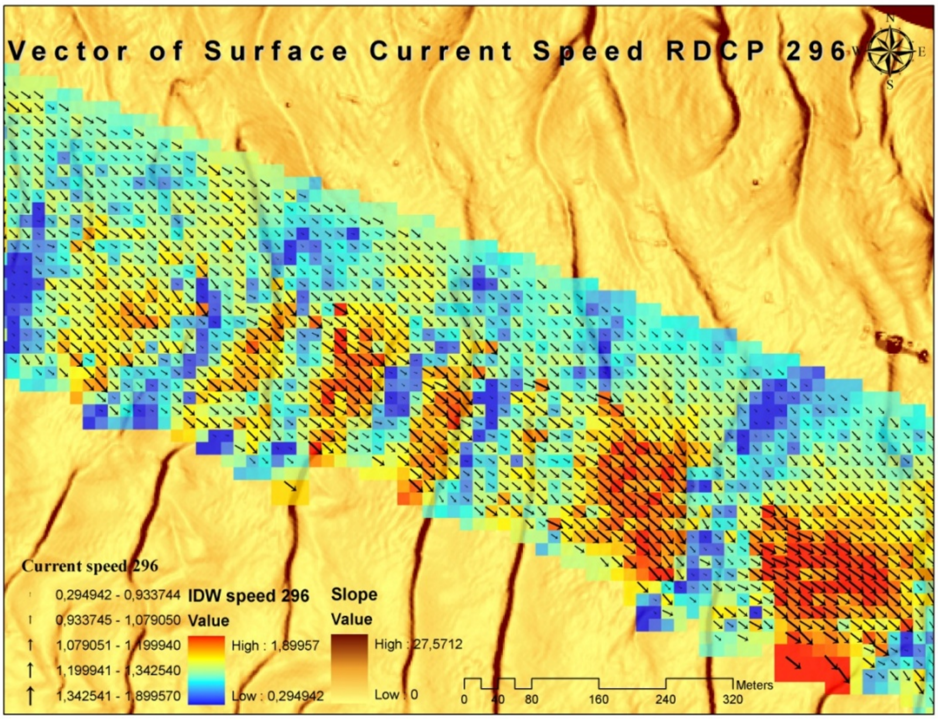
Vector of Surface Current Speed RDCP 296
N
W
E
S
Current speed 296
0,294942 - 0,933744
0,933745 - 1,079050
1,079051 - 1,199940
1,199941 - 1,342540
1,342541 - 1,899570
IDW speed 296
Value
High : 1,89957
Low : 0,294942
Slope
Value
High : 27,5712
Low : 0
0
40
80
160
240
320
Meters

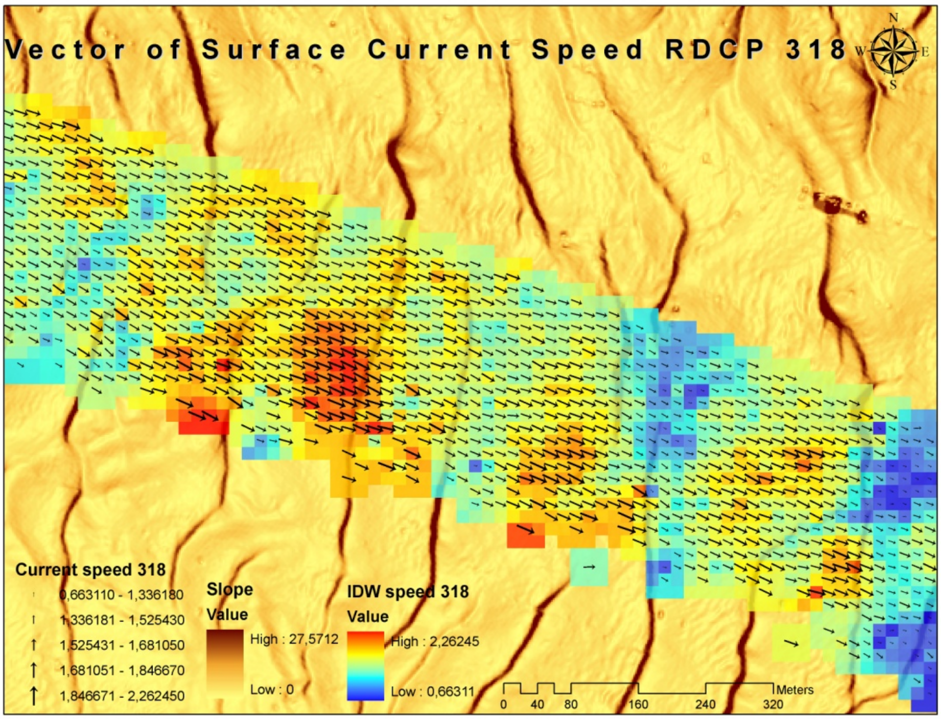
Vector of Surface Current Speed RDCP 318
N
W
E
S
Current speed 318
0,663110 - 1,336180
1,336181 - 1,525430
1,525431 - 1,681050
1,681051 - 1,846670
1,846671 - 2,262450
Slope
Value
High : 27,5712
Low : 0
IDW speed 318
Value
High : 2,26245
Low : 0,66311
0
40
80
160
240
320
Meters

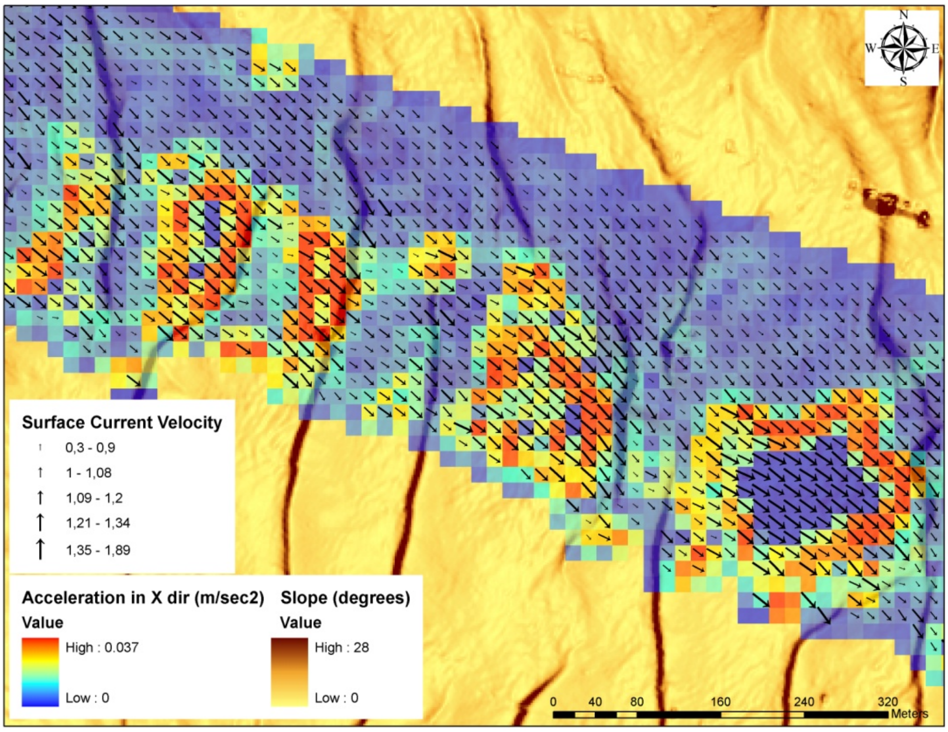
N
W
E
S
Surface Current Velocity
0,3 - 0,9
1 - 1,08
1,09 - 1,2
1,21 - 1,34
1,35 - 1,89
Acceleration in X dir (m/sec2)
Value
High : 0.037
Low : 0
Slope (degrees)
Value
High : 28
Low : 0
0
40
80
160
240
320
Meters

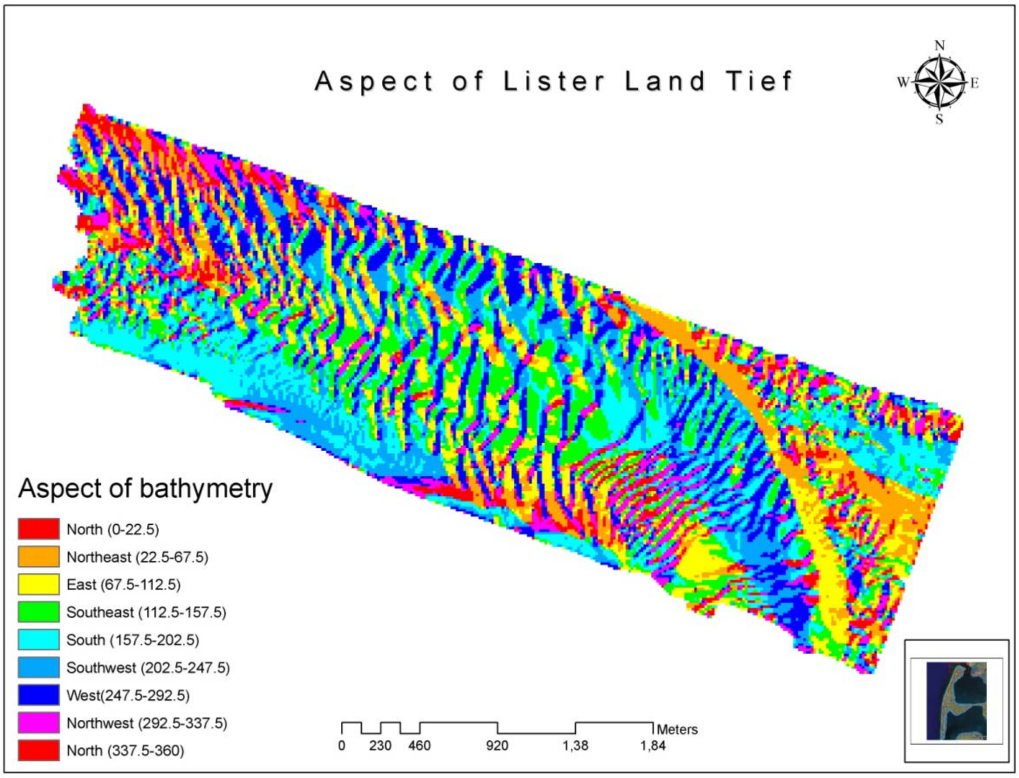
Aspect of Lister Land Tief
N
W
E
S
Aspect of bathymetry
🟥 North (0-22.5)
🟧 Northeast (22.5-67.5)
🟨 East (67.5-112.5)
🟩 Southeast (112.5-157.5)
South (157.5-202.5)
Southwest (202.5-247.5)
🟦 West(247.5-292.5)
🟪 Northwest (292.5-337.5)
🟥 North (337.5-360)
0
230
460
920
1,38
1,84
Meters

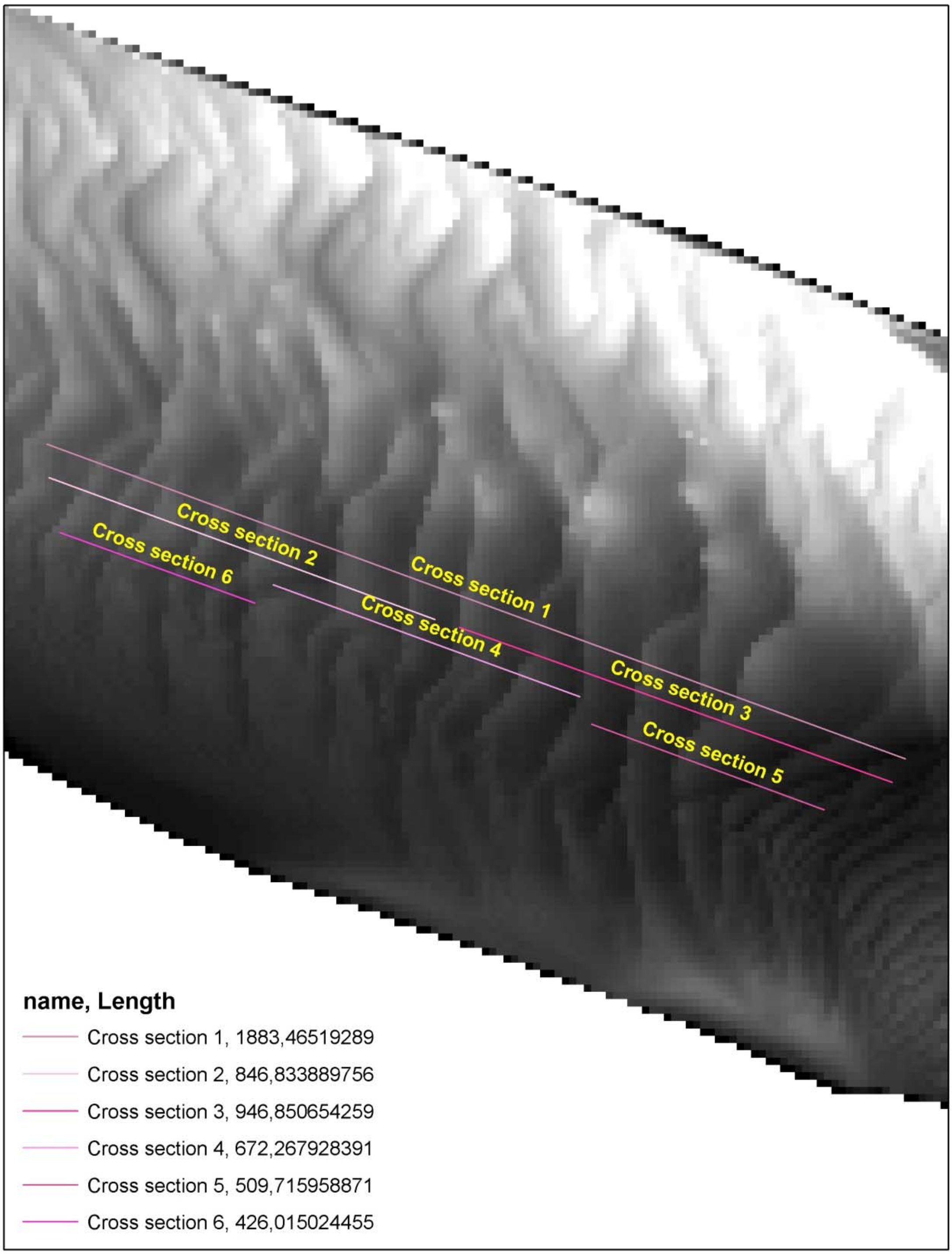
Cross section 2
Cross section 6
Cross section 1
Cross section 4
Cross section 3
Cross section 5
name, Length
Cross section 1, 1883,46519289
Cross section 2, 846,833889756
Cross section 3, 946,850654259
Cross section 4, 672,267928391
Cross section 5, 509,715958871
Cross section 6, 426,015024455

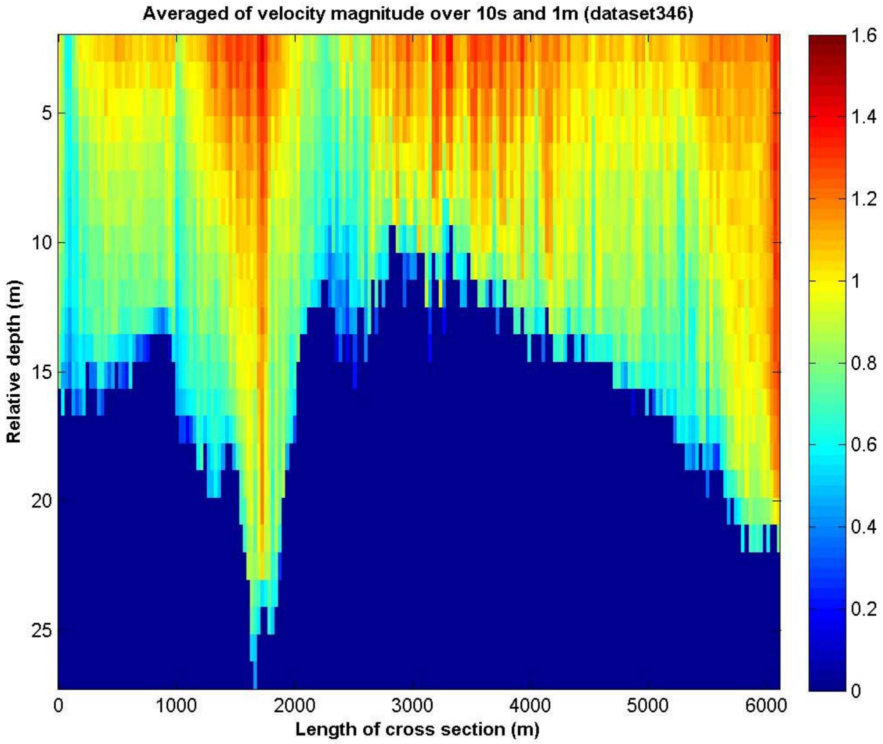
Averaged of velocity magnitude over 10s and 1m (dataset346)
Relative depth (m)
5
10
15
20
25
0
1000
2000
3000
4000
5000
6000
Length of cross section (m)
1.6
1.4
1.2
1
0.8
0.6
0.4
0.2
0

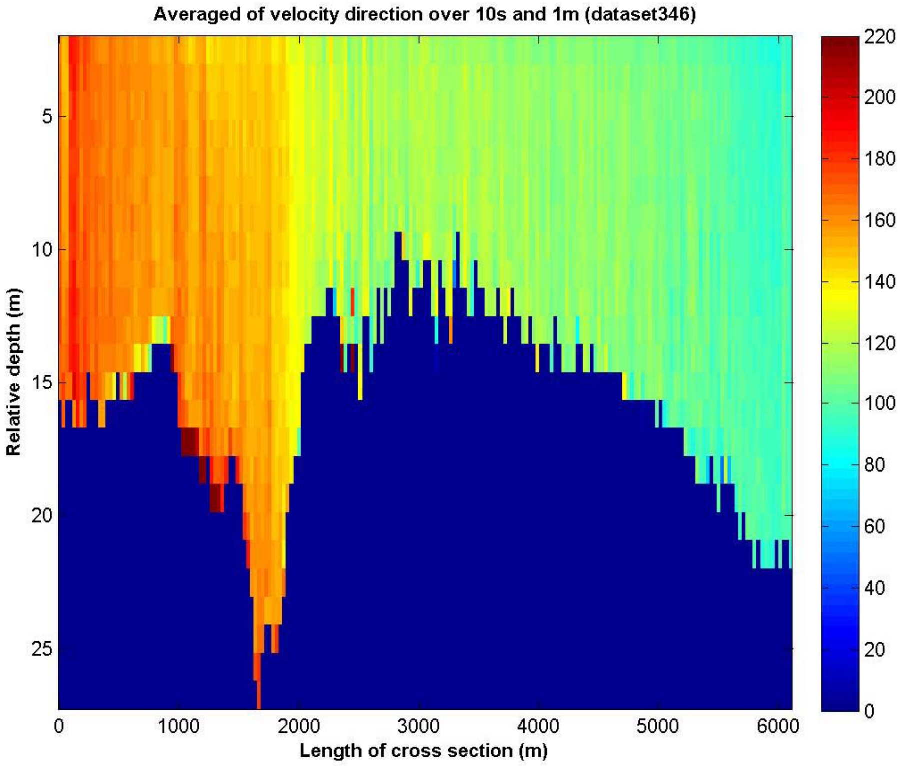
Averaged of velocity direction over 10s and 1m (dataset346)
Relative depth (m)
5
10
15
20
25
0
1000
2000
3000
4000
5000
6000
Length of cross section (m)
220
200
180
160
140
120
100
80
60
40
20
0

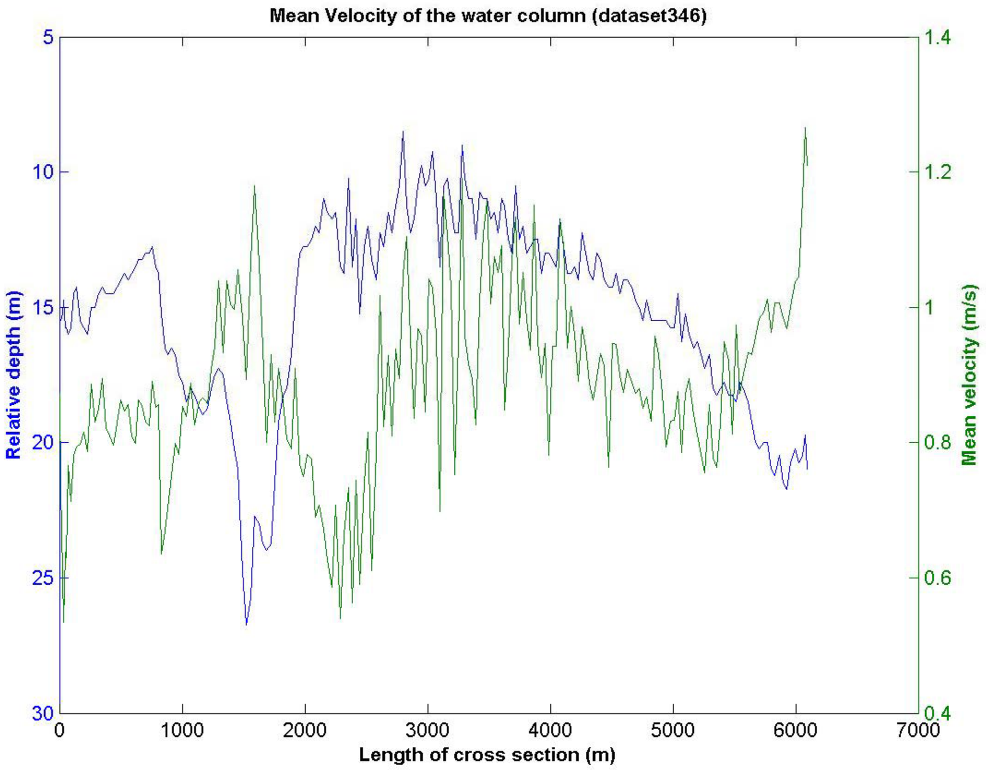
Mean Velocity of the water column (dataset346)
Relative depth (m)
5
10
15
20
25
30
Mean velocity (m/s)
1.4
1.2
1
0.8
0.6
0.4
0
1000
2000
3000
4000
5000
6000
7000
Length of cross section (m)

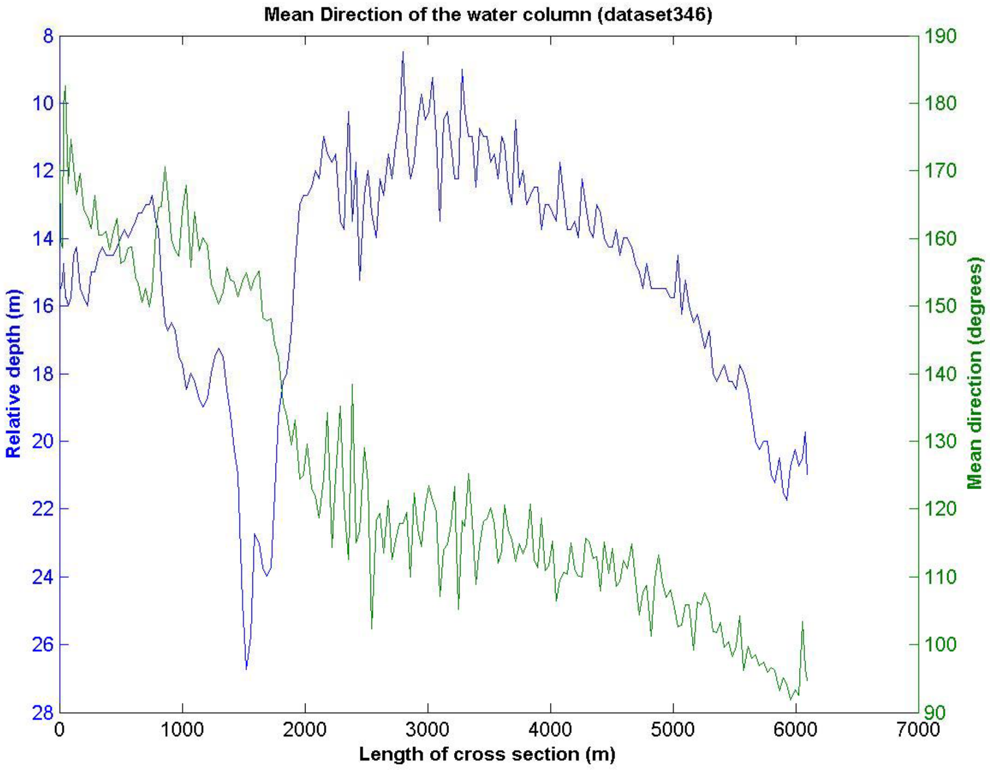
Mean Direction of the water column (dataset346)
Relative depth (m)
8
10
12
14
16
18
20
22
24
26
28
Mean direction (degrees)
190
180
170
160
150
140
130
120
110
100
90
0
1000
2000
3000
4000
5000
6000
7000
Length of cross section (m)

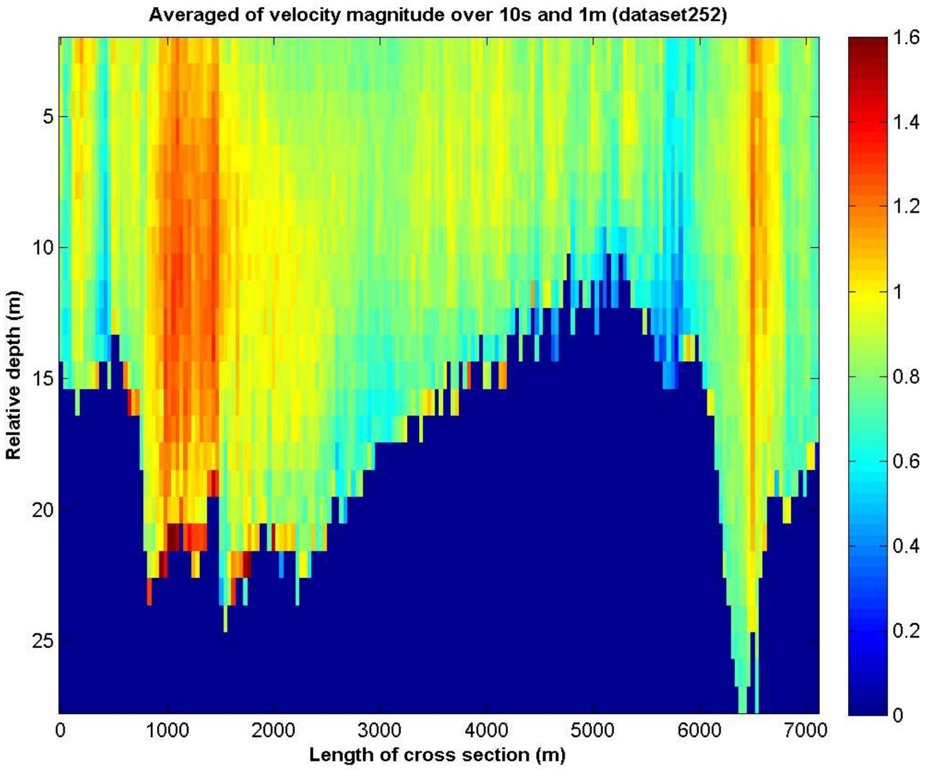
Averaged of velocity magnitude over 10s and 1m (dataset252)
Relative depth (m)
5
10
15
20
25
0
1000
2000
3000
4000
5000
6000
7000
Length of cross section (m)
1.6
1.4
1.2
1
0.8
0.6
0.4
0.2
0

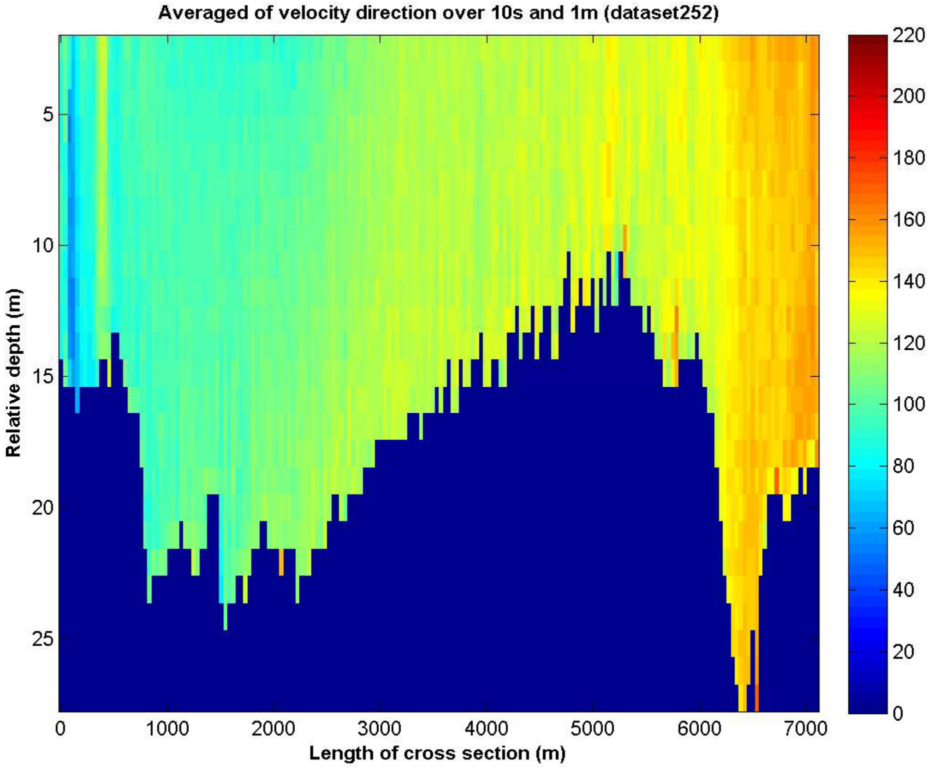
Averaged of velocity direction over 10s and 1m (dataset252)
Relative depth (m)
5
10
15
20
25
0
1000
2000
3000
4000
5000
6000
7000
Length of cross section (m)
220
200
180
160
140
120
100
80
60
40
20
0

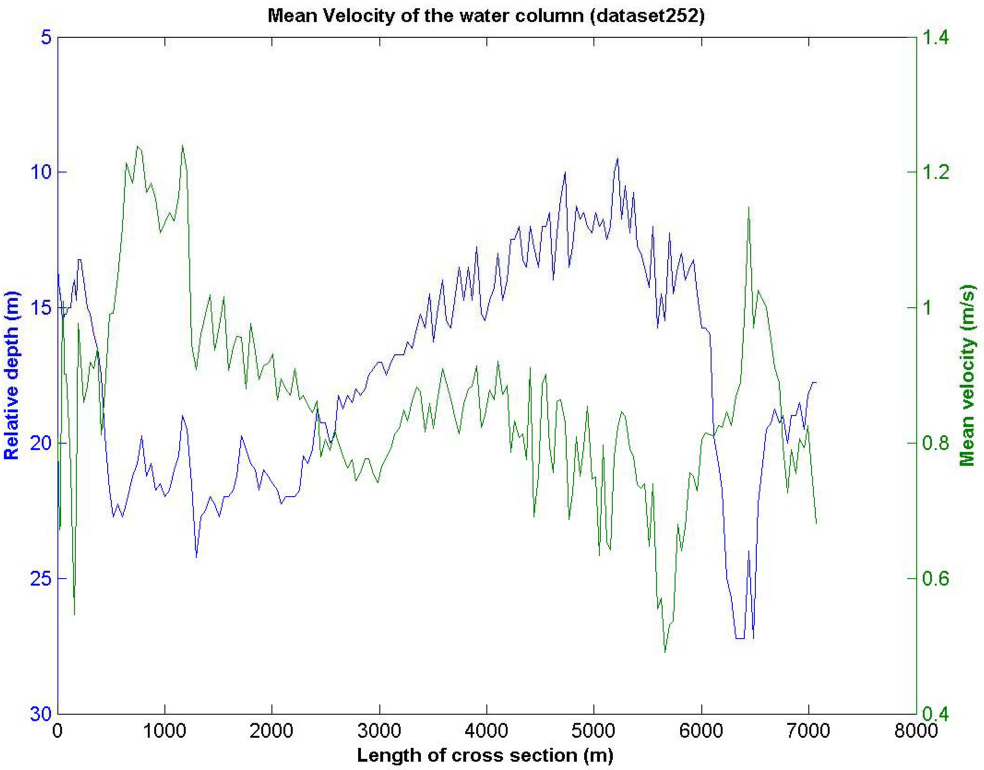
Mean Velocity of the water column (dataset252)
Relative depth (m)
5
10
15
20
25
30
Mean velocity (m/s)
1.4
1.2
1
0.8
0.6
0.4
0
1000
2000
3000
4000
5000
6000
7000
8000
Length of cross section (m)

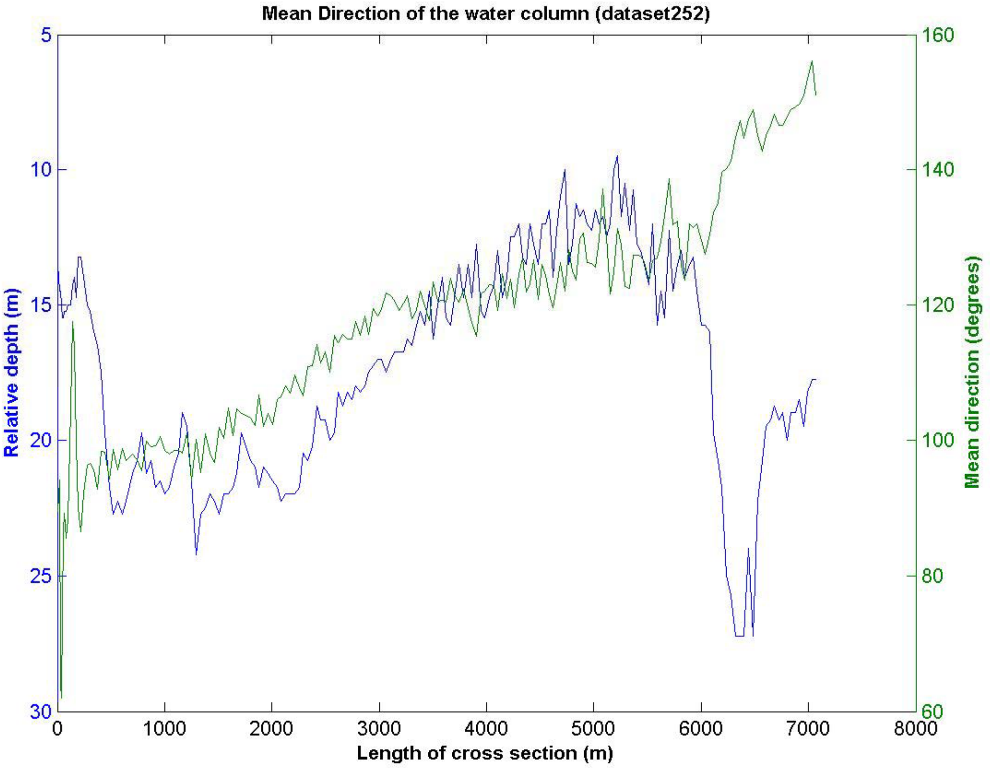
Mean Direction of the water column (dataset252)
Relative depth (m)
5
10
15
20
25
30
Mean direction (degrees)
160
140
120
100
80
60
0
1000
2000
3000
4000
5000
6000
7000
8000
Length of cross section (m)

```
load data252

data252(:,1) = adcp_252(:,1);
data252(:,2:6) = adcp_252(:,4:8);
data252(:,5) = data252(:,5)/100;
size_data = size(data252);
%% Mean velocity of the water column for every 10seconds
count = 1;sum_mag = 0;count_7 =1;sum_dir = 0;count_avg =1;
for i=1:size_data(1)
    if (data252(i,1) == 7)
        count_7 = count_7+1;
    end

    if (count_7 == 4)
        count = 1;sum_mag = 0;count_7 =1;sum_dir = 0;

        plot_10sec (count_avg,1:6) = data252(i-1,1:6); %#ok<AGROW>
        plot_10sec (count_avg,7:8) = avg_dat(i-1,1:2); %#ok<AGROW>
        count_avg = count_avg +1;
    end
        if (data252(i,1) ~= 7)
            sum_mag = sum_mag + data252(i,5);
            avg_dat(i,1) = sum_mag/count; %#ok<AGROW>

            sum_dir = sum_dir + data252(i,6);
            avg_dat(i,2) = sum_dir/count; %#ok<AGROW>
        count=count+1;

        end
end

data252(:,7:8)=avg_dat(:,1:2);

figure, scatter(plot_10sec(:,4),plot_10sec(:,5))


[AX,H1,H2] =
plotyy(plot_10sec(:,1),(plot_10sec(:,4)),plot_10sec(:,1),plot_10sec(:,5),'p
lot');
set(gca,'YDir','reverse')
title('Mean Velocity of the water column for every 10sec
(dataset252)','FontWeight','Bold')
xlabel('Length of cross section (m)','FontWeight','Bold')
set(get(AX(1),'Ylabel'),'String','Relative depth (m)','FontWeight','Bold')
set(get(AX(2),'Ylabel'),'String','Mean velocity (m/s)','FontWeight','Bold')


%% Mean velocity for every 25 centimeters

bath(:,1) = data252(:,1);
bath(:,2) = data252(:,4);
count = 1;
    for i = 1:32261;
        if bath(i,1) == 7;
            bath(i,2) = NaN;
             bath(i,1) = NaN;
             data252(i,4) = NaN;
             distance(count) = bath(i-1,1); %#ok<AGROW>
             count = count+1;
        end
    end
```

```
min_bath = min(bath(:,2));
max_bath = max(bath(:,2));
start_ship = 0;
end_ship = max(bath(:,1));

[x_grid,y_grid]=ndgrid(distance,min_bath:0.25:max_bath);
%
%current_mag_col=nanm([1,572],[1,100],1);
%current_dir_col=nanm([1,572],[1,100],1);
for i=1: size_data(1)

        data_dist = data252(i,1);
        data_depth = data252(i,4);

    if (data252(i,1)~=7 && data252(i,4) ~= NaN)

        [ind_x]=find((x_grid(:,1)-0.1< data_dist) &(x_grid(:,1)+0.1>
data_dist));

        [ind_y]=find((y_grid(1,:)-0.1 < data_depth)& (y_grid(1,:)+0.1 >
data_depth));

        current_mag_col(ind_y,ind_x)= data252(i,5);
        current_dir_col(ind_y,ind_x)= data252(i,6);
    end
end

for i=1:57200

        if current_mag_col(i) == 0
        current_mag_col(i) = NaN;
        end

        if current_dir_col(i) == 0
        current_mag_dir(i) = NaN;
        end

end

depth1=min_bath:0.25:max_bath;

figure, imagesc(distance,depth1,current_mag_col)
colorbar, caxis([0 1.6]);
title('Mean Velocity (m/s) every 25cm vs Depth','FontWeight','Bold')
xlabel('Length of cross section (m)','FontWeight','Bold')
ylabel('Relative depth (m)','FontWeight','Bold')


figure, imagesc(distance,depth1,current_dir_col);
colorbar, caxis([0 200]);
title('Direction of Velocity every 25cm vs Depth','FontWeight','Bold')
xlabel('Length of cross section (m)','FontWeight','Bold')
ylabel('Relative depth (m)','FontWeight','Bold')

%%Average every 10sec
```

```
cursize = size(current_dir_col);

for i=1:cursize(1)*cursize(2)
    if (current_dir_col(i)== 0)
        current_dir_col(i)= NaN;
    end
end

count_avg = 1;
for i=3:3:cursize(2)
    for j=1:cursize(1)

        average_mag_10sec(j,i-2:i) = nanmean(current_mag_col(j,i-2:i));
        average_dir_10sec(j,i-2:i) = nanmean(current_dir_col(j,i-2:i));
%              average_mag_10sec(j,count_avg) =
nanmean(current_mag_col(j,i));
%              average_dir_10sec(j,count_avg) =
nanmean(current_dir_col(j,i));
%              count_avg = count_avg+1;
    end
end

figure, imagesc(distance,depth1,average_mag_10sec)
colorbar, caxis([0 1.6]);
title('Magnitude of Velocity (m/s) averaged for every
10sec','FontWeight','Bold')
xlabel('Length of cross section (m)','FontWeight','Bold')
ylabel('Relative depth (m)','FontWeight','Bold');

figure, imagesc(distance,depth1,average_dir_10sec)
colorbar, caxis([0 220])
title('Direction of Velocity averaged for every 10sec','FontWeight','Bold')
xlabel('Length of cross section (m)','FontWeight','Bold')
ylabel('Relative depth (m)','FontWeight','Bold');

%% New arrays in order to put out the NaN data, AVERAGE_MAGNITUDE_10sec
counter_line=1; counter_column=1;
    for i=1:3:570
        new_avg_mag_10sec(1:100,counter_column)=average_mag_10sec(1:100,i);
        counter_line=counter_line+1;
        counter_column=counter_column+1;
    end

 depth_new2_10sec=min_bath:0.25:max_bath;
 depth_new2_10sec=depth_new2_10sec';


%% Delete Nan for the fit and plot data

size_mag2 = size(new_avg_mag_10sec);

for i=1:4 % size_mag2(2)

    data1_10sec=new_avg_mag_10sec(:,i);
    val1_10sec= ~isnan(data1_10sec);
    keep_avg_mag_10sec=data1_10sec(val1_10sec);

    tempdepth_10sec=depth_new2_10sec;
    keep_depth_10sec=tempdepth_10sec(val1_10sec);
```

```
    figure, plot(keep_avg_mag_10sec,keep_depth_10sec,'o')
    %hold on
    set(gca,'YDir','reverse')
    ylim([0 30])
    xlim([0.2 2])
    title(['Velocity averaged every 10sec, ', num2str(distance(i)),'m', '
of the cross section'])
    xlabel('Vertical profile of the Velocity (m/s)','FontWeight','Bold')
    ylabel('Relative depth (m)','FontWeight','Bold')

  filename = [num2str(i) '_velocity_1mdepth'];
  h = gcf;
  print ('-f6', '-djpeg' , filename );
  close (h)
%
% f = fittype('-a*x^n + b','problem','n');
% [c2,gof2] = fit( keep_avg_mag,keep_depth,f,'problem',2);
% plot(c2,'m')


end



%% Average every 1m depth

for i=4:4:cursize(1)
    for j=1:cursize(2)
        average_mag_1m(i-3:i,j)=nanmean(current_mag_col(i-3:i,j));
        average_dir_1m(i-3:i,j)=nanmean(current_dir_col(i-3:i,j));
    end
end

figure, imagesc(distance,depth1,average_mag_1m)
colorbar, caxis([0 1.6]);
title('Magnitude of Velocity (m/s) averaged for 1m
depth','FontWeight','Bold')
xlabel('Length of cross section (m)','FontWeight','Bold')
ylabel('Relative depth (m)','FontWeight','Bold')

figure, imagesc(distance,depth1,average_dir_1m)
colorbar, caxis([0 220])
title('Direction of Velocity averaged for 1m depth','FontWeight','Bold')
xlabel('Length of cross section (m)','FontWeight','Bold')
ylabel('Relative depth (m)','FontWeight','Bold')

%% New arrays in order to put out the NaN data, AVERAGE_MAGNITUDE_1m depth

 counter_line=1; counter_column=1;
    for i=1:4:100
        new_avg_mag_1m(counter_line,1:572)=average_mag_1m(i,1:572);
        counter_line=counter_line+1;
        counter_column=counter_column+1;
    end

 depth_new_1m=min_bath:1:max_bath;
 depth_new_1m=depth_new_1m';

% %% Delete Nan for the fit and plot data
%
% size_mag = size(new_avg_mag_1m);
%
```

```
% for i=1:size_mag(2)
%
%     data1=new_avg_mag_1m(:,i);
%     val1= ~isnan(data1);
%     keep_avg_mag=data1(val1);
%
%     tempdepth=depth_new_1m;
%     keep_depth=tempdepth(val1);
%
%
%
%     figure, plot(keep_avg_mag,keep_depth,'o')
%     hold on
%     set(gca,'YDir','reverse')
%     ylim([0 30])
%     xlim([0.2 2])
%     title(['Velocity averaged every 1m depth, ',
num2str(distance(i)),'m', ' of the cross section'])
%     xlabel('Vertical profile of the Velocity (m/s)','FontWeight','Bold')
%     ylabel('Relative depth (m)','FontWeight','Bold')

%   filename = [num2str(i) '_velocity_1mdepth'];
%   h = gcf;
%   print ('-f8','-djpeg', filename );
%   close (h)
%
% f = fittype('-a*x^n + b','problem','n');
% [c2,gof2] = fit( keep_avg_mag,keep_depth,f,'problem',2);
% plot(c2,'m')


%end

%% Plotting of the 10 seconds  velocity average vs the depth

%%depth1 = 2.49:0.25:27.24;
%%depth1=depth1';



%% for i = 1:4:570
   %% figure, plot(average_mag_10sec(:,i),depth1)
    %% xlim([0.2 2])
    %% ylim([0 30])
    %% title('Verical profile of the Velocity averaged for every
10sec','FontWeight','Bold')
    %% set(gca,'YDir','reverse')
    %% xlabel('Vertical profile of the Velocity (m/s)','FontWeight','Bold')
    %% ylabel('Relative depth (m)','FontWeight','Bold')
%% end

%% Plotting of the 10 seconds  direction average vs the depth
%%for i = 1:4:572
  %%figure, plot(average_dir_10sec(:,i),depth1)
   %%xlim([30 180])
  %% ylim([0 30])
   %%title([' Direction of the Velocity averaged every 10sec, ',
num2str(distance(i)),'m', ' of the cross section'])
  %% set(gca,'YDir','reverse')
  %% xlabel('Verical profile of the Direction (degrees) of the Velocity
','FontWeight','Bold')
  %% ylabel('Relative depth (m)','FontWeight','Bold')
```

```
  %% filename = [num2str(i) '_direction_average_10sec'];
  %% h = gcf;
  %% print ('-f8','-djpeg', filename );
  %% close (h)

%%end

%% Plotting of the velosity averaged every 1mdepth vs the depth

%%for i = 1:1:8
   %%figure, plot(average_mag_1m(:,i),depth1)

   %%xlim([0.2 2])
   %%ylim([0 30])
   %%set(gca,'YDir','reverse')
   %%title('Vertical profile of Velocity averaged for every 1m
Depth','FontWeight','Bold')
   %%xlabel('Verical profile of Velocity (m/s)','FontWeight','Bold')
   %%ylabel('Relative depth (m)','FontWeight','Bold')

%%val1=average_mag_1m(:,1);
%%data1=average_mag_1m(:,1);
%%val1= ~isnan(data1);
%%keep1=data1(val1);
%%tempdepth=depth1(:,1);
%%val2= ~isnan(data1);
%%keep2= tempdepth(val2);

%%end

%% Plotting of the 1m  direction average vs the depth

%%for i = 1:1:572
   %%figure, plot(average_dir_1m(:,i),depth1)

   %% xlim([30 180])
   %% ylim([0 30])
   %% set(gca,'YDir','reverse')

    %%title(['Direction of the Velocity averaged every 1m depth, ',
num2str(distance(i)),'m', ' of the cross section'])

    %%xlabel('Verical profile of the Direction (degrees) of the Velocity

','FontWeight','Bold')
    %%ylabel('Relative depth (m)','FontWeight','Bold')

  %% filename = [num2str(i) '_direction_average_1mdepth'];
  %% h = gcf;
  %% print ('-f8','-djpeg', filename );
   %%close (h)
```